Ulrich M. Engelmann

Assessing Magnetic Fluid Hyperthermia

Magnetic Relaxation Simulation, Modeling of Nanoparticle Uptake inside Pancreatic Tumor Cells and in vitro Efficacy

Author

Ulrich M. Engelmann
Institute of Applied Medical Engineering
RWTH Aachen University, Germany
E-mail: engelmann@ame.rwth-aachen.de

Abstract

As a leading cause of death worldwide with patient-specific evolving mutations, cancer requires innovative therapies capable of individualized treatment. The use of magnetic nanoparticles (MNP) as thermal agents offers such individualized cancer therapy: After local accumulation at the tumor site, MNP can be triggered to transform the energy of an externally applied alternating magnetic field into heat via relaxation of their magnetic moments. This process named magnetic fluid hyperthermia (MFH) enables organ-confined cancer treatment by delivering therapeutic temperatures higher than $43\,°C$ inside tumors, inducing tumor cell death. In this way, MFH efficacy relies on MNP efficiency to generate such elevated temperatures in interaction with the biological environment. However, this environment imposes severe limitations to the MNP magnetic relaxation and heating behavior by restricting the MNP mobility and causing MNP agglomeration. Based on in vitro experiments, this thesis addresses the applicability of MFH to pancreatic tumor cells and discusses opportunities to optimize intracellular MNP heating for clinical application of MFH. The interaction of iron oxide MNP with pancreatic tumor cells and the MNP uptake kinetics inside these cells are investigated using transmission electron microscopy and magnetic particle spectroscopy. The impact of MNP-cell interaction on heating efficiency is quantified with inductive heating experiments and compared to artificially agglomerated and immobilized MNP, mimicking the conditions in cellular environments. Furthermore, Monte-Carlo (MC-)simulations of MNP magnetic relaxation are used to predict sets of parameters varying field amplitude and frequency as well as MNP size and magnetic properties to optimize MFH efficiency under medically tolerable field parameters.

Combined agglomeration and immobilization of MNP upon internalization inside cells decrease heating efficiency by nearly two thirds compared to freely dispersed MNP. This decrease is attributed to one half (one third of the overall heating) to the inhibition of physical rotation upon MNP immobilization, blocking the Brownian contributions of larger MNP to overall heating. The other half can be related to demagnetization effects due to increased magnetic interparticle interactions upon MNP agglomeration. Despite this decrease in MNP heating, MFH can still effectively damage cell in vitro even without a perceptible bulk temperature rise, by local heating on the cellular level. This requires a sufficiently large MNP uptake inside cells, which is reached after approx. $6\,h$ of incubation as predicted from MNP uptake modeling. The cell damage depends on the thermal energy deposited per cell (TEC). Interestingly, healthy cells are more resistant to MFH treatment with a $50\,\%$ margin in TEC to damage healthy cells compared to pancreatic tumor cells. As a consequence, MFH therapy can be tuned to deal tumor-specific damage while healthy surrounding cells remain unharmed by controlling TEC via the intracellular uptake of MNP, the MNP heating efficiency and the duration of MFH treatment. The improvement of intracellular MNP uptake and heating efficiency, e.g. by using MNP with large particle cores ($d_C \geq 25\,nm$) as predicted by MC-simulations, will therefore remain one focus of future work. It seems most important, however, to translate MFH to in vivo experiments in the near future to establish MFH among the standard clinical cancer therapies.

Zusammenfassung

Übersetzung des englischen Originaltitels: *Evaluierung magnetischer Fluid-Hyperthermie: Simulation magnetischer Relaxation, Modellierung der Aufnahme von Nanopartikeln in Pankreas-Tumorzellen und Wirksamkeit in vitro.*

Als eine der weltweit führenden Todesursachen mit patientenspezifischen, sich entwickelnden Mutationen benötigt Krebs innovative Behandlungsmethoden, die eine individuelle Behandlung erlauben. Die Verwendung von magnetischen Nanopartikeln (MNP) als thermische Wirkstoffe bietet eine solche individualisierte Krebstherapie: Nach der lokalen Ansammlung von MNP an der Tumorort, können die MNP durch ein extern angelegtes, magnetisches Wechselfeldes zu Relaxationsprozesse angeregt werden und dadurch die Feldenergie in Wärme umwandeln. Dieser Prozess, genannt magnetische Fluid-Hyperthermie (MFH), erlaubt die lokal auf einzelne Organe beschränkte Krebsbehandlung: Hierbei werden therapeutisch wirksame Temperaturen von über 43 °C in den Tumor eingebracht und schädigen dadurch Tumorzellen irreparabel. In dieser Weise beruht die Wirksamkeit von MFH auf der Effizienz von MNP, diese erhöhten Temperaturen zu erzeugen, wobei die MNP dabei in Wechselwirkung mit der sie umgebenden biologischen Umgebung stehen. Diese Umgebung schränkt dabei das magnetische Relaxations- und Aufheizverhalten der MNP erheblich ein, indem sie die Beweglichkeit der MNP reduziert und MNP Agglomeration verursacht. Diese Arbeit befasst sich auf Basis von in vitro Experimenten mit der Evaluierung der Anwendbarkeit von MFH auf Pankreastumorzellen und diskutiert Ansätze zur Verbesserung der intrazellulären Aufheizung von MNP für die klinische Anwendung von MFH. Die Wechselwirkung von Eisenoxid-MNP mit Pankreas-Tumorzellen und die MNP-Aufnahmekinetik innerhalb dieser Zellen werden mittels Transmissionselektronenmikroskopie und Magnet-Partikel-Spektroskopie untersucht. Der Einfluss der MNP-Zell-Interaktion auf die MNP Aufheizung wird mit induktiven Aufheizexperimenten quantifiziert und mit synthetisch immobilisierten und agglomerierten MNP Modellsystemen verglichen, welche die Bedingungen der biologischen Umgebung nachahmen. Darüber hinaus werden Monte-Carlo (MC-)Simulationen der magnetischen Relaxation von MNP verwendet, um Parametersätze mit variierender Feldamplitude und -frequenz, sowie Partikeldurchmesser und magnetischen Eigenschaften zu bestimmen, die den Wirkungsgrad von MFH optimieren und zwar unter der zusätzlichen Einschränkung von medizinisch tolerierbaren Feldparametern.

Die kombinierte Agglomeration und Immobilisierung von MNP durch die Internalisierung in Zellen verringert die MNP Aufheizung um fast zwei Drittel im Vergleich zu frei dispergierten MNP. Dieser Rückgang der MNP Aufheizung wird zur Hälfte (einem Drittel der Gesamtaufheizung) auf die Hemmung der physikalischen Rotation der MNP bei ihrer Immobilisierung zurückgeführt, die die Brown'schen Beiträge großer MNP zur Gesamtaufheizung blockiert. Die andere Hälfte kann mit Entmagnetisierungseffekten in Verbindung gebracht werden, die durch erhöhte magnetische Wechselwirkung zwischen den MNP aufgrund der Agglomeration in Zellen entstehen. Trotz dieser Reduktion der Gesamtaufheizung der MNP kann MFH Zellen in vitro effektiv schädigen und das sogar ohne einen messbaren Anstieg in der globalen Temperatur der

Probe. Der Grund hierfür liegt auf einer lokalen Aufheizung auf der Zellebene, welche jedoch eine ausreichende Aufnahme von MNP in die Zellen voraussetzt. Aus der Modellierung der MNP-Aufnahme-Kinetik für Pankreastumorzellen folgt eine solche ausreichende MNP-Aufnahme nach 6 h Inkubationszeit. Die Zellschädigung hängt maßgeblich von der eingebrachten Wärmeenergie pro Zelle (EWZ) während der Anwendung von MFH ab. Interessanterweise zeigen sich gesunde Zellen resistenter gegen eine MFH-Behandlung in vitro und eine Marge von 50 % in der EWZ besteht zwischen gesunden Zellen und Tumorzellen. Dadurch kann die Tumorbehandlung durch MFH mittels des EWZ-Parameters auf eine tumorspezifische Schädigung abgestimmt werden, wobei gesunde Zellen in der Umgebung unversehrt bleiben. Die EWZ kann dabei entweder durch die Menge an intrazellulären MNP, die MNP Aufheizleistung oder die MFH-Behandlungsdauer gesteuert werden. Die Verbesserung der intrazellulären MNP Aufnahme- und Aufheizeffizienz, z B. durch den mittels MC-Simulationen vorhergesagten Einsatz von größeren Partikelkernen ($d_C \geq 25$ nm), bildet daher einen Schwerpunkt für zukünftige Arbeiten. Für die Etablierung von MFH als klinisch anerkannte Krebstherapie muss allerdings vorrangig die Untersuchung von MFH in in-vivo Experimenten vorangetrieben werden.

Contents

1. Introduction

With about 14 million new cases reported in 2014 [1] and accounting for 9 million deaths in 2016 [2], cancerous deseases are one of the leading causes of death worldwide [3]. Developed and developing countries are affected alike; e. g. 25.2 % of deaths were caused by cancer in Germany in 2015 [4]. Since cancer is a complex and constantly mutating disease [5], modern medicine is invariably challenged to develop new treatment approaches. Besides improving conventional therapy approaches such as chemotherapy, radiation and resection, much promise lies in novel approaches, adjustable to the cancer-specific challenges of each patient individually. Among these individualized therapies, locally confined *magnetic fluid hyperthermia* (MFH), i. e. the overheating of cancerous tissue, has gained much attention in current research due to its potential for the individualization of therapy, as will be outlined in the following.

The MFH principle relies on the use of *magnetic nanoparticles* (MNP) to generate therapeutic heat. MNP are nanosized magnets with sizes[1] below 100 nm [6] and introduce the phenomenon of *superparamagnetism* [7]. As such, MNP display unique heating characteristics when subjected to an alternating magnetic field (AMF), potentially allowing a precise temperature control required for individual therapy [8]. MNP can also be magnetically guided to and accumulated at the tumor site after injection in the body's circulatory system. This provides a high degree of individualization, as virtually any tumor site accessible by a magnetic field can be targeted with MNP and treated with therapeutic heat.

First successful clinical trials of MFH therapy performed between 2004 and 2011 confirmed the feasibility of clincial MFH [9]; however, after 2011, these trials were discontinued and broad clinical application of MFH is still missing. This is due to the fact that the concentration of MNP necessary to induce therapeutic temperatures (T$\leq$ 43 °C [10]) used in these trials has been very high and the biocompatibility of the MNP at such high concentration is ultimately not proven yet. Furthermore, MNP unavoidably interact with biological and cellular components inside the body. E. g., MNP internalization inside cells confines the MNP arrangement and immobilizes the MNP [11], and the effects of intracellular internalization of MNP on particle heating are poorly understood at present [12]. From this, two demands can be identified to advance the clinical application of MFH: (I) MNP heating performance must be improved in order to reach therapeutic temperatures at lower MNP concentrations that are biocompatible and (II) the interaction of MNP with tumor cells and its effects on particle heating must be deciphered. These demands translate into four research questions that this thesis endeavors to answer:

1. *What MNP (i. e. which MNP properties) maximize the particle heating in MFH?*

2. *How do MNP interact with cells and how can the MNP uptake inside cell be quantified?*

---

[1] By definition, the particle *size* denotes the particle *diameter* throughout this thesis.

3. *How does particle heating change upon MNP internalization inside cells?*

4. *How efficient is intracellular MFH applied to (tumor) cells; esp. at low MNP concentrations?*

This thesis sequentially investigates these four questions on the basis of well characterized MNP systems using an experimental approach: First, the particle heating in terms of the MNP properties and AMF parameters are evaluated experimentally and the results are compared to theoretical particle heating simulations using MNP relaxation theory. In this way, optimal MNP properties and AMF parameters for maximum particle heating are identified (Chapter 5). Second, the MNP-cell interactions in vitro with pancreatic tumor cells and healthy control cells are investigated, assessing the changes in arrangement that MNP undergo upon intracellular internalization and deriving a model for predicting the uptake kinetics of MNP (Chapter 6). Third, based on the MNP-cell interaction analysis, the effects of MNP internalization on particle heating are examined using artificial in situ model systems, which mimic the states of intracellular MNP (Chapter 7). Finally, the efficacy of MFH on pancreatic tumor cells is assessed in vitro using low MNP concentrations and the main parameters contributing to MFH effectiveness are identified (Chapter 8).

Short Description of each Chapter

This thesis is divided in seven main chapters. Chapter 2 provides background knowledge on key topics covered in this thesis: First, a basic introduction to the physical principles of magnetism with special focus on superparamagnetism is given, followed by an overview of the physical concepts governing the particle relaxation and heating processes. Moreover, the state-of-the-art in applying MFH in tumor therapy is summarized, also explaining how the application of MFH can be implemented in a treatment approach for pancreatic tumor therapy. Lastly, the chapter concludes with a description of the mechanical properties of hydrogels that are later used as tissue-mimicking modeling systems to incorporate MNP (cf. Chapter 7).

Chapter 3 presents the simulations of magnetic particle relaxation used to predict optimized particle heating. It first outlines the current state of research on simulating magnetic particle heating and, second, explains the implementation of the Monte-Carlo-based (MC-)simulation employed for predicting particle heating in this thesis. The simulation results are verified and compared to common theories of particle heating. From this, general trends for particle heating in dependence of MNP properties and AMF parameters are derived, which are later used to derive the optimal MNP properties and AMF parameters for maximum particle heating (cf. Chapter 5).

Chapter 4 describes the synthesis of MNP and covers the characterization of MNP properties. Each characterization technique used is introduced briefly by explaining the experimental procedure, followed by the analysis and discussion of the characterization results and the specific

MNP properties. These MNP properties are key parameters for the investigations of particle heating, MNP-cell interactions and intracellular particle heating effects in all following chapters.

Particle relaxation and heating measurements are presented in Chapter 5. This chapter introduces magnetic particle spectroscopy (MPS) as a means of characterizing MNP relaxation processes. Following, the particle heating of each MNP system is analyzed and discussed on the basis of the predictions of particle heating in dependence of MNP properties and AMF parameters derived from MC-simulations in the previous Chapter 3. Most importantly, MC-simulation results for particle heating are validated against experimental data. These validated MC-predictions are then employed to predict the optimal MNP properties and AMF parameters for maximum particle heating, answering research question 1 from above.

Chapter 6 investigates MNP-cell interactions with special consideration of changes in MNP morphology upon internalization inside cells and the quantitative description of the MNP uptake kinetics. A mathematical model is developed and fitted to the uptake kinetics, allowing to predict the amount of intracellular MNP for arbitrary incubation times. Key factors of how MNP arrangement, mobility and magnetic properties are affected upon MNP uptake inside cells are identified and quantified: Most importantly, MNP are found to be immobilized and agglomerated intracellularly. Overall, this chapter is dedicated to answer research question 2 from above.

On the basis of MNP immobilization and agglomeration effects inside cells from the previous Chapter 6, MNP model systems are presented in Chapter 7, which allow the study of the effects of either immobilization or agglomeration on particle heating in isolation. Therefore, MNP are suspended in two hydrogels of tunable mesh size, allowing the gradual control of the degree of immobilization of the incorporated MNP. Moreover, two systems of controlled MNP agglomeration are prepared, one of which even allows the evaluation of the combined effect of immobilization and agglomeration simultaneously. This chapter answers research question 3 from above.

In the last main Chapter 8, the efficacy of MFH applied to pancreatic tumor cells after incubation with low MNP concentrations is studied and the cytotoxic effects of MFH treatment are assessed. The superior efficacy of MFH compared to standard hyperthermia is demonstrated and reveals the presence of so-called nanoheating effects on the cellular level during MFH application. Furthermore, three main factors for controlling and improving MFH efficacy are identified: The overall particle heating performance, the amount of MNP internalized inside cells and the duration of treatment. These three factors can be combined in the single parameter of the thermal energy deposited per cell (TEC), allowing to assess the efficacy of MFH for specific tumors individually. In this way, Chapter 8 provides an answer to research question 4.

2. Background

This chapter introduces to the basics of nanomagnetism, magnetic particle relaxation, imaging and heating, as well as the current status of applying particle heating in tumor therpay and the use of hydrogels as tissue-equivalent model systems in biomedical applications. In detail, the basics of the theory of magnetism precedes the current chapter in Section 2.1. This section forms the foundation for a subsequent summary on the physics of magnetic particle relaxation in Section 2.2, followed by a brief introduction in the principles of magnetic particle imaging in Section 2.3. Subsequently, the physics of magnetic particle heating are explained in Section 2.4, including the leading mathematical theories developed for describing particle heating. An overview on the present-day applications of magnetic fluid hyperthermia is given in Section 2.5, where also a treatment strategy for the example of pancratic tumors is discussed. Finally, Section 2.6 concludes the present chapter by reviewing the application and mechanical description of hydrogels as tissue-equivalent model systems.

2.1. Theory of Magnetism

Generally, the phenomena of magnetism are easy to measure experimentally, but very complex to explain theoretically. Only when applying quantum mechanics down to the atomic scale, can a satisfactory explanation be given. The following sections are compiled to explain the basic magnetic phenomena (Section 2.1.1) neccessary to understand the concepts of magnetic anisotropy (Section 2.1.2) and superparamagnetism (Section 2.1.3). To this end, this section focuses on illustrating and understanding these phenomena rather than on complex calculation and is based on the concepts from [13] and [14], if not mentioned otherwise.

2.1.1. Basics of Magnetism

Materials exposed to a magnetic field, $\boldsymbol{H}$, acquire a magnetization, $\boldsymbol{M}$. This magnetization originates from the alignment of the magnetic (dipole) moments, $\boldsymbol{m} = g\mu_{\mathrm{B}}\boldsymbol{J}$, of each individual atom within the material and is defined per unit volume, V, as $\boldsymbol{M} = \frac{1}{V}\sum_{n=1}^{N}\boldsymbol{m}_n$. Here, $g = 2.0023$ is the Landé-factor for electrons, $\mu_{\mathrm{B}} = 9.274 \cdot 10^{-24}\,\mathrm{A} \cdot \mathrm{m}^2$ is the Bohr magneton and $\boldsymbol{J} = \boldsymbol{L} + \boldsymbol{S}$ is the atom's total angular momentum, combining the orbital momentum $\boldsymbol{L}$ and the intrinsic atomic momentum $\boldsymbol{S}$, denoted as spin. For most materials the magnetization aligns with an applied magnetic field, $\boldsymbol{H}$, linearly according to

$$\boldsymbol{M} = \chi \cdot \boldsymbol{H}. \tag{2.1}$$

χ is the magnetic susceptibility, which is generally a three-dimensional tensor. For homogeneous and isotropic materials all non-diagonal entries vanish and χ reduces to a scalar.
The response of any material to the applied magnetic field, $\boldsymbol{H}$, is called magnetic induction,

$\boldsymbol{B}$, and is defined by

$$\boldsymbol{B} = \mu_0(\boldsymbol{H} + \boldsymbol{M}), \tag{2.2}$$

with the magnetic constant $\mu_0 = 4\pi \cdot 10^{-7}\,\mathrm{N\,A^{-2}}$. If a magnetic material is inserted into the magnetic field $\boldsymbol{H}$ in free space, a demagnetizing field, $\boldsymbol{H_d}$, develops inside the material. $\boldsymbol{H_d}$ opposes the intrinsic magnetization of the material, $\boldsymbol{M}$, and can be approximated for magnetic materials of ellipsoidal shape as

$$\boldsymbol{H_d} = -N_{\mathrm{d}} \cdot \boldsymbol{M} \tag{2.3}$$

with the demagnetizing factor N_{d}, which is a function of the geometry of the material (e. g. $H_{\mathrm{d}} = 1/3$ for a spherical magnet). Therefore, the field inside a magnetic material actually reads $\boldsymbol{H}_{\mathrm{in}} = \boldsymbol{H} + \boldsymbol{H_d}$.

By introducing the susceptibility from eq. (2.1) in eq. (2.2) one obtains $\boldsymbol{B} = \mu \boldsymbol{H}$, with the permeability

$$\mu = \mu_0(1 + \chi) = \mu_0\mu_{\mathrm{r}}. \tag{2.4}$$

The relative permeability μ_{r} is used to classify all materials according to their magnetic behavior. Note that this classification is not without exceptions but provides a simple basis, upon which five different types of magnetism can be distinguished, divided according to the arrangement and interaction of the materials' atomic magnetic moments and the temperature dependence of the materials' magnetization:

Diamagnetism (DM)

For diamagnets $\mu_{\mathrm{r}} < 1$ holds as their susceptibility is $-1 < \chi_{\mathrm{DM}} < 0$. With no external magnetic field applied, the net magnetic moment of each individual atom of the diamagnet is zero. Typical examples are materials with completely filled electronic shells (e. g. noble gases such as argon or neon) or semiconductors with strong covalent bonding (e. g. silicon, diamond). Only when a magnetic field is applied a magnetic moment arises from the precession of the electron orbits around the direction of the field. The magnetic moment is proportional to the field strength according to eq. (2.1), but in the opposite direction of the field, with $\chi_{\mathrm{DM}} < 0$. On a side note: Diamagnets with $\chi_{\mathrm{DM}} = -1$ form the special class of ideal superconductors. In the superconducting state, usually accessible only at very low temperatures close to $T = 0\,\mathrm{K}$, these materials expel the magnetic induction $\boldsymbol{B}$ from their interior and pass electric currents with zero resistance. Note that diamagnetism is present in all known materials but is weak compared to the other types of magnetism (s. below). Hence it is usually not detectable experimentally in para- or ferromagnets as it is dominated by the response of the atomic magnetic moments to the applied field.

Paramagnetism (PM)

Paramagnets follow eq. (2.1) with $\mu_r > 1$ and thus $0 < \chi_{PM} < 1$. PM is observed in metals like aluminum, gold and copper [15]. On a microscopic scale, paramagnets differentiate from diamagnets as the magnetic moment of each atom is not equal to zero in the absence of an external magnetic field. When the magnetization in zero field is measured however, DM and PM are indistinguishable and both show $|M| = 0$. Even though paramagnets have magnetic moments for each atom, they add up to zero net magnetization in the ensemble average at room temperature, since the thermal energy is sufficiently high for the magnetic moments to orientate randomly due to thermal fluctuation. Applying a weak magnetic field aligns some of the magnetic moments, resulting in a small net magnetization. As the field is increased, more and more magnetic moments align along the direction of the field, usually following a linear increase in M (corresponding to a constant susceptibility χ, eq. (2.1)). If the temperature is increased at constant field instead, the additional thermal fluctuation causes a decrease in M and in χ. Generally, the susceptibility χ is inversely proportional to the temperature T, described by Curie's law of paramagnetism, reading:

$$\chi_{PM} = C/T, \tag{2.5}$$

with $C = \frac{\mu_0 N |m|^2}{3k_B}$, where N denotes the number of magnetic moments in the entire paramagnetic ensemble, each with the magnetic dipole moment magnitude $|m|$. Note that eq. (2.5) is only valid for $T < T_C$, where T_C is the Curie temperature, an experimentally determined parameter characteristic for a specific paramagnetic material.

Paramagnets can be described in theory by assuming equal magnetic moments for each atom that only interact with the field H, but not with each other, and have a total angular momentum quantum number J. The magnetization of such an idealized paramagnet with N atoms is mathematically described by

$$M = N \cdot g\mu_B J \cdot B_J(x) = N \cdot m \cdot B_J(x). \tag{2.6}$$

With the Brillouin function

$$B_J(x) = \frac{2J+1}{2J} \cdot \coth\left(\frac{2J+1}{2J} \cdot x\right) - \frac{1}{2J} \cdot \coth\left(\frac{x}{2J}\right) \tag{2.7}$$

and $x = \dfrac{m \cdot H}{k_B T}$.

$B_J(x)$ is a function of temperature, T, and the Boltzmann constant, $k_B = 1.3806 \cdot 10^{-23}$ J/K. For small fields $H \ll 1$, and thus $x \ll 1$, eq. (2.7) can be expanded in a Taylor series reading to first order approximation $B_J(x) \approx \frac{J+1}{3J} \cdot x + O(x^3)$. Inserting this Taylor series in eq. (2.6) yields the linear relationship generally observed for paramagnets $M \propto H$ (cf. eq. (2.1)).

Ferromagnetism (FM)

A few materials (primarily iron, nickel, cobalt and their alloys [15]) display a permanent mag-

netization even in the absence of an applied external field. They are called ferromagnets. With $\mu_r \gg 1$, ferromagnets show the highest magnetization of all magnetic materials, when exposed to an external field $\boldsymbol{H}$. FM is caused by the individual atoms' spins that interact with each other via a strong but short-ranged interaction, aligning neighboring spins in parallel arrangement. This so-called exchange interaction causes a permanent spin order within ferromagnets and leads to a permanent magnetization.

Ferromagnetic Hysteresis Ferromagnetic materials do not fulfill eq. (2.1) and exhibit a previous-magnetization-dependent response when exposed to $\boldsymbol{H}$, called *hysteresis*. A typical hysteresis curve (loop) is depicted in Fig. 2.1, where the magnetization M is plotted versus the applied external field $\boldsymbol{H}$. The enveloping loop can be recorded by applying a sufficiently strong
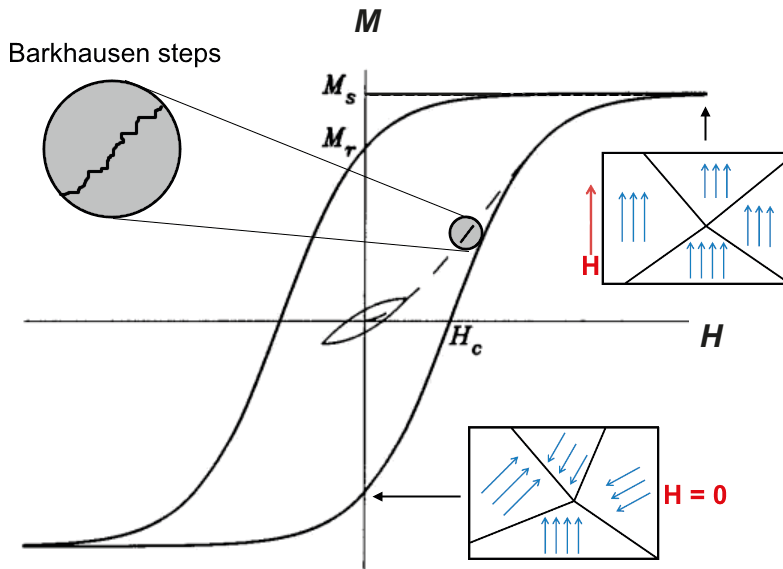
Fig. 2.1.: Schematic diagram of a hysteresis curve $M(H)$. The enveloping loop marks the major hysteresis loop, reaching saturation magnetization, M_S, for large fields $|\boldsymbol{H}| > H_C$. $M = 0$ when the coercivity field, $|\boldsymbol{H}| = H_C$, is applied, whereas for $\boldsymbol{H} = 0$ a permanent magnetization called remanence, M_r, remains. The inner curve shows a minor loop for small $\boldsymbol{H}$. The dashed line markes the virgin curve. The mircoscopic regions of uniform spontaneously aligned magnetization, called domains, are marked at two destinct points (at positive saturation for large $\boldsymbol{H}$ and at $\boldsymbol{H} = 0$). Barkhausen steps arise from irreversible domain wall motions on the microscale (shown in zoom). Adapted from [13].

field to align all magnetic moments with the field and reach the saturation magnetization M_S. When $\boldsymbol{H}$ is reduced to zero a permanent magnetization $|\boldsymbol{M}(\boldsymbol{H} = 0)| = M_r$, the so-called remanence, remains within the ferromagnet. Now applying $\boldsymbol{H}$ in the opposite direction, a certain field strength is required to reset $M = 0$. This field is named coercivity H_C. Both segments of the hysteresis curve, going from $|\boldsymbol{H}| = 0$ to $|\boldsymbol{H}| = \pm H_C$ are denoted as demagnetizing curves. By applying an equally strong and saturating field in the opposite direction, the lower tail of the loop can be traced. The entire outer loop is named major (hysteresis) loop. The loops are actually a whole continuum of curves enveloped by the major loop. The smaller curves do

not reach M_S for applied fields below coercivity, $|\boldsymbol{H}| < H_C$ and are thus denoted as minor hysteresis loops. By adapting $|\boldsymbol{H}|$ appropriately, every remanent magnetization value between $-M_r r < |\boldsymbol{M}| < +M_r$ can be selected. Ferromagnets can lose their permanent (remnant) magnetization, meaning to set $\boldsymbol{M} = 0$ for $\boldsymbol{H} = 0$, either by cycling the applied field with steadily decreasing amplitude or heating the ferromagnet above the critical Curie-temperature $T > T_C$ (e.g. $T_C \approx 1\,041\,\mathrm{K}$ for Fe). Above T_C the spin order characteristic for FM is broken by thermal fluctuation and the ferromagnet behaves like a paramagnet with $\mu_r > 1$. A third way of demagnetizing a ferromagnet is to mechanically break the spin order, e.g. by forcefully throwing it to the ground. However, this methods holds a high risk of damaging the ferromagnet permanently.

Magnetic Domain Formation A qualitative description of the magnetic properties of ferromagnets was first introduced by Pierre-Ernst Weiss in 1907. Weiss stated that atomic magnetic moments (later named spins, as is also the denotation throughout this thesis) align against thermal fluctuation in areas within the ferromagnet and he termed those areas of aligned spins *(magnetic) domains* [16]. Within a single domain, some exchange interaction (defdinded below, cf. eq. (2.8)) between spins aligns them parallel to each other. Between domains, however, the direction of the magnetization vector varies, if no external field is applied. Thus, when the bulk magnetization over many domains is measured in the absence of a field, the superposition of the randomly oriented domain magnetization vectors yields $|\boldsymbol{M}| < M_S$, as not all vectors are aligned. An external field $\boldsymbol{H}$ forces the domain walls to shift position. As some of these positions lead to preferred local minima in the total energy of the crystal, the random shift of the walls causes a discontinuous change in magnetization on the microscale, known as Barkhausen steps [17]. Consequently, the magnetization in a gradually increasing field occurs in discontinuous steps on the microscale as sketched in Fig. 2.1. A sufficiently large field ($|\boldsymbol{H}| \geq H_C$) aligns all domains and the full saturation magnetization M_S is reached. When the field is reduced after saturation, the domains remain in their newly preferred orientation and the overall addition of domain magnetization vectors yields $|\boldsymbol{M}| = M_r$ for $\boldsymbol{H} = 0$.

The formation of domains originates from the interaction between exchange and anisotropy energies within a ferromagnetic crystal, which are explained briefly in the following: The (Heisenberg) exchange interaction is the short-ranged (between next neighbors) but strong quantum mechanical mechanism between atomic spins that aligns these spins parallel to each other. Its energy, ε_{ex}, can be summed over all atoms in the crystal pair by pair, i, j, reading

$$\varepsilon_{ex} = -2 \cdot \sum_{i \neq j} J_{ij} \boldsymbol{S}_i \cdot \boldsymbol{S}_j, \qquad (2.8)$$

with the factors J_{ij}, the so called exchange integrals, describing the strength and range of the interaction. J_{ij} is accessible by experiment from the Curie temperature, T_C, where the magnets saturation magnetization becomes zero and therefore T_C is a natural measure for the strength of the atomic exchange interaction.

Anisotropy within ferromagnets arises from the spin-orbit interaction, which mainly couples the electronic orbits to the crystallographic structure. Further contributions to anisotropy arise

from geometrical deviance from spherical symmetry and spin-canting effects at the surface of nanosized ferromagnets. These different contributions to anisotropy are discussed in detail in the next Section 2.1.2. For now, simply consider the total effective anisotropic energy ε_{ai} resulting from these contributions (cf. eq. (2.21) for a mathematical definition). The anisotropy energy is generally much lower than the exchange energy $\varepsilon_{ex} \gg \varepsilon_{ai}$. But since the exchange interaction is always isotropic in space, the direction of magnetization M in a domain is exclusively determined by anisotropy energy ε_{ai}. The preferred directions of magnetization within the crystal, i. e. those directions, where ε_{ai} is minimal, are named easy axes

Both the exchange and anisotropy energies compete with a third energy, named magnetostatic or demagnetizing energy, ε_{ms}, whose energy reads

$$\varepsilon_{ms} = -\frac{\mu_0}{2} \int M \cdot H_d \, dV. \tag{2.9}$$

with the magnetization M and the demagnetizing field H_d, while the integration is over the whole volume of the ferromagnetic body, V and the factor $\frac{1}{2}$ corrects the otherwise twofold counting of the interaction between two atoms. ε_{ms} is a complicated function of the domain geometry and therefore also denoted shape anisotropy (cf. Section 2.1.2). The magnetostatic interaction is long-ranged compared to the exchange interaction, spanning many atoms or several hundreds of nanometers. The energy ε_{ms} is stored in a magnetic stray field (s. Fig. 2.2). The
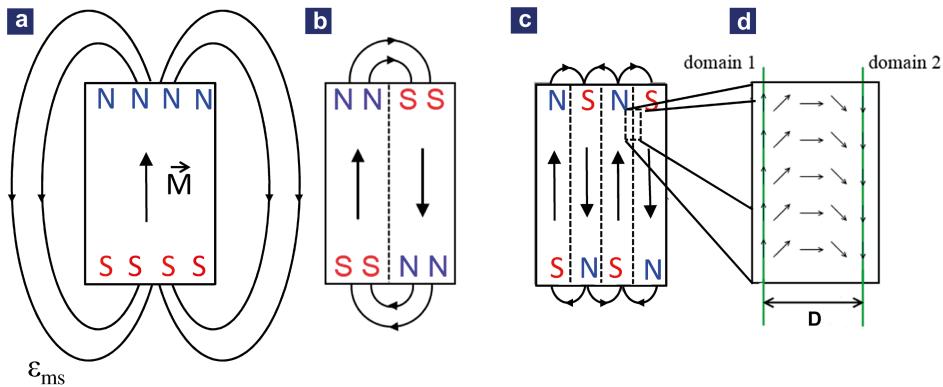
Fig. 2.2.: Magnetic domains and domain wall formation: (a) shows a single domain with the magnetization $\vec{M}$ directed from magnetic south S to magnetic north N. The stray field is large and the magnetostatic energy ε_{ms} is maximal. In comparison, in (b) two domains and even four in (c) reduce the stray field and consequently ε_{ms} remarkably. But this reduction comes at the expense of an increase in exchange energy ε_{ex}, which causes a gradual reversal of the spin direction between domain 1 and domain 2 across the length D, as shown in (d). Adapted from [18].

three energies, ε_{ex}, ε_{ai} and ε_{ms} allow for a deeper understanding of the formation of domains in a ferromagnetic crystal, since the magnetization direction, strength and area of the domains are governed by minimizing the net energy

$$\varepsilon_{net} = \varepsilon_{ex} + \varepsilon_{ai} + \varepsilon_{ms} \tag{2.10}$$

with $\varepsilon_{\mathrm{ex}} \sim \varepsilon_{\mathrm{ms}} \gg \varepsilon_{\mathrm{ai}}$.

The interplay between energy minimization of $\varepsilon_{\mathrm{ex}}$ by aligning spins parallel and $\varepsilon_{\mathrm{ms}}$ by reducing the stray field causes the formation of magnetic domains, as shown in Fig. 2.2. Furthermore, $\varepsilon_{\mathrm{ex}}$ is responsible for the gradual change of the magnetization vector M between domains, called domain walls, cf. Fig. 2.2d. Here, $\varepsilon_{\mathrm{ex}}$ aims to keep the angular separation between neighboring spins minimal, which increases the wall thickness. $\varepsilon_{\mathrm{ex}}$ competes with the anisotropy energy $\varepsilon_{\mathrm{ai}}$, to which the spins favorably align along the easy axes (directions of easiest magnetization, s. sec. 2.1.2 for details) and thus forms comparatively thinner walls. The actual wall thickness, D, is a result of the equilibrium between exchange and anisotropy energy.

Antiferromagnetism (AFM)

In antiferromagnets the neighboring spins show a strong but negative (i. e. repulsive) interation, therefore they align anti-parallel to each other. The spins, all originating from a single magnetic species, are distributed in equal numbers on two interpenetrating, antiparallel crystal lattices. Consequently, they add up to zero net magnetization in the absence of an applied field. Antiferromagnetic materials typically show paramagnetic properties at room temperature but display a complex behavior in susceptibility χ below a critical temperature, named the Néel temperature T_{N}: For $T < T_{\mathrm{N}}$, antiferromagnetic spins align in the characteristic antiparallel spin order and χ depends on whether H is applied perpendicular or parallel to the orientation of the spins. Common AFM examples are cobalt(II)oxide (CoO), nickel(II)oxide (NiO) and wustite (FeO) [15].

Ferrimagnetism (FeM)

In materials with two or more magnetic species, their different magnetic moments and sublattices give rise to a strong and negative interaction between the individual species' spins, leading to an anti-parallel arrangement of these spins. In contrast to AFM, neighboring atoms have different magnitudes of magnetic moments. Therefore, ferrimagnets show a non-zero (permanent) net magnetization in zero magnetic field below a critical temperature. As this magnetization is permanent as in ferromagnets, this critical temperature is also denoted Curie temperature, T_{C}. For $T > T_{\mathrm{C}}$ the spin order of FeM is broken by thermal fluctuations in the same way as described above for FM. Typical ferrimagnetic materials are oxides, including iron-oxides maghemite (γ-Fe_2O_3) and magnetite (Fe_3O_4), which will be used throughout this thesis.

2.1.2. Magnetic Anisotropy

Experiments reveal that the magnetization of a ferromagnet (or a antiferro- or ferrimagnet for that matter) has a preferential orientation along certain internal directions. These preferential directions depend on the crystallographic structure, the magnet geometry, mechanical stress within the magnetic material or — in the case of small magnetic objects — spin-canting at the

surface. These four dependencies are referred to as *magnetocrystalline* (with energy ε_{mc}), *shape* (or magnetostatic) (ε_{ms}), *stress* (or magnetoelastic) (ε_{me}), and *surface anisotropy* (ε_{sur}), respectively. They all contribute to the net anisotropy energy, ε_{ai}, reading

$$\varepsilon_{ai} = \varepsilon_{mc} + \varepsilon_{ms} + \varepsilon_{me} + \varepsilon_{sur}. \tag{2.11}$$

and will be discussed individually briefly in the following. Note that the general description will be discussed in more detail for the special case of spherical magnetic nanoparticles, where appropriate.

Magnetocrystalline Anisotropy

Every magnet exhibits magnetocrystalline anisotropy, which arises from spin-orbit interaction: The symmetrical order of atoms in the crystal lattice generates electrostatic fields that couple with the electronic orbits, which in turn are interacting with the electronic spins. This results in preferential directions of magnetization. Directions, in which saturation magnetization is reached easiest (i. e. at lowest applied fields) are called easy axes and those directions along which magnetizing is most difficult, hard axes. Depending on the crystallographic structure of the magnetic material, generally, two different formulations of magnetocrystalline anisotropy — *uniaxial* and *cubic* anisotropy — are discussed:

Uniaxial Anisotropy In crystals with only one easy axis, e. g. hexagonal crystals such as cobalt, the magnetocrystalline energy is isotropic for any given angle, φ, in the plane perpendicular to the easy axis. The anisotropy of such crystals is therefore *uniaxial* and the magnetocrystalline anisotropy energy is given by:

$$\varepsilon_{mc}^{u} = K_{u}V \cdot \sin^2(\theta). \tag{2.12}$$

Where K_{u} denotes the temperature-dependent uniaxial anisotropy constant, which is usually determined experimentally,[1] V is the sample volume and θ describes the angle between the easy axis and the direction of magnetization. Note that eq. (2.12) is an approximation, only taking into account the dominant contribution to angle-dependent anisotropy (since the direction of magnetization inside a magnet is exclusively determined by the angular dependency of ε_{ai}, as stated in Section 2.1.1).

Assuming spherical magnetic nanoparticles with a particle magnetic moment $\boldsymbol{m}$ (equivalent to the magnet's magnetization, $\boldsymbol{M}$, mentioned above), eq. (2.12) simplifies further to:

$$\varepsilon_{mc}^{u} = K_{u}V \cdot (\boldsymbol{m} \cdot \boldsymbol{n})^2, \tag{2.13}$$

---

[1] Anisotropy constants of thin film materials are for example determined by angle-dependent ferromagnetic resonance (FMR) measurements [19]. However, magnetic nanoparticles, as used throughout this thesis, are very challenging to prepare for FMR measurements.

where θ marks the angle between $\boldsymbol{m}$, and the particle easy axis, $\boldsymbol{n}$, and further assuming that $\boldsymbol{m}, \boldsymbol{n} \in K$, where K is the unit sphere.

Cubic Anisotropy Cubic crystals (such as iron and nickel, but also iron-oxides as used in this thesis) posess more than one easy axis of magnetization. Therefore, their magnetocrystalline energy, ε_{mc}^c, depends on the direction that the magnetization vector $\boldsymbol{M}$ makes with the principal crystallographic axes of the crystal [14]: These directions can be expressed as the directional cosines of $\boldsymbol{M}$, $\alpha_1 = \cos(a)$, $\alpha_2 = \cos(b)$ and $\alpha_3 = \cos(c)$, defined as shown in Fig. 2.3. Using
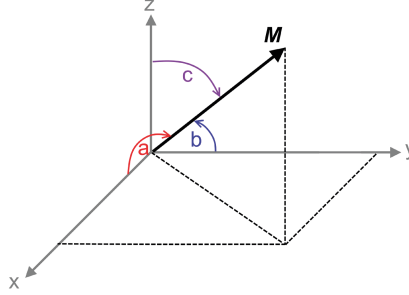
Fig. 2.3.: Sketch of the directional cosines of the magnetization $\boldsymbol{M}$: $\alpha_1 = \cos(\textcolor{red}{a})$, $\alpha_2 = \cos(\textcolor{blue}{b})$ and $\alpha_3 = \cos(\textcolor{purple}{c})$. Adapted from [14].

these directional cosines, ε_{mc}^c reads:

$$\varepsilon_{mc}^c = K_{c_1} V \cdot (\alpha_1^2 \alpha_2^2 + \alpha_2^2 \alpha_3^2 + \alpha_3^2 \alpha_1^2) + K_{c_2} V \cdot \alpha_1^2 \alpha_2^2 \alpha_3^2, \tag{2.14}$$

with the sample volume V and the cubic anisotropy constants K_{c_1} and K_{c_2}. As explained for uniaxial anisotropy already, the angle-independent terms were neglected again. Typical values are $K_{c_1} \approx 48 \, \text{kJ/m}^3$ and $K_{c_2} \approx 5 \, \text{kJ/m}^3$ for iron [14] and $K_{c_1} \approx -11 \, \text{kJ/m}^3$ and $K_{c_2} \approx -3 \, \text{kJ/m}^3$ for magnetite at room temperature [20]. The directions of the easy axes in a cubic crystal depend on the sign of K_{c_1} and K_{c_2}, as depicted in Fig. 2.4. Knowing that $K_{c_1} < 0$ and $K_{c_2} < 0$ holds for magnetite at room temperature [20], one directly sees from Fig. 2.4 that the easy axis aligns along the [111]-direction in magnetite.

The Anisotropy Field The forces binding the magnetization to the easy axes can be expressed in terms of a pseudo-field, denoted *anisotropy field*, $\boldsymbol{H}_K$. This field is parallel to the easy axes and defined by the torque, $\boldsymbol{\tau} = \mu_0 \boldsymbol{M} \times \boldsymbol{H}_K = \frac{d\varepsilon_{mc}}{d\theta}$, on the magnetization $\boldsymbol{M}$ with the angle between easy axes and $\boldsymbol{M}$, θ. For small angles $\sin(\theta) \approx \theta$ and with $|\boldsymbol{M}| = M_S$ the saturation magnetization, a general approximation for the magnitude of the anisotropy field yields

$$|\boldsymbol{H}_K| = H_K = \frac{2K_i}{\mu_0 M_S}, \tag{2.15}$$

with $i = u, c$, for uniaxial or cubic anisotropy.
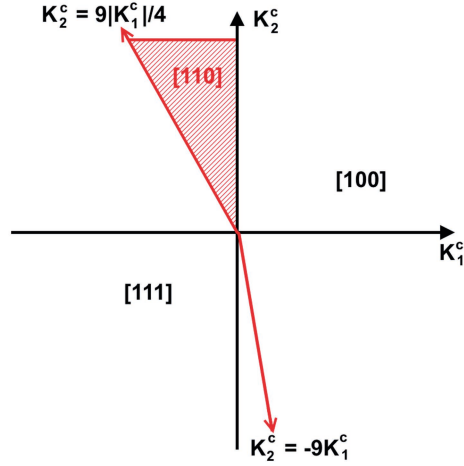
Fig. 2.4.: Directions of magnetization along easy axes for cubic crystals as a function of the anisotropy constants K_{c_1} and K_{c_2}. The direction [110] is shown in red (holds for the shaded region). Adapted from [14].

Shape Anisotropy

Shape anisotropy arises from the divergence in the magnetization at the surface of a magnet, generating a stray or demagnetizing field, as described previously in eq. 2.9. In the following, a solution to the integration for $\varepsilon_{\mathsf{ms}}$ (cf. eq. (2.9)) is presented for the case of a prolate spheroid: Assuming the magnetization in the x-z-plane with $M_{\mathsf{S}}^x = M_{\mathsf{S}} \cdot \sin(\theta)$ and $M_{\mathsf{S}}^y = M_{\mathsf{S}} \cdot \cos(\theta)$, the angle between the direction of magnetization and the easy axis is denoted as θ. If the dimensions of the spheroid are elongated along the z-axis, with $l_x = l_y < l_z$ and the demagnetization factors N_x, N_y and N_z are known, $\varepsilon_{\mathsf{ms}}$ can be expressed by

$$\varepsilon_{\mathsf{ms}} = \frac{1}{2}\mu_0 N_z M_{\mathsf{S}}^2 V + \frac{1}{2}\mu_0 (N_x - N_z) M_{\mathsf{S}}^2 V \cdot \sin^2(\theta) := K_0 V + K_{\mathsf{sh}} V \cdot \sin^2(\theta). \quad (2.16)$$

The easy axis of a prolate spheroid determined by shape anisotropy is therefore governed by the strength of the shape anisotropy constant K_{sh} with respect to the other anisotropy constants, while K_0 can be neglected as it has no angle dependency.

Stress Anisotropy

A magnetic material subjected to a sufficiently strong magnetic field changes its dimensions, which changes of overall volume, V. This places mechanical stress (or strain) on the crystal lattice, which in turn induces preferential directions for the magnetization vector known as stress or magnetoelastic anisotropy. The magnetoelastic energy of a cubic crystal under stress can be described in terms of the elastic stress σ_{s} and the magnetostriction constant λ_{s}:

$$\varepsilon_{\mathsf{me}} = \frac{3}{2} \int \sigma_{\mathsf{s}} \cdot \lambda_{\mathsf{s}} \mathrm{d}V \quad (2.17)$$

integrated over the entire magnetic volume, V. For isotropic crystals and uniform stress, eq. (2.17) simplifies to

$$\varepsilon_{\mathsf{me}} = K_{\mathsf{me}} \sin^2(\vartheta), \tag{2.18}$$

with ϑ the angle between magnetization, $\boldsymbol{M}$, and the applied stress direction and $K_{\mathsf{me}} = \frac{3}{2}\sigma_{\mathsf{s}} \cdot \lambda_{\mathsf{s}}$. Typical values of magnetostriction constants are $\lambda_{\mathsf{s_{Fe,bcc}}} = -7$ for polycrystalline iron and $\lambda_{\mathsf{Fe_3O_4}} = 40$ for polycrystalline magnetite [14].

Surface Anisotropy

Nanostructured magnetic objects (such as magnetic nanoparticles), which are characterized by a significant surface to volume ratio (and therefore a relatively large number or surface atoms), can additionally experience surface anisotropy. Here, the deviations from crystal symmetry at the surface due to structural defects, broken exchange bonds and surface strain can dominate the magnetocrystalline and shape anisotropy effects [21]. The effective anisotropy increases as the size of spherical nanomagnets decreases [22], which is described very well by an effective anisotropy constant, adding bulk (core) anisotropy, K_{B}, and surface anisotropy, K_{S}, contributions:

$$K_{\mathsf{eff}} = K_{\mathsf{B}} + \frac{6}{d} K_{\mathsf{S}}, \tag{2.19}$$

where d is the particle diameter. The surface anisotropy energy arises solely from K_{S} and reads

$$\varepsilon_{\mathsf{sur}} = K_{\mathsf{S}} V \frac{6}{d}. \tag{2.20}$$

Total Anisotropy Energy of Spherical Nanomagnets

Throughout this thesis, spherical nanomagnets, so-called *magnetic nanoparticles*, are considered, whose high geometric symmetry influence the anisotropy contributions as follows: For ideally spherical nanoparticles, shape anisotropy contributions average to zero, therefore, $\varepsilon_{\mathsf{ms}} = 0$. Note that the same argument should hold for surface anisotropy contributions. However, in reality, the surface roughness and spin disorder of the nanostructure of nanoparticles induce an effective surface anisotropy, $\varepsilon_{\mathsf{sur}} \neq 0$. Lastly, the magnetoelastic anisotropy contributions are very small due to the nanoparticle small size and are therefore neglected, $\varepsilon_{\mathsf{me}} \approx 0$. Hence, the net anisotropy energy reduces to

$$\varepsilon_{\mathsf{ai}} \approx \varepsilon_{\mathsf{mc}} + \varepsilon_{\mathsf{sur}}, \tag{2.21}$$

which can be rewritten in terms of eqs. (2.13) and (2.14) (depending on uniaxial or cubic crystal structure), containing the modified effective anisotropy constants, combining bulk and

surface anisotropy contributions from eq. (2.19):

$$\varepsilon_{\mathsf{ai}}^{\mathsf{u}} = K_{\mathsf{eff,u}} V \cdot (\boldsymbol{m} \cdot \boldsymbol{n})^2, \quad \text{with} \quad K_{\mathsf{eff,u}} = K_{\mathsf{u}} + \frac{6}{d} K_{\mathsf{S}} \tag{2.22}$$

and

$$\varepsilon_{\mathsf{ai}}^{\mathsf{c}} = K_{\mathsf{eff,c_1}} V \cdot (\alpha_1^2 \alpha_2^2 + \alpha_2^2 \alpha_3^2 + \alpha_3^2 \alpha_1^2) + K_{\mathsf{eff,c_2}} V \cdot \alpha_1^2 \alpha_2^2 \alpha_3^2, \tag{2.23}$$

$$\text{with} \quad K_{\mathsf{eff,c_1}} = K_{\mathsf{c_1}} + \frac{6}{d} K_{\mathsf{S}} \quad \text{and} \quad K_{\mathsf{eff,c_2}} = K_{\mathsf{c_2}} + \frac{6}{d} K_{\mathsf{S}}.$$

2.1.3. The Origin of Superparamagnetism

When decreasing the dimensions of a ferromagnet (or antiferro- or ferrimagnet as well) below a certain size, it is energetically no longer efficient to form domain walls (cf. Section 2.1). Magnetic objects below this size will be called *magnetic nanoparticles* (MNP) or simply *(magnetic) particles* throughout this thesis. This critical size is $d < 100$ nm for typical MNP materials like Fe_3O_4, FePt or nickel [23].

For a quantitative description, one assumes a simple system of only next-neighbor exchange interaction and uniaxial anisotropy, eqs. (2.8) and (2.12), in which the energy is given by

$$\varepsilon = K_{\mathsf{u}} V \sin^2 \theta - |\boldsymbol{m}||\boldsymbol{H}| \cos(\theta). \tag{2.24}$$

Equation (2.24) describes the energy landscape in dependence of θ, the angle between the direction of magnetization and the easy axis. $\varepsilon(\theta)$ is plotted in Fig. 2.5 and has two minima: one at $\theta = 0$ with $\varepsilon_1 = -|\boldsymbol{m}||\boldsymbol{H}|$ and the other one at $\theta = \pi$ with $\varepsilon_2 = +|\boldsymbol{m}||\boldsymbol{H}|$. The one maximum is at $\theta = \arccos(-|\boldsymbol{m}||\boldsymbol{H}|/(2K_{\mathsf{u}}V))$ with $\varepsilon_{\mathsf{m}} = K_{\mathsf{u}} V \cdot (1 + (|\boldsymbol{m}||\boldsymbol{H}|/(2K_{\mathsf{u}}V))^2)$. At
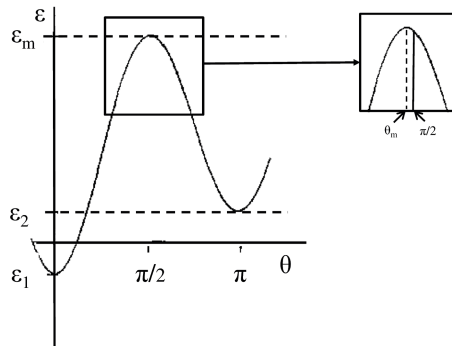
Fig. 2.5.: Energy ε for spherical magnetic particles with uniaxial anisotropy. The two minima at $\theta = 0$ and $\theta = \pi$ are separated by an energy barrier caused by anisotropy with the maximum ε_{m} at $\theta_{\mathsf{m}} = \arccos(-|\boldsymbol{m}||\boldsymbol{H}|/(2K_{\mathsf{u}}V))$ (s. inset for zoom). Adapted from [18] and inspired by [13].

thermal equilibrium the magnetization, $\boldsymbol{M}$, resides in the vicinity of the minima $\varepsilon_{1,2}$, separated by the energy barrier $\Delta E_{1,2} = \varepsilon_m - \varepsilon_{1,2}$. The initial position of the particle (whether minimum

1 or 2) is determined by the initial direction of the magnetization. The magnetization can flip its direction if the thermal energy exceeds the energy barrier, e. g. when thermally activated. The rate of flips, ν, across the energy barrier from one minimum to the other is approximated by $\nu \propto \exp(-(K_\mathrm{u}V(1 \pm (H_0 M_\mathrm{S})/(2K_\mathrm{u}))^2)/(k_\mathrm{B}T))$. ν is independent of the direction of the flips in the case of $\boldsymbol{H} = 0$ (i. e. the energy barrier is of equal height, $\Delta E_1 = \Delta E_2$). The average time $\tau = \frac{1}{\nu}$ between one flip of $\boldsymbol{M}$ between the two minima due to thermal activation is called *relaxation time*:

$$\tau = \tau_0 \cdot e^{\psi}, \tag{2.25}$$

$$\text{with} \quad \tau_0 = \frac{M_\mathrm{S}}{2K_\mathrm{u}\gamma} \cdot \sqrt{\frac{\pi}{\psi}}, \ \psi = \frac{K_\mathrm{u}V}{k_\mathrm{B}T}$$

and the electron gyromagnetic ratio $\gamma_0 = 1.76 \cdot 10^{11}$ rad $\cdot$ Hz/T. Obviously, the relaxation time is exponentially dependent on the particle magnetic volume, $V = V_\mathrm{M} = \frac{1}{6}\pi d_\mathrm{M}^3$, with the particle magnetic size (diameter), d_M: Within a rather short range of decreasing d_M, the relaxation time changes rapidly from large to small values by several orders of magnitude.

Superparamagnetism can be observed if measuring the particle magnetization over a specific time t_exp: If $\tau \gg t_\mathrm{exp}$, no change in magnetization is observed during the experiment. However, if $\tau \ll t_\mathrm{exp}$ holds, the magnetization vector flips back and forth many times during the experiment, as thermal fluctuations dominate anisotropy effects. Therefore for $\boldsymbol{H} = 0$, the measured value of magnetization averaged over the time t_exp is zero. Whereas for a sufficiently high field the magnetization $\boldsymbol{M}$ aligns with the applied field against the preferential direction defined by anisotropy, i. e. $\boldsymbol{H} \geq \boldsymbol{H}_\mathrm{K}$ (cf. eq. (2.15)). As described in Section 2.1, $\boldsymbol{M}$ reaches saturation for $|\boldsymbol{H}| > H_\mathrm{C}$. The interaction energy between $\boldsymbol{M}$ and $\boldsymbol{H}$ can be described by simplifying eq. (2.24) to $\varepsilon = -|\mathbf{m}||\mathbf{H}|\cos\theta$ (cf. eq. (2.38) in the following Section). Hence, the magnitude of magnetization M_H parallel to an applied field is described as the average of the angle θ over many particles

$$|\boldsymbol{M}_\mathrm{H}| = |\boldsymbol{M}| \cdot \langle \cos\theta \rangle = M_\mathrm{S} \cdot L(\xi), \tag{2.26}$$

where

$$L(\xi) = \coth(\xi) - \frac{1}{\xi} \tag{2.27}$$

$$\text{with } \xi = \frac{\boldsymbol{m} \cdot \boldsymbol{H}}{k_\mathrm{B}T} = \frac{\mu_0 V_\mathrm{M} M_\mathrm{S} H_0}{k_\mathrm{B}T}, \tag{2.28}$$

with the amplitude of the applied field H_0. $L(\xi)$ is called the *Langevin function*, which is also the limit of the Brillouin function (eq. (2.7)) for high spin quantum numbers, $S \to \infty$. Note that $L(\xi)$ is valid for non-interacting magnetic moments that are assumed to be homogeniously distributed inside the magnet (isotropic distribution) [24]. Furthermore, the Langevin function is defined under the assumption that MNP are always at thermal equilibrium, i. e. that the applied

field vector, $\boldsymbol{H}$ is always parallel to the magnetization vector of the MNP, $\boldsymbol{M}$. This assumption is only true for static applied fields, as otherwise, the MNP show relaxation phenomena, which is why in the next Section 2.2 the MNP relaxation including thermal fluctuations are discussed in detail.

Such a magnet behaves like a ferromagnet without hysteresis but with a high saturation magnetization, as several thousand spins are aligned as a result of the single domain nature (compared to only single spins in paramagnets). This phenomenon of "loss of ferromagnetism" in small particles in dependence of the time-scale of the experiment and the temperature is therefore known as *superparamagnetism* (SPM), with 'super' referring to the high saturation and 'paramagnetism' to the paramagnetic behavior. The respective $M(H)$-curve is depicted in Fig. 2.6a.

The Blocking Temperature Superparamagnetism may also be induced by temperature (not just by the time-scale of the experiment, as described in the paragraph above): Assuming a typical value of $t_{\mathsf{exp}} = 100\,\mathsf{s}$ for static magnetic measurements such as SQUID [14], one can see from the exponent in eq. (2.25), that a particle of known anisotropy constant K_{u} and known magnetic volume, $V = V_{\mathsf{M}}$, shows superparamagnetic behavior with $\tau \ll t_{\mathsf{exp}}$ for temperatures T high enough to induce thermal fluctuations of the particle's magnetic moment. Decreasing the temperature, superparamagnetism is lost and the particle's magnetic moment will be blocked for $\tau \geq t_{\mathsf{exp}}$. The temperature where $\tau = t_{\mathsf{exp}}$ holds is denoted as the *blocking temperature*, $T = T_{\mathsf{B}}$. By measuring the sample magnetization as a function of temperature in zero-field-cool (ZFC) experiments, the characteristic blocking temperature of the whole particle size distribution can be estimated. Furthermore, the mean anisotropy energy barrier, $\Delta E = K_{\mathsf{eff}} V_{\mathsf{M}}$, can be estimated and from this the effective anisotropy constant K_{eff} can be calculated—provided that the particle magnetic volume V_{M} is known. Comparing T_{B} of MNP of nominally equivalent particle magnetic size can also give a qualitative interpretation of the effect of magnetic dipole-dipole particle interactions. For a ZFC measurement, the sample is cooled from its superparamagnetic state with zero field applied, freezing all particles' magnetic moments in random orientation. At low temperature (e.g. $T = 5\,\mathsf{K}$), a small magnetic field, e.g. $H = 1\,\mathsf{mT}/\mu_0$ ($\approx 800\,\mathsf{A/m}$), is applied and the sample magnetization, M is recorded under gradual temperature increase. As T increases, M increases as well, as more and more particles are passing over their blocking temperature and their magnetic moments align with the applied field. Above a certain temperature, $T > T_{\mathsf{max}}$, M decreases again, as thermal fluctuations dominate the applied field, randomly orienting the particle magnetic moments again. From the peak in temperature, T_{max}, one can estimate the mean blocking temperature, T_{B}. In the complement field-cooled (FC) experiment, the small field, H, is applied at room temperature and the sample is consecutively cooled. As T decreases, M increases as the thermal fluctuations lessen and the particles' magnetic moments align with H upon blocking (freezing). M will continue to increase up to its saturation temperature, T_{sat}. For temperatures below the so-called branching temperature, $T < T_{\mathsf{bra}}$, the ZFC and FC magnetization curves branch off, while for $T > T_{\mathsf{bra}}$ the ZFC and FC curves superimpose (i.e. $M_{\mathsf{ZFC}} = M_{\mathsf{FC}}$), as all particles relax driven by thermal fluctuation. An exemplary ZFC-FC curve is depicted in Fig. 2.6b.
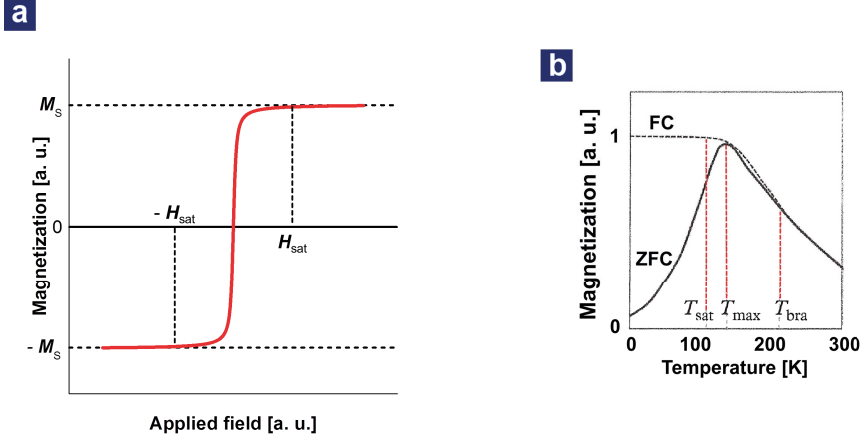
Fig. 2.6.: (a) magnetization curve of a superparamagnetic material; no hysteresis is measured. The saturation magnetization, M_S, is reached for applied fields $|H_0| > H_{sat}$. (b) Zero-field-cooled/field-cooled (ZFC-FC) magnetization curves; the ZFC and FC curves separate for $T \leq T_{bra}$, the ZFC curve peaks at $T = T_{max}$, and the FC curve saturates for $T \leq T_{sat}$. (b) adapted from [14].

2.2. Physics of Magnetic Particle Relaxation

When MNP are exposed to an external alternating magnetic field (AMF),

$$H_{ac}(t) = H_0 \cdot \cos(2\pi f \cdot t), \tag{2.29}$$

with the field amplitude, H_0, the frequency, f, and the time of exposure, t, they begin to rotate with the magnetic field. At the same time, their internal magnetic moment $\boldsymbol{m}$ with

$$|\boldsymbol{m}| = \mu_0 M_S V_M, \tag{2.30}$$

where M_S is the saturation magnetization, $V_M = \frac{\pi}{6}d_M^3$ the particle magnetic volume and μ_0 the permeability of free space, flips with a certain probability dependent on thermal energy $\varepsilon_{therm} = k_B \cdot T$. This process of simultaneous rotation and flipping of the particle's magnetic moment is denoted as *relaxation*. In other words, there two ways for the magnetic moment to relax in a particle: *Brownian relaxation*, which describes the rotation of the entire particle relative to its surrounding and *Néel relaxation*, describing the internal rotation of the magnetic moment, while the particle itself remains stationary [23, 25] (s. Fig. 2.7). At zero-field, their contributions can be described via the characteristic Brownian and Néel relaxation times, τ_B and τ_N, respectively, which are given by:

$$\tau_B = \frac{\pi \eta}{2k_B T} \cdot d_H^3 \tag{2.31}$$

$$\tau_{\mathsf{N}} = \tau_0 \cdot \exp(\frac{\Delta E}{k_{\mathsf{B}}T}) \tag{2.32}$$

with the anisotropy energy barrier ΔE (which is typically $\Delta E = K_{\mathsf{eff}} \cdot V_{\mathsf{M}}$, cf. eq. (2.25)), the viscosity of the carrier liquid η, and the particle hydrodynamic size d_{H}. As shown in the
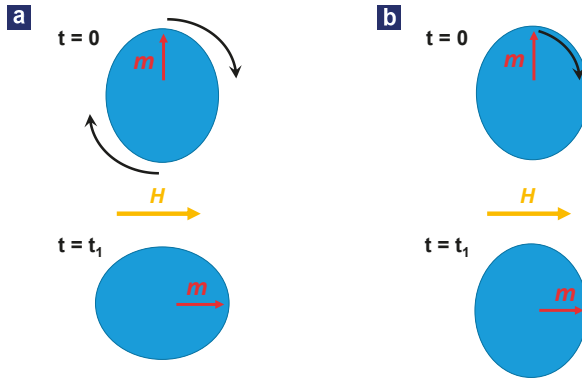
Fig. 2.7.: Schematic diagram of magnetic particle relaxation processes in the presence of a magnetic field $\boldsymbol{H}$, which is switched on at time $t = 0$: (a) particle rotation by revolving the entire particle relative to its surrounding while the magnetic moment $\boldsymbol{m}$ remains stationary, called Brownian relaxation. (b) relaxation of the magnetic moment $\boldsymbol{m}$, while the particle remains stationary relative to its surrounding, denoted as Néel relaxation. Note that $\boldsymbol{m}$ is aligned with $\boldsymbol{H}$ for both cases at time $t = t_1$. Note further that particles are drawn as prolate spheroids for emphasis of the relaxation mechanism; in reality, MNP are assumed to be spherical.

previous Section 2.1.3, the magnetization dynamics of MNP can be described in terms of the Langevin function $L(\xi)$, Eq. (2.27). However, $L(\xi)$ assumes an isotopic distribution of spins within MNP [24] and therefore does not account for magnetic anisotropy. Furthermore, it is valid only for thermal equilibrium and does not consider particle relaxation processes. Only if the change in the applied field is slow enough for the magnetization of the MNP to follow the field, i.e. the relaxation time τ is much smaller than applied field frequency, $\tau \ll 1/f$, relaxation effects can be neglected and $L(\xi)$ accurately describes the magnetization of the MNP [24].

Applications such as magnetic fluid hyperthermia and magnetic particle imaging, however, rely on relatively high field amplitudes $H_0 \sim 10\,\mathrm{mT}$ and frequencies $f \sim 100\,\mathrm{kHz}$, that force the MNP response to the applied field well into the non-equilibrium regime, where $\tau \sim 1/f$. Here, particle relaxation is driven by the applied field $\boldsymbol{H}$ and furthermore influenced by magnetic anisotropy as well as by thermal fluctuations, overall resulting in hysteresis effects. These relaxation contributions to the MNP magnetization can only be accurately characterized by combined Néel-Brownian rotation relaxation dynamics, which are described mathematically as follows: The internal magnetic moment of a particle, $\boldsymbol{m}_i$, rotates within the particle magnetic volume as described by the Landau-Lifshitz-Gilbert (LLG) equation [26, 27]:

$$\frac{\mathrm{d}\boldsymbol{m}_i}{\mathrm{d}t} = \frac{\gamma_0}{1+\alpha'^2} \cdot (\boldsymbol{H}_{\mathsf{eff}} \times \boldsymbol{m}_i + \alpha' \cdot \boldsymbol{m}_i \times (\boldsymbol{H}_{\mathsf{eff}} \times \boldsymbol{m}_i)), \tag{2.33}$$

with the electron gyromagnetic ratio γ_0, the (phenomenological) damping parameter $\alpha' \in [0,1]$ and the effective field $\boldsymbol{H}_{\text{eff}}$ (defined below, eq. (2.35)). Similarly, the Brownian rotation dynamics can be described in terms of a generalized torque [28], $\boldsymbol{\Theta}$, acting on the easy axes of a particle, $\boldsymbol{n}_i$, and depending on the surrounding fluid viscosity, η, and the hydrodynamic volume, $V_{\text{H}} = \frac{\pi}{6} d_{\text{H}}^3$:

$$\frac{\mathrm{d}\boldsymbol{n}_i}{\mathrm{d}t} = \frac{\boldsymbol{\Theta}}{6\eta V_{\text{H}}} \times \boldsymbol{n}_i. \tag{2.34}$$

These two differential equations, eqs. (2.33) and (2.34), describe the combined Néel-Brownian rotation relaxation dynamics for the general case of non-zero fields and at non-equilibrium conditions. The physics governing the relaxation process is encoded in $\boldsymbol{H}_{\text{eff}}$ and $\boldsymbol{\Theta}$, which are determined using the Helmholtz free energy $F = U - T \cdot \Sigma$ of the system, with the internal energy U, temperature T and entropy Σ. When considering monodisperse MNP, entropy is negligible, $\Sigma \approx 0$, so that the effective field and generalized torque read:

$$\boldsymbol{H}_{\text{eff}} = \frac{1}{\mu_0} \frac{\partial F}{\partial \boldsymbol{m}} \approx \frac{1}{\mu_0} \frac{\partial U}{\partial \boldsymbol{m}} \tag{2.35}$$

and

$$\boldsymbol{\Theta} = \frac{\partial F}{\partial \boldsymbol{n}} \times \boldsymbol{n} \approx \frac{\partial U}{\partial \boldsymbol{n}} \times \boldsymbol{n}. \tag{2.36}$$

The internal energy, U, includes contributions arising from the applied field $\boldsymbol{H}$ (ε_{Zee}), particle interaction ($\varepsilon_{\text{pp-IA}}$) and magnetic anisotropy (ε_{ai}):

$$U = \varepsilon_{\text{Zee}} + \varepsilon_{\text{pp-IA}} + \varepsilon_{\text{ai}}, \tag{2.37}$$

with the Zeeman term[2]

$$\varepsilon_{Zee} = -\boldsymbol{m} \cdot \boldsymbol{H}, \tag{2.38}$$

the magnetic dipole-dipole interaction exerted on an individual particle, with magnetic moment $\boldsymbol{m_0}$ (cf. eq. (2.30)) located at an arbitrary point R_0, by all other particles that are at the distance $\boldsymbol{r}_i$ away from R_0 and have the magnetic moment $\boldsymbol{m}_i$

$$\varepsilon_{\text{pp-IA}} = \sum_i \frac{\mu_0}{4\pi r_i^3} \left(\frac{3(\boldsymbol{m_0} \cdot \boldsymbol{r}_i) \cdot (\boldsymbol{m}_i \cdot \boldsymbol{r}_i)}{r_i^2} - \boldsymbol{m_0} \cdot \boldsymbol{m}_i \right), \tag{2.39}$$

and the magnetic anisotropy energy, ε_{ai}, as described above in eqs. (2.22) or (2.23) for uniaxial or cubic anisotropy, respectively.

This set of coupled equations, eqs. (2.33) - (2.37), describes the combined rotational relaxation dynamics fully deterministically. However, in order to include thermal fluctuation, a stochiastic

---

[2]The Zeeman energy describes the applied (external) field energy inside a magnetized body of volume V. Its more general form reads $\varepsilon_{\text{Zee}} = -\mu_0 \int \boldsymbol{M} \cdot \boldsymbol{H} \mathrm{d}V$, which was solved here already for spherical MNP [14].

term must be introduced to eqs. (2.35) and (2.36), giving [29]:

$$\boldsymbol{H}_{\text{eff}} = \frac{1}{\mu_0} \frac{\partial U}{\partial \boldsymbol{m}} + \boldsymbol{H}_{\text{th}}, \tag{2.40}$$

and

$$\boldsymbol{\Theta} = \frac{\partial U}{\partial \boldsymbol{n}} \times \boldsymbol{n} + \boldsymbol{\Theta}_{\text{th}}. \tag{2.41}$$

These thermally generated fields, $\boldsymbol{H}_{\text{th}}$, and torques, $\boldsymbol{\Theta}_{\text{th}}$, are expressed as Gaussian-distributed with an approximately flat frequency distribution of noise (equivalent to white noise) defined under the initial conditions

$$H_{\text{th}}^i(t = 0) = 0 \quad \text{and} \quad \Theta_{\text{th}}^i(t = 0) = 0, \tag{2.42}$$

and with zero mean

$$\langle H_{\text{th}}^i(t) \rangle = 0 \quad \text{and} \quad \langle \Theta_{\text{th}}^i(t) \rangle = 0. \tag{2.43}$$

The magnitude of the thermal fluctuations is encoded in the averaged variances reading:

$$\langle H_{\text{th}}^i(t) H_{\text{th}}^j(t') \rangle = \frac{2k_{\text{B}}T}{\gamma_0 |\mathsf{m}|} \frac{1 + \alpha'^2}{\alpha'} \delta_{ij} \delta(t - t'), \tag{2.44}$$

$$\langle \Theta_{\text{th}}^i(t) \Theta_{\text{th}}^j(t') \rangle = 12 k_{\text{B}} T \eta V_H \delta_{ij} \delta(t - t'), \tag{2.45}$$

with $i, j \in x, y, z$, Cartesian spacial coordinates. The magnitude of fluctuations depends on MNP parameters, as well as the Boltzmann constant, k_{B}, and the temperature, T. Furthermore, the magnitude is unambiguously defined in 3D-space (Kronecker-Delta function δ_{ij}) and in time (Dirac-Delta function $\delta(t - t')$). The introduction of thermal fluctuations by inserting eqs. (2.40) and (2.41) in eqs. (2.33) and (2.34) makes this a set of coupled *stochastic differentiable equations* (SDE), whose solution requires stochastic calculus schemes and numerical integration, discussed in detail in the next Chapter 3; esp. Section 3.2.1.

In practice, calculating the relaxation dynamics of a single particle is meaningless for predicting magnetization loops, $M(H)$, for MNP solutions of typically concentrations of $\sim 10^{13}$ individual particles per mL. Therefore, an ensemble of at least 1000 particles is usually simulated and by calculating the ensemble average magnetization for different applied fields, one can predict $M(H)$ for any arbitrary set of particles core or hydrodynamic sizes, anisotropy constants, saturation magnetizations and thermal fluctuations. This kind of numerically solving stochastic problems in the limit of large populations in an ensemble is commonly called a *Monte Carlo* method. Throughout this thesis, the simulations based on magnetic particle relaxation will therefore be referred to as *Monte Carlo (MC-)simulations*, henceforth. The implementation and

extraction of data from such MC-simulated $M(H)$-loops is presented in detail in Chapter 3, Section 3.2.

2.3. Physics of Magnetic Particle Imaging

The relaxation of superparamagnetic MNP in an AMF described above in Sections 2.1.3 and 2.2 can be exploited for direct (i. e. positive contrast[3]) imaging of particles in magnetic particle imaging (MPI) [30]. In MPI, the derivative of the MNP magnetization $M(t)$, $M'(t) = \mathrm{d}M(t)/\mathrm{d}H$ is measured by a receive coil via electromagnetic induction (s. below). The MNP are excited by an external sinusoidal AMF of typical field amplitude $H_0 \leq 20\,\mathrm{mT}/\mu_0$ and frequency $f \sim 25\,\mathrm{kHz}$. MPI relies on the superparamagnetic non-linear response of $M(t)$, described by the Langevin function $L(\xi(H))$ (cf. eq. (2.27)) [31]: When a sufficiently high field amplitude is applied, $M(t)$ saturates and $M'(t)$ is zero. Contrastingly, $M'(t)$ will only be non-zero, at sufficiently small fields that do not saturate $M(t)$.

MPI uses a send coil to apply a sinusoidal alternating magnetic field (AMF), cf. eq. (2.29), to change the magnetization of MNP, $M'(t)$. By using Faraday's law of induction, $M'(t)$ can be measured from the voltage, $V(t)$, induced in a receive coil by a temporary change in the magnetic induction, $\mathrm{d}\boldsymbol{B}/\mathrm{d}t$, as will be outlined in the following: For simplification, considering the receive coil as a single conductor loop spanning the surface S_{RC}, then the voltage at the end points of the loop reads according to Faraday's law in integral form:

$$V(t) = \oint_{\partial S_{\mathrm{RC}}} \boldsymbol{E}(\boldsymbol{l}) \cdot \mathrm{d}\boldsymbol{l} = -\frac{\mathrm{d}}{\mathrm{d}t}\Phi, \tag{2.46}$$

with the electric field, $\boldsymbol{E}(\boldsymbol{l})$, induced along the conductor loop of length $\boldsymbol{l}$, by the magnetic flux, Φ, defined by

$$\Phi = \oint_{S_{\mathrm{RC}}} \boldsymbol{B}(\boldsymbol{r}) \cdot \mathrm{d}\boldsymbol{A}, \tag{2.47}$$

through the surface of the receive coil S_{RC}, the magnetic induction $\boldsymbol{B}$ and the differential vector $\mathrm{d}\boldsymbol{A}$ perpendicular to S_{RC}, as outlined in Fig. 2.8. Inserting eq. (2.47) in eq. (2.46) and knowing that $\boldsymbol{B} = \mu_0(\boldsymbol{H} + \boldsymbol{M})$ from Section 2.1, eq. (2.2), one acquires:

$$V(t) = -\mu_0\frac{\mathrm{d}}{\mathrm{d}t} \oint_{S_{\mathrm{RC}}} \boldsymbol{H}(\boldsymbol{r},t) \cdot \mathrm{d}\boldsymbol{A} - \mu_0\frac{\mathrm{d}}{\mathrm{d}t} \oint_{S_{\mathrm{RC}}} \boldsymbol{M}(\boldsymbol{r},t) \cdot \mathrm{d}\boldsymbol{A} = V_{\mathrm{AMF}}(t) + V_{\mathrm{MNP}}(t). \tag{2.48}$$

Eq. (2.48) shows that the (time-varying) alternating magnetic field (AMF), $\boldsymbol{H}(\boldsymbol{r},t)$, is directly picked up by the receive coil as the voltage $V_{\mathrm{AMF}}(t)$ and superimposed with the voltage $V_{\mathrm{MNP}}(t)$ induced by the MNP's change in magnetiaztion. The latter can be expressed as an integration over the sample volume, V, containing MNP within the receive coil by using the law of reciprocity

---

[3]Positive contrast is defined by the fact that the imaging signal is proportional to the amount of material generating the signal.
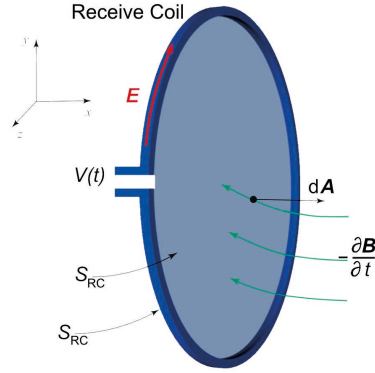
Fig. 2.8.: The voltage, $V(t)$, induced by a temporal change in the magnetic induction, B, in a receive coil spanning the surface S_{RC}. The voltage is equal to the line integral of the electric field E along the receive coil loop. Adapted from [32].

[32], yielding:

$$V_{MNP}(t) = -\mu_0 \int_V \zeta(V) \cdot \frac{dM(V,t)}{dt} dV, \tag{2.49}$$

with the coil sensitivity ζ, summarizing the geometrical parameters of the coil. To discriminate the superimposed voltages one chooses a sinusoidal AMF for the MNP excitation, $H_{ac}(t) = H_0 \cdot \cos(2\pi f \cdot t)$, cf. eq. (2.29): Then, the particle signal shows two distinct peaks, which are clearly distinguished from the excitation signal, as is shown in Fig. 2.9. Due to the sinusoidal AMF, the particle and excitation signal can be mathematically decoupled in the frequency domain by expanding into a discretized Fourier series [32]:

$$V(t) = \sum_{k=-\infty}^{\infty} \hat{V}_k \cdot \exp(2\pi \cdot ik \cdot f \cdot t). \tag{2.50}$$

Its spectrum consists of discrete lines at multiples of the frequency of the applied AMF, f:

$$f_k = k \cdot f, \qquad k \in \mathbb{Z}. \tag{2.51}$$

f_k will be denoted as *harmonics* throughout this thesis. Since $V(t)$ is real, the Fourier coefficients follow the relation:

$$\hat{V}_k = f \cdot \int_0^{1/f} V(t) \cdot \exp(-2\pi \cdot ik \cdot f \cdot t) dt \tag{2.52}$$

$$= f \cdot \int_0^{1/f} (V(t) \cdot \exp(2\pi \cdot ik \cdot f \cdot t))^* dt \tag{2.53}$$

$$= (\hat{V}_{-k})^*. \tag{2.54}$$

From eq. (2.54) it follows, that the negative frequencies do not carry any additional information on the MPI signal and are therefore neglected henceforth.

Since the excitation AMF is purely sinusoidal, the contribution of the excitation signal, V_{AMF},
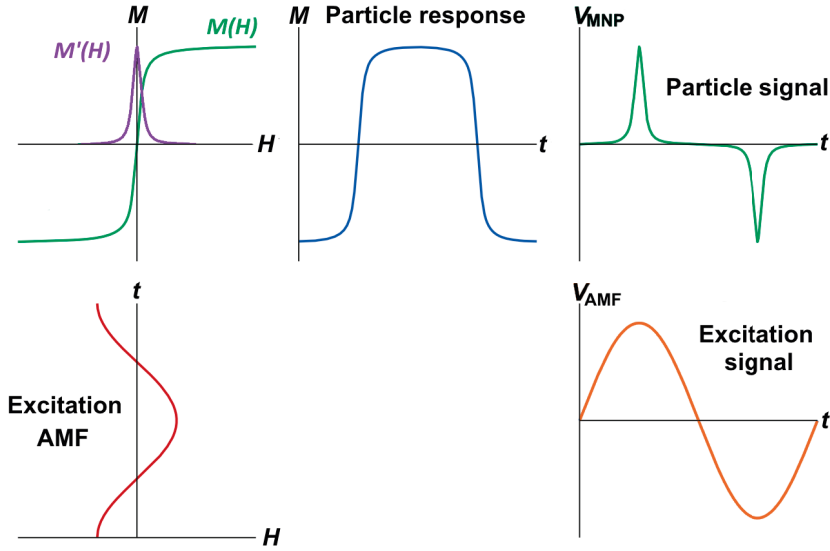
Fig. 2.9.: Schematic of the signal generation of MPI (reading from bottom left clockwise to bottom right): Applying a sinusoidal excitation field, H, drives the MNP magnetization M from negative saturation through zero to positive saturation according to the Langevin function $L(\xi)$. The derivative of MNP magnetization, $M'(H) = dM/dH$, is only non-zero for small field amplitudes. The MNP response to the applied field, $M(t)$, resembles a rectangular function. The voltage, V_{MNP}, induced in the receive coil by the MNP shows two distinct peaks as the particle signal, directly resulting from $M'(H)$, while the excitation signal resembles a sinusoidal function. Adapted from [32].

in frequency space is limited to a single peak at the frequency f. Contrastingly, the non-linear relationship $M(H)$ of the particles allows particle signal contributions not just for f but rather for all higher harmonics, f_k. This is illustrated in Fig. 2.10, where the excitation signal, the particles signal and their superposition is shown in time and frequency domain. From this one observes that the particle signal is hardly detected in the superposition signal in the time domain. This is due to the low amplitude of the particle signal compared to the excitation signal[4] [32]. In the frequency domain however, the particle signal can be easily seen in the superimposed signal spectrum for higher harmonics. Only the first harmonic, $f = f_{k=1}$, is covered by the excitation signal. By ignoring the first harmonic, one removes the influence of the excitation signal as well as any background signal. Therefore, all higher harmonics of the MPI signal carry only the undisturbed particle signal and can be used for imaging[5]. The fact that the even harmonics are missing in the signal spectrum a consequence of the non-linear MNP response (described by the Langevin function) to the sinusoidal excitation AMF, as derived in Appendix A.1.1.

To image a sample volume, MPI uses a field-free-point (FFP) to spatially encode the particle signal according to the non-linear magnetization particle response to the AMF. Since the

---

[4]For a typical MPI experiment the difference between V_{MNP} and V_{AFM} ranges from six to ten orders of magnitude, depending on the MNP concentration imaged, the coil sensitivities and the quality of the MNP in order to generate a good signal.

[5]The higher harmonics include all non-linear contributions to $M(H)$ in the scanned sample volume. This usually includes MNP only for an in vivo MPI scan, as e. g. bodily iron is present in the atomic form, therefore much smaller than the MNP and with a linear magnetization response for the considered AMF range [32].

Time domain   Frequency domain
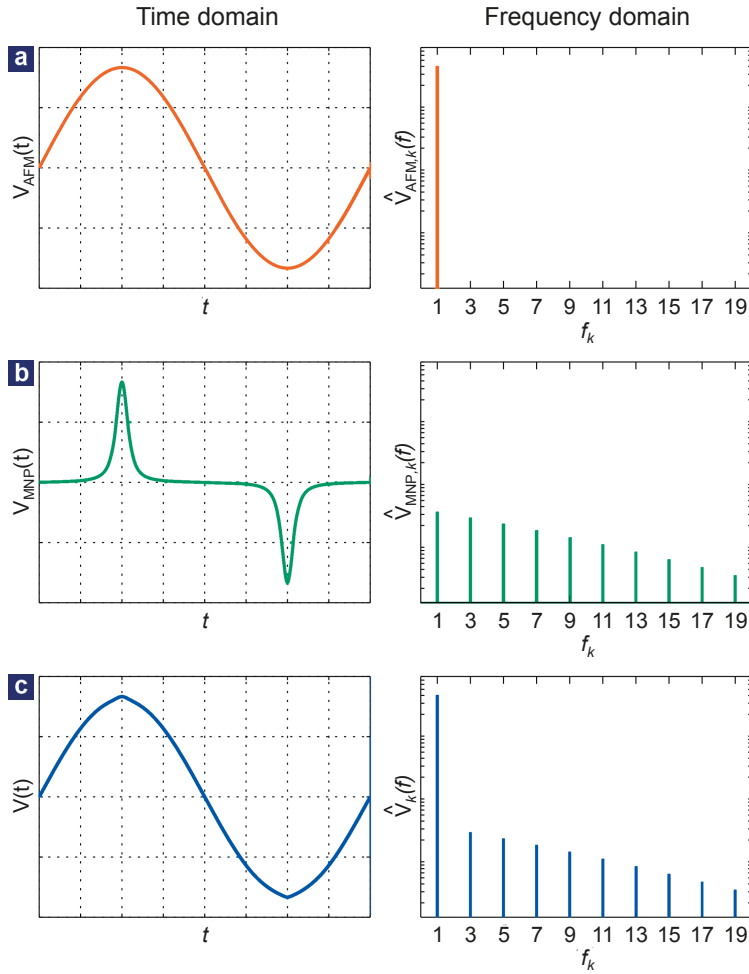
Fig. 2.10.: Comparison of the the signal induced in the receive coil for a sinusoidal AMF in time domain and frequency domain for (a) the excitation signal, (b) particle signal and (c) superposition of (a) and (b). Adapted from [32].

excitation AMF is known (cf. eq. (2.29)), eq. (2.49) can be expanded by $\frac{dH}{dH}$, reading:

$$V_{\mathrm{MNP}}(t) = -\mu_0 \int_V \boldsymbol{\zeta}(V) \cdot \frac{d\boldsymbol{M}(V,t)}{d\boldsymbol{H}(t)} \cdot \frac{d\boldsymbol{H}(t)}{dt} dV =: -\mu_0 \int_V \boldsymbol{\zeta}(V) \cdot M'(H(t)) \cdot \boldsymbol{H}'(t) dV. \quad (2.55)$$

Only considering contributions by the MNP, $V_{\mathrm{MNP}} \propto M'(H(t))$ holds. Since the magnetization of MNP is described by the Langevin function, $M(H(t)) \propto L(\xi(H(t)))$ (cf. eq. (2.27)), the particle signal is determined by the derivative of the Langevin function:

$$L'(\xi(H(t))) := \frac{dL(\xi(H(t)))}{d\xi} = (\xi^{-2} - \sinh^{-2}(\xi)), \quad (2.56)$$

with $\xi = \frac{\mu_0 V_\text{M} M_\text{S} H_0}{k_\text{B} T}$. $L'(\xi(H(t)))$ has a maximum at $H = 0 \Rightarrow \xi = 0$ with $L'(\xi = 0) = 1/3$ and therefore particle response is maximal for $H = 0$. By scanning the FFP (or field-free line in more advanced systems) through a sample volume containing a MNP distribution, the signal induced in the receive coil is non-zero only where MNP are located at the FFP [33]. Around the FFP the MNP are saturated by a sufficiently high gradient field, and therefore do not generate a signal $V_\text{MNP} \propto M'(H(t))$. In this way, a MNP distribution can be conveniently mapped by gridding the particle signal to the location of the FFP (as depicted in Fig. 2.11).
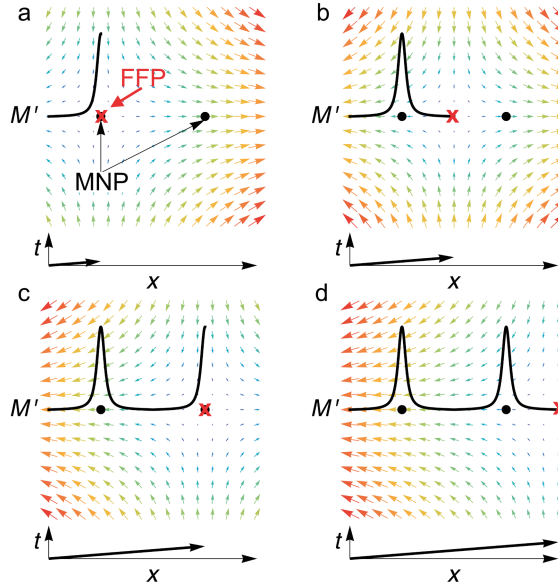
Fig. 2.11.: Characteristic response of MNP to a field-free point (FFP), generated by a combination of gradient fields and scanned along the x-axis at four different time points (a) through (d): The MNP response, $M'(H(t))$, is only non zero, when a distribution of MNP (symbolized as black point sources here) is crossed by the FFP. Note that $M'(H(t))$ is indicated as a black line here, showing the accumulated signal one line scanned by the FFP over time. Adapted from [34].

In practice, 2D- and 3D-MPI require complex trajectories of moving the FFP to record the particle signal efficiently [14,32]. Furthermore, the raw MPI data must be mathematically post-processed to reconstruct an MPI image [35–38]. Both concepts go beyond the scope of this thesis, but are covered in more detail in the references cited above.

The suitablility of MNP as MPI tracers is determined by the magnitude of $M'(H = 0)$, $|M'(H = 0)|$ (i. e. the signal intensity or MPI signal-to-noise ratio (SNR), respectively) and the full width at half maximum (FWHM)[6] of $M'(H)$, ΔH_FWHM, (i. e. the spacial resolution) [34]. The signal intensity can be derived from $M(H) = M_\text{S} \cdot L(\xi(H))$ (s. eq. (2.26)) and the derivative of the

---

[6] The full width at half maximum (FWHM) is defined as the width at which a (peak) function drops to 50% of its maximum value.

Langevin function (s. eq. (2.56)), yielding [32]:

$$|M'(H = 0)| = c \cdot \frac{|\boldsymbol{m}|^2 \cdot \mu_0}{3 k_B T}, \tag{2.57}$$

with the MNP concentration c, and particle magnetic moment $|\boldsymbol{m}| = \mu_0 \cdot M_S \cdot V_M$ (s. eq. (2.30)). The FWHM can be similarly approximated from the derivative of the Langevin function reading:

$$\Delta H_{\mathsf{FWHM}} = \frac{4.16 \cdot k_B T}{\mu_0 \cdot |\boldsymbol{m}|}. \tag{2.58}$$

From eq. (2.57) one sees that the particle signal is directly proportional to the MNP concentration. Therefore, MPI is a quantitative, positive contrast imaging technique, as the signal is directly related to the amount of the (MNP) tracer.

If a MPI scanner is not accessible easily, the suitablity of MNP as MPI tracers described by the signal intensity (eq. (2.57)) and the spacial resolution (eq. (2.58)), can be assessed by magnetic particle spectoscopy (MPS) measurements. MPS is basically a zero dimensional MPI scan [23], where a sinusoidal field is applied, $H_{\mathsf{ac}}(t)$ cf. eq. (2.29), with typical frequencies in the range of $f = (3 - 25)\,\mathrm{kHz}$ [34]. Since the sample volume, V, and coil sensitivity, ζ, are accessible, the particle signal induced in the receive coil from eq. (2.55) simplifies to [39, 40]:

$$V_{\mathsf{MNP}}(t) = -\mu_0 \cdot \zeta \cdot M'(H) \cdot H'(t), \tag{2.59}$$

with the MNP response $M'(H(t))$ and the derivative of the field $H'(t) = \mathrm{d}H(t)/\mathrm{d}t$. Rearranging eq. (2.59) for M' gives

$$M'(H(t)) = \frac{-1}{\mu_0 \cdot \zeta \cdot 2\pi f \cdot H_0} \cdot \frac{V_{\mathsf{MNP}}(t)}{\cos(2\pi f \cdot t)}. \tag{2.60}$$

Equivalently to an MPI scanner, the received signal, $V(t)$, is Fourier transformed $\mathcal{F}(V(t)) = \hat{V}_k(f_k)$ to derive the harmonic spectrum in the frequency domain [41]. Here, the first harmonic, $f = f_{k=1}$ is excluded usually as it carries the excitation signal (as discussed above) and to the remove background signal. Typically, the performance of MNP as MPI tracers is analyzed by comparing the MPS harmonic spectra: A higher absolute spectral magnitude indicates superior SNR of the MNP tracer (cf. eq. (2.57)) and a broader spectrum (i. e. smaller FWHM) indicates improved spacial resolution (2.58) [23, 32].

2.4. Physics of Magnetic Particle Heating

As described in Section 2.2 above, an ensemble of MNP relaxes under the influence of an applied alternating magnetic field (AMF), $H_{\mathsf{ac}}(t)$, c. f. eq. (2.29). Both relaxation processes, Brownian and Néel, require magnetic energy to align the magnetic moment parallel to the direction of the applied field. During the field-driven relaxation processes, heat is generated equivalent to

the magnetic energy consumed for this alignment. The heating rate is commonly referred to as the *specific loss power* (*SLP* [W/g]), defined as energy per unit time and per unit mass of nanoparticles [42]. It is defined in terms of the area of the hysteresis loop $M(H)$, denoted as A, the frequency f and the MNP materials' mass density ρ:

$$SLP = \frac{1}{\rho} \cdot A \cdot f \tag{2.61}$$

Two main theories are commonly used to describe the SLP on the basis of simple MNP magnetization models: The *Stoner-Wohlfarth Model Based Theory* (SWMBT), which approximates the hysteresis loop $M(H)$ for large particles in high fields (typically $d_\mathsf{M} > 18\,\text{nm}$ and $H_0 > 20\,\text{mT}/\mu_0$ for magnetite) and the *Linear Response Theory* (LRT), based on the MNP linear relaxation approximation in low fields for small particles (typically $d_\mathsf{M} < 10\,\text{nm}$ and $H_0 < 15\,\text{mT}/\mu_0$ for magnetite). In the following, SWMBT and LRT will be discussed briefly, building an understanding of the physics of magnetic particle heating.

Note that furthermore, a third way of simulating the hysteresis loop $M(H)$ within the framework of particle relaxation (s. previous Section 2.2) exists, which is generally not restricted to a certain field amplitude or particle size. These two theories will be compared to results from the third theory of simulating $M(H)$ in Chapter 3.

Stoner-Wohlfarth Model Based Theory of Magnetic Particle Heating

This theory is based on the Stoner-Wohlfarth model and describes the hysteresis losses for single-domain magnetic particles in the ferromagnetic regime with uniaxial anisotropy [43]. At $H_{\mathsf{ac}} = 0$ and for fields below a certain amplitude (definded below), the magnetic moments of MNP are aligned along the easy axes due to anisotropy, which can be expressed in terms of an anisotropy field, H_K, eq. (2.15). The magnetic moments of the MNP remain aligned, until a sufficiently high field is applied, which can be either expressed in terms of the anisotropy field H_K or the coercivity H_C, (cf. Section 2.1): For $H_0 \geq H_C \approx \frac{H_\mathsf{K}}{2}$, the magnetic moments align with the direction of the applied field $H_{\mathsf{ac}}(t)$ and develop a hysteresis loop $M(H)$. In its original form, the Stoner-Wohlfarth model does not take thermal activation into account [44], thus is only valid for $T = 0$ or in the limit of infinite frequency $f \to \infty$.

Based on earlier works on the temperature dependency of the coercive field [45, 46], Carrey et al. [42] proposed an extension named Stoner-Wohlfarth model based theory for randomly oriented particles (SWMBT), calculating the hysteresis loop area, A, as:

$$A = 2\mu_0 \cdot M_\mathsf{S} \cdot H_\mathsf{C}(\kappa) \tag{2.62}$$

with the coercive field

$$H_C(\kappa) = 0.48 \cdot H_\mathsf{K} \cdot (1 - \kappa(T, f, H_0, V_\mathsf{M})^{0.8}) \tag{2.63}$$

which includes the anisotropy field H_K, eq. (2.15) and the dimensionless parameter

$$\kappa(T, f, H_0, V_\mathsf{M}) = \frac{k_\mathsf{B}T}{K_\mathsf{u}V_\mathsf{M}} \cdot \ln\Big(\frac{k_\mathsf{B}T}{4 \cdot \mu_0 H_0 \cdot M_\mathsf{S}V_\mathsf{M} \cdot f\tau_0}\Big), \tag{2.64}$$

where τ_0 is typically approximated as $\tau_0 \approx 10^{-10}\,\text{s}$ and a restriction of $\kappa \leq 0.7$ holds for eq. (2.63). Consequently, SWMBT is limited to high fields where $H_0 \geq H_\mathsf{C} \approx \frac{H_\mathsf{K}}{2}$ and generally to $\kappa < 0.7$. Experimental data on iron MNP support the validity of this concept for high field amplitudes of $H_0 = (15 - 60)\,\text{kA/m}$ [47], but do not consider the applicability at lower field amplitudes. One major drawback of SWMBT is the fact that it does not take particle relaxation processes into account and thereby neglects a fundamental effect of superparamagnetic particle relaxation on magnetic particle heating.

Linear Response Theory of Magnetic Particle Heating

This theory describes the magnetic particle heating in terms of a relaxation of the magnetic particle magnetization to equilibrium state within the material's linear response to the field, $M = \chi \cdot H$ (c.f. eq. (2.1)). Hence it is called linear response theory (LRT). It was derived under the assumption of an adiabatic system of monodisperse MNP by Rosensweig [48]. However, the linear response regime is limited to small fields and particle sizes, restricting the regime of validity of LRT. This limit is given by the ratio of magnetic versus thermal energy, in numbers $\xi \leq 1$, with

$$\xi = \frac{|\boldsymbol{m}| \cdot |\boldsymbol{H}|}{k_\mathsf{B}T} = \mu_0 \cdot \frac{M_\mathsf{S}V_\mathsf{M}}{k_\mathsf{B}T} \cdot H_0. \tag{2.65}$$

ξ is also called the reduced field parameter. For example, eq. (2.65) yields a limit of validity for LRT to a field amplitude $H_0 \leq 15.7\,\text{kA/m}$ for typical values of particle magnetic size of $d_\mathsf{M} = 10\,\text{nm}$ and saturation magnetization $M_\mathsf{S} = 400\,\text{kA/m}$ at temperature $T = 300\,\text{K}$.

LRT can be derived in the framework of the Debye theory of dipolar fluids [49] under the assumption of spherical and non-interacting MNP: Let the MNP be subjected to an AMF; then the magnetic susceptibility of MNP becomes complex and shows both real (χ') and imaginary (χ'') parts, describing the in-phase and out-of-phase (or loss) component, respectively. This complex AC-susceptibility reads

$$\hat{\chi} = \chi' + i\chi'' = \chi_0 \cdot \left(\frac{1}{1 + (2\pi f \cdot \tau_\mathsf{R})^2} + i\frac{2\pi f \cdot \tau_\mathsf{R}}{1 + (2\pi f \cdot \tau_\mathsf{R})^2}\right) = \frac{\chi_0}{1 + i2\pi f \cdot \tau_\mathsf{R}}, \tag{2.66}$$

containing the initial DC susceptibility $\chi_0 = \frac{\mu_0 M_\mathsf{S}^2 V_\mathsf{M}}{3k_\mathsf{B}T}$ and the effective relaxation time τ_R that it takes for the system to relax back to equilibrium after a small step in the magnetic field (defined below, eq. (2.70)). $\hat{\chi}$ and $H_\mathsf{ac}(t)$, from eqs. (2.66) and (2.29), respectively, are inserted in eq. (2.1), which yields for the magnetization:

$$M(t) = |\hat{\chi}| \cdot H_0 \cos(2\pi f \cdot t + \varphi), \tag{2.67}$$

$$\text{with } |\hat{\chi}| = \frac{\chi_0}{\sqrt{1 + (2\pi f \cdot \tau_R)^2}},$$

where φ is the phase lag between magnetization and the alternating magnetic field. In this way, the heat is generated by the magnetization vector lagging behind the driving field vector in LRT [42]. Simple mathematical observation indicates that eq. (2.29) and eq. (2.67) correspond to the parametric equations for an ellipse, wherefore the area of the resulting hysteresis loop $M(H)$ is given by

$$A = \pi \chi'' \cdot H_0^2, \tag{2.68}$$

$$\text{with } \chi'' = \chi_0 \cdot \frac{2\pi f \cdot \tau_R}{1 + (2\pi f \cdot \tau_R)^2}. \tag{2.69}$$

The relaxation time τ_R can be approximated by adding both relaxation processes yielding the effective relaxation time:

$$\tau_R^{-1} = \tau_N^{-1} + \tau_B^{-1}, \tag{2.70}$$

where τ_B is the Brownian relaxation time and τ_N the Néel relaxation time, given by eq. (2.31) and eq. (2.32), respectively. Note that it is widely assumed that the faster relaxation process will dominate the relaxation time.

2.5. Magnetic Fluid Hyperthermia in Tumor Therapy

This Section describes various aspects of magnetic fluid hyperthermia (MFH), first describing the present-day status of applying MFH, including the main challenges and promises in Section 2.5.1. As magnetic nanoparticles (MNP) used in MFH will inevitably interact with cells inside the body, Section 2.5.2 deals with a general description of pathways of particles inside cells. The nanoscale heating effects of intracellular MNP in MFH and their direct effects on cells are presented in Section 2.5.3. Finally, a treatment approach with MFH is motivated and described for pancreatic ductal adenocarcinoma (PDAC) in Section 2.5.4.

This Section is partly based on an original publication by the writer [50] (s. Appendix C). Where entire sentences are cited directly from the publication, this is marked with †.

2.5.1. Magnetic Fluid Hyperthermia in Tumor Therapy

The term *hyperthermia* derives from ancient Greek combining 'hyper' meaning *over* and 'thermia' meaning *heating*. Hyperthermia is applied to purposefully induce local heating in parts of the body with temperatures of $(42 - 46)\,°C$. At these elevated temperatures, the function and structure of many enzymes and proteins alters within cells, which can lead to apoptosis (induced cell death) [51]. Thus, hyperthermia is an alternative to open surgery, X-ray irradiation

and chemotherapy in modern tumor therapy [52]. Nevertheless, hyperthermia must be clearly distinguished from thermoablation, where temperatures up to 56°C are applied to destroy cells by necrosis and coagulation [53].

Hyperthermia can be applied using different techniques such as microwave [54] and laser irradiation [55], resistive heating via implanted electrode devices [56], and whole body treatment with water baths [57]. Additionally, *magnetic fluid hyperthermia* (MFH) offers a novel and promising approach [58, 59], which is also the main application focus of this thesis. In MFH, magnetic nanoparticles are accumulated locally by magnetic targeting or injection in target tumor tissue and subsequently heated by applying an external alternating field, as described in the previous Section 2.4. At the target tumor size, the MNP inevitably interact with the surrounding cells and tissue, leading to an uptake of MNP inside cells (s. Section 2.5.2 for details). Once internalized inside cells, the intracellular MNP can potentially deliver therapeutic heat from the inside of the cells, increasing the efficacy of MFH by so-called *nanoheating effects*, discussed in detail in Section 2.5.3.

The MNP material used for MFH should show colloidal stability, adjustable magnetic properties, low cytotoxicity, sufficient circulation time within the body during treatment and eventually appropriate biodegradability [60]. These requirements limit the MNP-type that can be used for MFH mainly to the magnetic iron oxides maghemite (γ-Fe_2O_3) and magnetite (Fe_3O_4), which are well tolerated in the human body [23, 61]. Within the field amplitudes, H_0, and frequencies, f, applied in hyperthermia ($H_0 < 25\,\text{mT}$, $f < 1\,000\,\text{kHz}$), these iron oxides display controllable heating characteristics. However, the field itself can stimulate non-selective and undesired heating within the body due to the formation of eddy currents [62]. The heat of such eddy currents Q_eddy depends on the field and the diameter of the induced current loop in the body, D^*, according to $Q_\text{eddy} \propto (D^* \cdot H_0 \cdot f)^2$ [62]. Medically, there is a limit to the AMF tolerated within the body, which experimentally has been determined to be $H_0 \cdot f < 4.9 \cdot 10^8\,\text{A}/(\text{m}\cdot\text{s})$ in 1984 [63]. The first successful clinical trials at the Charité Berlin, however, have shown slightly higher tolerances of $H_0 \cdot f < 1.4 \cdot 10^9\,\text{A}/(\text{m}\cdot\text{s})$ for fields applied to the head [64] and $H_0 \cdot f < 5.0 \cdot 10^8\,\text{A}/(\text{m}\cdot\text{s})$ for application of MFH at the lower body (rectum) [65]. Both tolerances agree well with the field-frequency limit of $H_0 \cdot f < 8.0 \cdot 10^8\,\text{A}/(\text{m}\cdot\text{s})$ suggested by the International Commission on Non-Ionizing Radiation Protection (ICNIRP) in their Guidelines for a public exposure limit to alternating magnetic fields [66, 67]. Depending on the desired medical application, either $1.4 \cdot 10^9\,\text{A}/(\text{m}\cdot\text{s})$ (head) or $0.5 \cdot 10^9\,\text{A}/(\text{m}\cdot\text{s})$ (body) will serve as the medical limit for the AMF throughout this thesis.

In hyperthermic treatment, both temperature T, and exposure time to elevated temperatures t_HT, have to be monitored closely, as their interaction with each other determines the cell's response in a complex manner: If cells are heated above $T > 43\,°\text{C}$ for a short time, the surviving cells prove more vulnerable to subsequent heating. This effect is known as step-down heating [68]. Contrastingly, if the exposure was $T < 43\,°\text{C}$, the surviving cells appear to be much more resistant to heating to even higher subsequent temperatures. Moreover, if cells are heated above $T > 43\,°\text{C}$ but afterwards incubated at $37\,°\text{C}$ for several days, they present

themselves more resistant to subsequent heating as well [69]. This process has been coined as thermotolerance [70] and been shown to exist for both healthy and tumor tissue [71]. In order to benefit from the effects of step-down heating, while avoiding thermotolerance in therapy, the heating must be generally well controlled in both temperature and exposure time. It seems reasonable to devise therapies of applying temperatures $T \geq 43\,^\circ\mathrm{C}$ for extended periods of time, e. g. $t_{\mathrm{HT}} > \frac{1}{2}$ hour [10, 72, 73]. However, the individual success of hyperthermia treatment depends on the superposition of challenges, such as (tumor) blood perfusion, targeting efficiency and accessibility of the tumor. To this end, personalized treatment for a given patient is necessary for successful MFH treatment, as proposed by the Berlin company *MagForce AG* [74–76]. In fact, based on these treatments, MFH has reached successful clinical trial stages I+II one decade ago [64, 65, 77, 78].

Most promise for MFH application lies with its enhancement of the efficacy of existing standard treatments. It has been shown that hyperthermia improves the efficacy of irradiation therapy [79–81]. Specifically, one third less radiation dose is needed to kill the same amount of cells, if they are heated to $T = 43\,^\circ\mathrm{C}$ either before or after irradiation [82]. Moreover, the efficacy of certain chemotherapeutic drugs increases significantly when administered together with local heating of the tumor tissue [83, 84]. New models even envision the combination of magnetic drug targeting (MDT) with MFH to form an entirely new, local cancer treatment technique [85, 86]. Here, MNP of thermosensitve coatings are loaded with chemotherapeutic drugs and injected into the body, where they are magnetically guided to and accumulated at the tumor site [87, 88]. There, the MNP are heated in an external AMF to trigger a local drug-release. Such a triggering has been demonstrated in vitro by the controlled release of fluorecent markers [89–91] and the anticancer drug doxorubicin [92] upon heating.

Interestingly, the potentially ground-breaking advantage of local heating restricted to tumor tissue in magnetically targeted MFH also includes its greatest challenge to enter clinical translation: According to Wilhelm et al., who analyzed 117 independent targeting studies, only $< 1\,\%$ of the administered MNP acutally reach the desired tumor [93]. Furthermore, Southern et al. recently cast doubt on whether MFH can actually be effective at low MNP concentrations in such a targeting scenario [94]. However, assuming an MNP concentration as chosen in the aforementioned clinical trials of $1\,\mathrm{M(Fe)}$[7] [64, 81], a targeting efficiency of $1\,\%$ results in $10\,\mathrm{mM(Fe)}$ of MNP at the tumor site. In Section 2.5.4 the targeting efficacy of MDT will be discussed in more detail for the example of a treatment approach of the pancreatic ductal adenocarcinoma (PDAC).

2.5.2. Pathways into Cells

Cells are the basic structural and functional unit of any living entity and the smallest units of life in general. Cells are enveloped by a membrane that separates the intracellular and extracellular

---

[7]This thesis differentiates between the MNP iron mass concentration, c [mg(Fe)/mL], and the MNP iron molar concentration, c_{M} [M $\,\hat{=}\,$ mol/L]. Typically the iron mass concentration, c, is given. Using the molar mass of iron, $m_{\mathrm{mol,Fe}} = 55.85\,\mathrm{g/mol}$, the two concentrations can be converted via c[mg(Fe)/mL]$= \frac{1}{55.85} \cdot c_{\mathrm{M}}$[M].

space [95]. The intracellular space is divided in the *nucleus*, containing mostly deoxyribonucleic acid (DNA) necessary for cell proliferation, and the *cytoplasma*, comprised of cellular organelles and metabolic end-products as well as foreign substances [96]. The cellular (plasma-)membrane consists mostly of a double layer of amphiphilic phospoholipids (so-called *phospholipid bilayer*), which is selectively permeable and regulates the exchange of substances between intra- and extracellular space, enables chemo-electrical communication to neighboring cells and provides mechanical adhesive forces to fix the cell in its surrounding [97].

Cells interact with their surrounding by exchanging substances (e. g. particles) via the processes of *endocytosis* (uptake inside the intracellular space) and *exocytosis* (secretion to the extracellular space) [98]. These pathways will be discussed in the following with special focus on the transport of nanoparticles. Generally, particles can enter cells by different endocytic pathways, depending on their size and surface ligands interacting with the cellular membrane. Large particles ($\sim 1\,\mu m$) are internalized via actin-driven phagocytosis, where the plasma membrane forms cup-shaped invaginations, which engulf the particle. Although quick and effective, phagocytosis is primarily used for the uptake of dead cells and debris, usually reserved to professional phagocytic cells (e. g. macrophages, dendritic cells and neurophils) [99]. For smaller particles ($\sim 100\,nm$), receptor-mediated, and more specifically clathrin- and caveolin-mediated, endocytosis occurs, which is the most common pathway into cells for viruses and nanoparticles [100, 101]. In clathrin-mediated endocytosis, clathrin-ligand binding causes the formation of invaginations in the cellular plasma membrane, which wraps the particle. Similarly, in the caveolin-mediated endocytic pathway, caveolin assembly at the cytoplasmatic side of the membrane triggers the formation of "flask-like" invaginations of $60-80\,nm$ in diameter (so-called "caveolae"), induced again by receptor-ligand binding [102]. Clathrin assembly at the membrane is also involved in the formation of vesicle necks necessary in the late wrapping stage in the pinch-off process for final internalization of particles [103]. Additional non-specific endocytic pathways are pinocytosis and macropinocytosis: In pinocytosis, biological fluid and small particles ($< 10\,nm$) are directly absorbed across the plasma membrane, whereas macropinocytosis is an actin-driven process of membrane engulfment of large amounts of extracellular fluid and substances, observed for the uptake of larger nanoparticles ($\sim 1\,\mu m$) [104]. Endocytosis pathways are summarized in Fig. 2.12. Note that the endocytosis pathways can be inhibited by passivating the cell, which can e. g. be achieved by cooling it down to temperatures of $T \approx (4-10)\,°C$ [98].

Upon internalization, the particles are wrapped in a membrane-enclosed intracellular vesicle and remain separated from the intracellular fluid. Inside the cell, these endocytic vesicles (called early endosomes) develop in late endosomes that increase in size by fusion with other endosomes [105], reaching final sizes of approximately $500\,nm$ in diameter [106]. Sometimes, endocytic vesicles are merged with their vesicle membranes still intakt, forming multivesicular bodies. Generally, late endosomes are of increasing acidity in preparation for finally fusing with lysosomes [107]. Lysosomes are responsible for the digestion of exogen (cell-foreign) material and therefore carry digestion enzymes (so-called hydrolase), working in an acidic environment with pH-value

approximately 4 [96]. Sometimes, substances escape endosomes into the intracellular fluid, from where they are secreted quickly. Cargo, which does not reach late endosomal stage or cannot be digested by the lysosomes is secreted via exocytosis. Exocytosis is basically the reversal of the endocytosis process: Intracellular vesicles transmigrate to the plasma membrane and are secreted either as membrane-wrapped vesicles or expelled freely into the extracellular space [99]. The entire pathways of nanoparticles into, across and out of cells are summarized in Fig. 2.12.
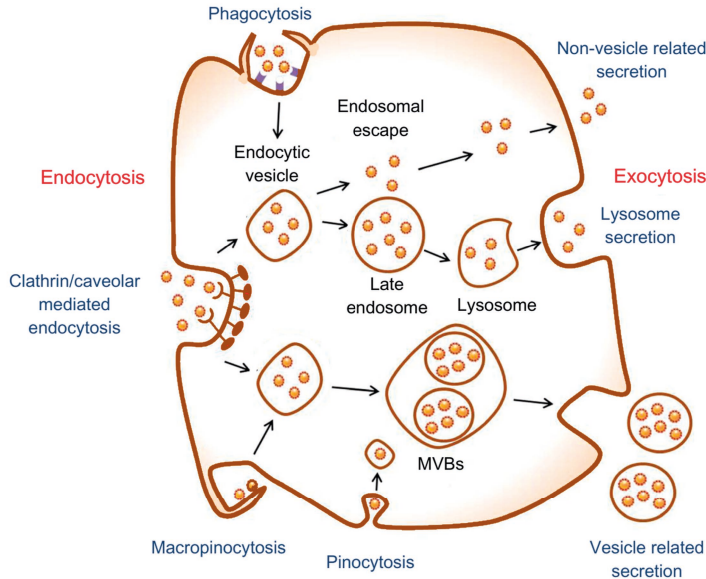
Fig. 2.12.: Pathways of nanoparticles into (endocytosis), through and out (exocytosis) of the cell. Endocytosis comprises of phagocytosis, clathrin- and caveolar-mediated endocytotis, macropinocytosis and pinocytosis. Inside the cell, endocytic vesicles develop either in late endosomes and lysosomes or multivesicular bodies (MVBs). In seldom cases, nanoparticles escape the endosome. Nanoparticles exit cells via lysosome secretion, vesicle related secretion or via non-vesicle related exocytosis. Adapted from [99].

2.5.3. Nanoheating Effects

As previously described in Section 2.5.1, hyperthermic cancer treatment usually aims at raising the temperature of tumor tissue to $(42 - 46)\,°C$, leading to tumor cell death, while at the same time sparing healthy tissue. This was a long standing goal for MFH since the first in vitro studies conducted by Jordan et al. [108] in 1996: In that study, human adenocarcinoma cells subjected to a bulk temperature of approx. $43\,°C$ reached via MFH showed a roughly equal inactivation of cell activtiy as the same cells heated to $43\,°C$ externally with a water bath. However, evidence is mounting that MFH is dealing intracellular cytotoxic damage even without a perceptible rise in bulk temperature [109–112]. The effect was coined nanoscale thermal phenomena or short *nanoheating* [113] and describes a dramatic temperature increase in the direct (nanoscale) vicinity of MNP upon interaction with AMF. Evaluating the intensity of thermosensitive fluorescent dye Dylight549 attached to the surface of MNP, Huang et al.

demonstrated that the surface temperature of the MNP was raised by approx. $5\,°\text{C}$ after $45\,\text{s}$ of AMF application, limiting particle heating clearly to the nanoscale vicinity of MNP [114]. Similarly, Polo-Corrales et al. attached fluorescent dye bound in thermosensitive polymer poly(N-isopropylacrylamide)(pNIPAM) to iron-oxide MNP to indirectly measure MNP surface temperatures by monitoring the increase in fluorescent intenstiy upon particle heating [115]: They applied an AMF and found an immediate increase in fluorescence. Using a water bath in control experiments, the same intensity as for AMF application was matched by reaching a global temperature increase of $\Delta T \approx 15\,°\text{C}$ (initial temperature $20\,°\text{C}$). Therefore, the authors further concluded that nanoheating on the order of $\Delta T \approx 15\,°\text{C}$ must occur on the surface of MNP under particle heating, which however does not affect the global temperature. Dong et al. used $\text{NaYF}_4\text{:Yb}^{3+}\text{-Er}^{3+}$ crystal nanothermometers inside silica nanoparticles ($d_C \approx 100\,\text{nm}$) loaded with MNP ($d_C \approx 20\,\text{nm}$) to optically measure the temperature dependent emission spectra, reporting an increase of up to $\Delta T \approx 30\,°\text{C}$ inside the silica particles [116]. Using temperature-sensitively bound Fluoresceineamine attached to the surface of iron oxide MNP Riedinger et al. were even able to approximate an immediate region of nanoheating of up to $100\,\text{nm}$ around the MNP, beyond which no substantial heating was measured [117]. Recent theoretical finite-
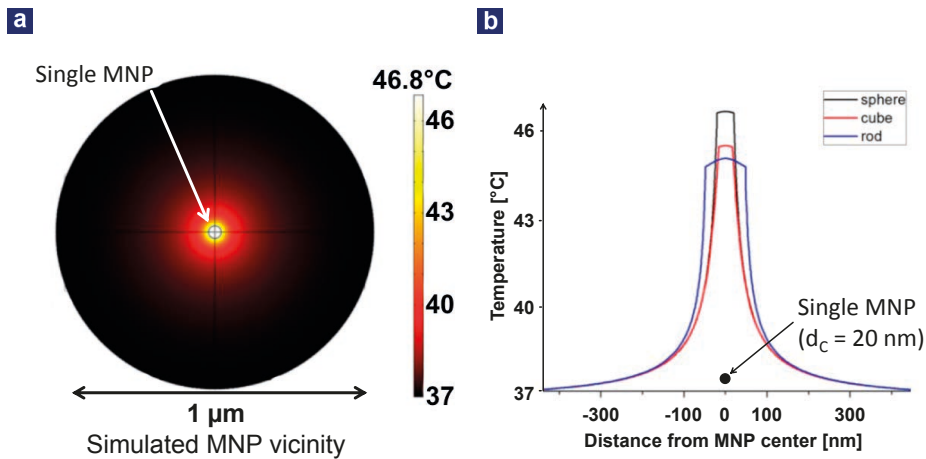
Fig. 2.13.: Simulated temperature distribution in the vicintiy of a single MNP with particle core diameter $d_C = 20\,\text{nm}$: (a) temperature distribution of the MNP located in the origin of a spherical compartment with diameter $d = 1\,\mu\text{m}$. (b) cross-sectional temperature distribution in the vicinity magnetic nanostructures of different shapes, all located at 0. Based on methods developed for a sperical MNP with $d_C = 20\,\text{nm}$, a nanocube and nanorod with the same nominal volume were simulated. Adapted from [118].

element simulation performed by Taloub et al. for a single iron oxide MNP with particle core size of $d_C = 20\,\text{nm}$ and assuming an SLP of $500\,\text{W/g(Fe)}$[8], confirms the above-mentioned experimental findings (Fig. 2.13) [118]: The MNP heats up by almost $10\,°\text{C}$ inside and at its surface (Fig. 2.13a), from where the temperature is exponentially decreasing, dropping to

---

[8]Actually, Taloub et al. assume a volumetric power density of $Q = 10^{16}\,\text{W/m}^3$ for their simulations. The authors base this assumption on [119], where SLP values of up to $500\,\text{W/g(Fe)}$ are reported, which also fits to the SLP values reported throughout this thesis.

approx. 15% of the maximum temperature at a distance of $100\,$nm from the MNP surface (Fig. 2.13b). Approximately $500\,$nm away from the MNP, there is no heating observed. Interestingly, nanostructures of different shapes but of the same nominal volume as the $20\,$nm-sized spherical MNP reached slightly lower maximum temperatures, but the temperature gradient in their outer vicinity ($100\,$nm and larger) was independent of the shape (cf. 2.13b).

All of the studies mentioned above clearly indicate the existence of nanoheating in the vicinity of MNP during particle heating, which is not perceptible in bulk temperature [113]. It is assumed, that such nanoheating effects have the ability to damage cells, provided that MNP are uptaken inside lysosomes or at least attached to the cell membrane [12, 112]. In fact, the expression of reactive oxygen species (ROS) can be detected within $30\,$min of AMF application [111], which is directly connected to lysosomal membrane permeabilization, leading to cell death [120].

In addition to nanoheating, a second mechanism of intracellular damage on the nanoscale can arise from (direct) mechanical rupture of the membrane due to the physical rotation of membrane-bound MNP with the applied magnetic field [121, 122][†]. It has been demonstrated that this mechanism leads to apoptosis of INS-1 cells in low frequency AMF $f = (5...20)\,$kHz [123][†]. Further, U87 brain tumor cells were reliably killed by membrane rupture due to slow rotation of membrane-bound $2\,\mu$m CoFeB/Pt microparticles [124][†].

In this way, intracellular nanoheating and mechanical rupture together could support the efficacy of MFH treatment especially for lower MNP concentrations at the tumor site[†], for which therapeutic bulk temperatures of $T \geq 43\,$°C cannot be reached.

2.5.4. Targeting Pancreatic Tumors

Cancer is one of the most challenging deseases to treat worldwide and approximately 25% of the total deaths in Germany were caused by cancer in 2015 [4]. Among the most aggressive types, the pancreatic ductal adenocarcinoma (PDAC)[†] has a 5-year-survival-rate of only less than 5% [125]. Moreover, PDAC is predicted to rank second in the total number of deaths caused by carcinoma in 2020 in the United States of America [126][†]. At present, surgical removal (resection) is the only curative therapy among established treatment routines, as PDAC has proven to be highly resistant to chemo- and radiotherapy [127, 128][†]. Unfortunately, resection is only possible in approximately 20% of the cases, as by the time the PDAC is diagnosed, the tumor has often metastasized already [129][†]. Of these 20% resectable tumors, many are encasing the superior mesenteric artery by more than $180°$, making resection very risky [130, 131][†]. Thus, there is desperate need for alternative therapies that are either stand-alone techniques or assist in partial regression of at least such 20% the tumor to make it accessible to resection eventually[†].

Current treatment strategies are either focused on combining chemo- and radiotherpy (so-called neoadjuvant therapy) — such as the CONKO-007 study [132] — or are exploring entirely new and innovative therapies. Among those innovative cancer therapies, MFH becomes increasingly

attractive due to the local and minimally-invasive delivery of heat with therapeutic temperatures to tumors (Section 2.5): For advanced therapy, biocompatible MNP are either directly injected into the tumor or administrated intravenously and accumulated at the tumor site via external magnetic fields (magnetic targeting)[†].

In clinical trials mentioned before (cf. Section 2.5), effective intratumoral temperatures up to approx. $47\,°\text{C}$ were reached during treatment [64][†]. These elevated temperatures could be achieved mainly due to a relatively high local concentration of MNP of up to approx. $128\,\text{mg(Fe)/mL}$ after a direct MNP intratumoral injection[†]. Nevertheless, an intratumoral injection is an invasive procedure with high risks of developing metastasis[†]. These risks can be omitted when magnetic targeting of MNP is intravenously applied, however, at the cost of reaching comparatively low MNP concentrations of approx. $150\,\text{μg(Fe)/g(Tumor)}$ $(3\,\text{mM})$ [133] to $400\,\text{μg(Fe)/g(Tumor)}$ $(7\,\text{mM})$ [134][†]. Such low concentrations were achieved for a mouse tumor model using permanent magnets[†]. Endoluminal tumor that can be reached endoscopically, such as PDAC, offer additional potential for magnetic targeting, as these allow the minimally-invasive insertion and accurate positioning of miniaturized coils or permanent magnets for magnetic targeting [18]. Using an endoscopic targeting setting and individualized magnets, it was recently demonstrated that the targeting efficiency could be enhanced by a factor of 40 [135][†]. This study is part of the same therapy approach as the MFH investigations in this thesis. Consequently, the local MNP concentration at disposal for MFH treatment would be much higher than the one for simple magnets mentioned above and the effective temperatures for treatment might be reached more easily[†]. In this way, an individualized and less stressful cancer therapy for each patient may be possible[†]. In particular, PDAC tumors could achieve regression and, in this way, be accessible for secondary resection[†].

This work is embedded in a treatment approach for PDAC and therefore the in vitro studies of the present thesis are focused on pancreatic tumor cells, adding to the full treatment strategy of combining endoscopic MNP magnetic targeting and MFH application. Using low MNP concentrations of $(3-7)\,\text{mM(Fe)}$ that are achieved for MNP targeting in animal models (s. above), this thesis explicitly studies the uptake of MNP inside pancreatic tumor cells in Chapter 6 and examines further the effects of nanoheating upon intracellular MFH application in Chapter 8.

2.6. Hydrogels and Rubber Elasticity Theory

Hydrogels are three-dimensional crosslinked polymer networks that swell, but do not dissolve, in water. Hydrogels have many applications, especially in biomedical technology, as they posses tissue-equivalent mechanical properties, while being easy to synthesize reproducibly. Hydrogels mixed with MNP are used in this thesis as a biocompatible model system to study the effect of gradual immobilization of MNP on magnetic particle heating in situ in Section 7.2. In the following, a general description of hydrogels is given, followed by a brief introduction in the rubber elasticity theory, which is used to describe the mechanical properties of hydrogels

mathematically. The description of the specifications of agarose and poly(acrylamide) hydrogels, which are specifically used throughout this thesis, concludes this section.

General Description of Hydrogels

Hydrogels are nonfluid natural or synthetic three-dimensional polymer networks resulting from cross-linking of polymer strands. These networks maintain their structure when being subjected to water, but at the same time exhibit a remarkable ability to absorb a large fraction of water within their stucture (typically containing up to $> 90\,\%$ of water)[9] [137]. Consequently, they swell in water, combining solid-like properties (e.g. internal polymer network structure) and liquid-like properties (e.g. flexibility, thermal and electrical properties similar water), and are therefore denoted as *hydrogels*[10]. Hydrogels offer a versatile tool for many applications in biomedicine and medical technology due to their biocompatibility, tissue-equivalent characteristics and tunable mechanical properties [138,139]. Most importantly, hydrogels are used in tissue engineering and cell biology as 2D and 3D extracellular cell matrices (ECM), promoting tailored (stem) cell growth and differentiation [140, 141]. But hydrogels also have major applications in e.g. macromolecular biology as a biocompatible electrophoresis embedding [142], and generally as tissue-equivalent phantoms in (pre-)clincial assessment of thermal dosimetry, ultrasound and magnetic resonance imaging [139, 143, 144]. Essentially, hydrogels can be differentiated in natural polymers - such as gelatine, matrigel, polysaccharides and the protein-based fibrin and collagen - and synthetic polymers, containing poly(acrylamide) (PAAm), polyethylenglycol (PEG), poly(oxazolines) (POZ), poly(vinyl alcohol) (PVA), and biodegradable poly(lactic-co-glycolic acid) (PLGA) and oligo(ethylene glycol) fumarates (OPF) [141]. All of these different hydrogels have unique properties useful for the applications mentioned above. The range of applications can even be expanded, however, by incorporating magnetic nanostructures inside hydrogels, forming so-called *ferrohydrogels* (FHG). As magnetically manipulable hybrid structures, FHG attract much interest in fundamental materials analysis and for biomedical applications: For example, $CoFe_2O_4$ MNP incorporated in PAAm hydrogels have been proposed as magneto-mechanical probes to non-invasively analyze the mechanic properties of the respective hydrogel network [145]. Furthermore, remote controlled cell and drug delivery systems were designed, which exploit the deformation of FHG in magnetic field gradients [146]. When investigated specifically for MFH applications, FHG enable active control of therapeutic heating temperatures for MFH [147] and thermosensitive drug delivery [148].

Rubber Elasticity Theory

The general term *elasticity* describes the ability of a material body to change its shape under the action of an external force and return to its initial shape when the external force is removed. *Rubber elasticity* is a special form of elasticity, which is thermodynamically based on a reversible

---

[9]There are also special hydrogels, classified as *superabsorbent hydrogels*, which can contain up to $99.9\,\%$ water [136].

[10]In this thesis, water-swollen gels are used, therefore they are named *hydrogels*. In principle, any fluid could be used as an extender to swell the gel, however these gels are not the focus of this thesis and are thus neglected.

change in the entropy of the material rather than a change the internal energy [149]. The *rubber elasticity theory* (RET), describes the mechanical properties of ideal rubber-like materials by a combination of thermodynamics and polymer chain statistics. RET is derived under to following assumptions [150]:

(I) the (Helmholtz) free energy, $F = U - T \cdot \Sigma$, with the temperature, T, and entropy, Σ, is minimized in the resting state,

(II) the internal energy, U, does not change under deformation, i.e. $dU = 0$,

(III) the material is incompressible, i.e. the material volume does not change under deformation, and

(IV) the deformations of the material are microscopically and macroscopically the same (affine deformation assumption).

From combining assumption (I) and (II) it follows that for an isothermal process an increase in the free energy due to deformation of the material will result in an a decrease in the system entropy, $d\Sigma < 0$, according to [151]:

$$dF = -T \cdot d\Sigma. \tag{2.71}$$

Furthermore, RET holds for materials whose matrix consists of long (polymer) chains of identical building blocks, which must be highly flexible and joined by crosslinkers in a network structure [151]. These chains rotate about their joints randomly due to activation from thermal energy[11], so that the distance between their ends is governed purely by statistical considerations: Applying assumption (III) and (IV) within the so-called Gaussian network theory [152], the entropy of deformation of these chains is fully described by the number of chains per unit volume, ν_{el}, and the Boltzmann constant, k_B. For *pure* strain (i.e. strain that does not involve rotating the principal axes), with the extension ratios λ'_x, λ'_y, λ'_z — describing the deformation parallel to the principal axes x, y, z in comparison to the initial state — and assuming $\lambda'_x \lambda'_y \lambda'_z = 1$, the entropy of deformation reads [152]:

$$d\Sigma = -\frac{1}{2}\nu_{el}k_B \cdot ((\lambda'_x)^2 + (\lambda'_y)^2 + (\lambda'_z)^2 - 3). \tag{2.72}$$

For shear strain in the (x, y)-plane the extension ratios may be defined as $\lambda'_x = \lambda'$, $\lambda'_y = 1/\lambda'$, $\lambda'_z = 1$ and the corresponding shear strain is $\gamma_{el} = (\lambda' - 1/\lambda')$ [153]. Now eq. (2.72) simplifies to:

$$d\Sigma = -\frac{1}{2}\nu_{el}k_B \cdot \gamma_{el}^2. \tag{2.73}$$

Inserting eq. (2.73) in eq. (2.71) and applying the definition of shear stress, one obtains:

$$\sigma_{el} = \frac{dF}{d\gamma_{el}} = \nu_{el}k_B T \cdot \gamma_{el}. \tag{2.74}$$

---

[11]This implies that the molecular segments of the chains have sufficient thermal energy to rotate freely, independent of their neighbors, i.e. RET holds only for those polymers in which the intermolecular forces between chains are sufficiently weak to satisfy this condition [152].

It can be seen from comparing eq. (2.74) to the general definition of the shear modulus, $G := \frac{\sigma_{\text{el}}}{\gamma_{\text{el}}}$, that the shear modulus is equivalent to the following expression in RET:

$$G = \nu_{\text{el}} \cdot k_{\text{B}} \cdot T. \qquad (2.75)$$

Consequently, the elastic properties (i.e. the stress-strain relations) of an ideal rubber-like material can be described by only a single physical parameter, the shear modulus G. Furthermore, the stress-strain relations have the same form for all rubber-like materials (assuming constant temperature), only subjected to a scale factor (G), which is determined by the number of chains per unit volume, ν_{el} [152]. Note that ν_{el} is also referred to as the number of active polymer strands throughout this thesis.

Specifics of Agarose and Poly(acrylamide) Hydrogels

For this thesis, the natural polymer hydrogel agarose and the synthetic polymer hydrogel poly(acrylamide) (PAAm) are used for immobilization studies of MNP in Section 7.2. The polymer network forms differently in these two hydrogels, as will be shortly sketched in the following description:

Agarose

As a linear polysaccharide, agarose consists of $(1 \rightarrow 3)$-β-D-galactopyranose-$(1 \rightarrow 4)$-$3,6$-anhydro-α-L-galactopyranose and contains a few ionized sulfate groups [154]. In highly purified agarose powders the amount of sulfate groups is below $0.2\,\%$ to better control its elastic properties. The gelling mechanism is temperature dependent, forming intramolecular hydrogen-bonds upon cooling, which assemble as aggregates of double helices resulting from the entanglement of anhydro bridges [155]. The chemical formula of one such building blocks of agarose gels is depicted in Fig. 2.14a. Agarose hydrogels are prepared from powder dissolved in hot deionized water (DI-H_2O): Standard agarose fully dissolves at $T = (90 - 100)\,°C$ solidifying at $T = (35 - 39)\,°C$ [156], while low-melting (LM-) agarose only requires temperatures around $T = (60 - 70)\,°C$ for dissolving in DI-H_2O and solidifies at $T \approx 28\,°C$ [157]. By controling the mass fraction of agarose in solution, the elastic moduli, E, and the mean mesh size, d_{mesh}, can be easily tuned between $E \sim (0.1 - 1\,000)\,\text{kPa}$ [141] and $d_{\text{mesh}} \sim (10 - 1\,000)\,\text{nm}$ [158], respectively.

Poly(acrylamide)

Poly(acrylamide) (PAAm) hydrogels form when monomers from one polymer are chemically joined at junction points by crosslinking monomers of a second polymer (s. Fig. 2.14b for a typical building block of such a crosslinking junction). Typically, PAAm hydrogels are produced by radical polymerization of a solution containing acrylamide (AAm) monomers and bi-functional[12] N,N'-methylenebisacrylamide (BIS) crosslinkers. The gelling mechanism is initialized on-demand by adding ammonium persulfate (APS) and N,N,N',N'-tetramethylethylene-diamine (TEMED) to start the exothermal free radical polymerization [159]. The reaction can

---

[12]I.e. consisting of two functional groups; here monomers and crosslinkers.
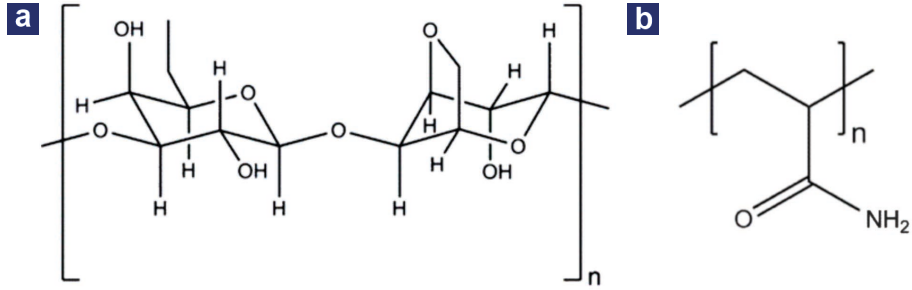
Fig. 2.14.: Chemical formula of one building block (multiplied block in brackets marked with n) of (a) agarose and (b) (poly)acrylamide hydrogels. Modified figures from [141].

be discribed by a chain polymerization mechanism [149]: After initiation, the radical reacts with one AAm monomer molecule, elongating the chain by one unit and moving the radical to the end of the chain. One bi-functional BIS crosslinker molecule can react with two separetly growing polymer chains, thereby forming crosslinked networks with "rubberlike" elasticity [160] (s. above). The elastic moduli, E, and the mean mesh size, d_{mesh}, of such a PAAm hydrogel can be tuned ranging between $E \sim (1 - 10\,000)\,\text{kPa}$ [141] and $d_{\text{mesh}} \sim (1 - 100)\,\text{nm}$ [158], respectively, by controlling the crosslinker fraction, i. e. the BIS mole fraction

$$\alpha = n_{\text{BIS}}/(n_{\text{AAm}} + n_{\text{BIS}}), \tag{2.76}$$

with the amounts of AAm, n_{AAm}, and BIS, n_{BIS}, respectively.

9. Conclusion and Future Directions

Throughout this thesis, magnetic nanoparticles (MNP) have been investigated as therapeutic heating agents for application in innovative cancer therapy via magnetic fluid hyperthermia (MFH). By studying various aspects of MFH — such as the optimization of particle heating considering medical limitation to the applied AMF, the uptake kinetics of MNP inside cells, the changes of particle heating under intracellular conditions and the efficacy of MFH in vitro — this thesis succeeds in answering four key research questions raised in the introduction (Chapter 1) and which are of paramount importance for the advancement of MFH application in tumor therapy:

1. *What MNP (i. e. which MNP properties) maximize the particle heating in MFH?*

2. *How do MNP interact with cells and how can the MNP uptake inside cell be quantified?*

3. *How does particle heating change upon MNP internalization inside cells?*

4. *How efficient is intracellular MFH applied to (tumor) cells; esp. at low MNP concentrations?*

These questions are answered by the main findings of this thesis, as presented in the following. Alongside, future directions on research opportunities resulting from these findings are pointed out.

Question 1 is investigated theoretically using Monte-Carlo (MC-)simulations of stochastic coupled Néel-Brownian magnetic relaxation of MNP to predict particle heating in Chapter 3. From these MC-simulations, the particle core size and effective anisotropy constant, as well as the external field parameters are identified as main contributors to particle heating. It can also be demonstrated that particle heating is indeed described most accurately within the framework of MC-simulations, when compared to established models for particle heating — the linear response theory and the Stoner-Wohlfarth based model theory (s. Section 3.3). Additionally, question 1 is investigated experimentally employing inductive particle heating measurements in Chapter 5, revealing that MNP with large particle core sizes, $d_C > 25$ nm, generate the most heat, expressed as a higher specific loss power (SLP). The trends of field-dependent particle heating predicted by MC-simulations agree well with experimental data, both showing a linear dependence of the SLP on the field-frequency (f) and a square dependency on the field-amplitude (H_0), as long as $H_0 < H_K/4$ holds (where H_K denotes the MNP anisotropy field). As a novelty, MC-simulations are matched to experimental data, showing best fitting for an anisotropy constant of $K_{eff} = 4$ kJ/m^3, lying substantially below magnetite bulk value ($K_{eff} = 11$ kJ/m^3). From these experimentally validated MC-simulations, predictions of SLP are derived in dependence of particle core size and AMF parameters limited to medically-tolerable field strengths (i. e. AMF parameters are low enough to not heat up healthy tissue). Results confirm the experimentally determined highest particle heating for large MNP with $d_C > 25$ nm at frequen-

cies of $f \approx 100\,\text{kHz}$, with the respective field amplitude adjusted to keep within the medically tolerated range. The results suggest an improvement in particle heating by a factor of approx. 12 compared to MNP systems currently used in clinical application of MFH, which is valuable information for the future design of MNP optimized for maximum heat generation and resulted in a publication [251]. In summary, particle heating is maximized for low (lower than bulk) anisotropy MNP with core sizes of $d_C > 25\,\text{nm}$, even under medically-tolerable limitations to the applied field, which precisely answers question 1.

Chapter 6 addresses question 2 by studying how MNP interact with pancreatic tumor cells and healthy control cells in vitro. From morphological analysis via transmission electron microscopy it is observed that MNP first group into agglomerates at the cellular plasma membrane within minutes of incubation with cells and second internalize as agglomerates inside cellular endosomes via endocytosis within tens of minutes (s. Sections 6.2.2 and 6.2.3). Furthermore, MNP are tightly clustered and immobilized inside these cellular endosomes, which merge over time into lysosomes with final average sizes after $24\,\text{h}$ in the range of $d_{\text{lys}} \approx (400 - 650)\,\text{nm}$, depending on the cell line. Additionally, some MNP agglomerates are also found attached to the outer cell membrane after $24\,\text{h}$, presumably due to exocytosis. Assuming a three-step process of (1) MNP agglomeration at the outer cell membrane, (2) endocytosis (internalization) of these MNP agglomerates inside the cell and (3) exocytosis (excretion) of MNP agglomerates, the MNP uptake kinetics can be modeled mathematically (s. Sections 6.3.4 and 6.3.5). For modeling, the MNP uptake kinetics is experimentally quantified with magnetic particle spectroscopy (MPS) over an incubation time of up to $24\,\text{h}$. The MNP uptake saturates after $6\,\text{h}$ of incubation in pancreatic tumor cells and after $8\,\text{h}$ of incubation in healthy control cells. This is valuable information for the future planning of MNP targeting duration before applying MFH for localized tumor therapy. In this way, question 2 can be precisely answered using the MNP uptake kinetics model, allowing to predict the MNP uptake inside cells for an arbitrary incubation time.

Chapters 7 and 8 address the change in particle heating upon intracellular agglomeration and immobilization of MNP (question 3). Generally, the SLP decreases by nearly two thirds for MNP inside cells compared to freely dispersed MNP (s. Section 8.2.4). This is in agreement with a decrease in the MPS spectral magnitude of intracellular MNP, attributed to the inhibition of Brownian relaxation upon MNP immobilization inside cells (s. Section 6.3.6), and an increase in the magnetic interparticle interactions for intracellular MNP, leading to demagnetization effects due to MNP agglomeration (s. Section 6.4). This thesis achieves a better understanding of the isolated contributions of either immobilization or agglomeration of MNP to particle heating by unambigously differentiating between both effects: MNP gradually immobilized in agarose and polyacrylamide hydrogels show a decrease in SLP of up to one third, which can be attributed to the inhibition of Brownian relaxation while excluding MNP agglomeration effects (s. Sections 7.1 and 7.2). These results demonstrate the gradual decrease in SLP upon gradual MNP immobilization on the basis of well-characterized hydrogels for the first time [264]. In contrast, MNP agglomerated in liposome shells and MNP agglomerates — formed after damaging their lauric acid shell by adding NaCl — show a significant increase in SLP by up to one forth, as long

as the MNP agglomerates are freely dispersed and rotatable [328]. If the MNP agglomerates are additionally immobilized, the SLP decreases by almost one third compared to monodisperse MNP in water [329]. In summary, and to answer question 3, the results reveal a decrease of nearly two thirds in particle heating for intracellular MNP due to a combination of inhibited Brownian relaxation upon MNP immobilization and demagnetization effects arising from the simultaneous MNP agglomeration inside cells.

In Chapter 8, MFH efficacy is evaluated in vitro on pancratic tumor cells MiaPaCa-2 and healthy L929 cells for low MNP concentrations of $c = (0.15...0.3)\,\mathrm{mg(Fe)/mL}$, specifically addressing question 4. Cytotoxic temperatures ($T \geq 43\,°\mathrm{C}$) can be reached even for low MNP concentrations achievable in animal models via magnetic targeting, resulting in significant cell damage. Moreover, significant cell damage is also observed without a perceptible temperature rise, indicating that additional nanoheating effects are present. This assumption is enforced by a higher MFH efficacy, when compared to conventional hyperthermia with the same bulk temperatures but without MNP. Most importantly, the MFH treatment efficacy can be evaluated by a single parameter — the total thermal energy deposited per cell (TEC) — which comprises the amount of intracellular MNP per cell, the SLP generated by the MNP and the duration of MFH treatment. Healthy L929 cells require a $50\,\%$ higher TEC to cause significant cell damage compared to pancreatic tumor cells MiaPaCa-2, which leaves a safety margin to only damage tumor cells in in vivo application of MFH [50]. Consequently, question 4 can be answered by evaluating the TEC, confirming that MFH is efficiently even at low MNP concentrations, destroying pancreatic MiaPaCa-2 tumor cells above a certain critical TEC, which is still harmless for healthy L929 cells.

Using TEC as the optimization parameter to evaluate the efficacy of MFH opens the discussion on future research opportunities to advance MFH application for tumor therapy: Further studies should include extensive in vitro analysis of MFH efficacy for many different cell lines (tumor cells and healthy references) in order to assess the individual critical TEC above which significant cell damage is expected for each cell line. Alongside, the MNP uptake kinetics for each cell line could be determined and modeled as presented in Chapter 6 to assess the amount of intracellular MNP per cell. As this work is embedded in a treatment approach for pancreatic tumors using endoscopic magnetic targeting of MNP (s. Section 2.5.4), the following specific suggestions for the application of MFH in this treatment approach can be made: Magnetic targeting of MNP should be performed for approx. $6\,\mathrm{h}$ to saturate MNP uptake inside cells prior to applying an AMF for $(60-90)$ min to induce sufficient cell death via MFH. As a future research opportunity, TEC could be used as a control parameter to plan in vivo application of MFH, as it can be tuned by (1) the (intracellular) particle heating, (2) the MNP uptake inside cells and (3) the duration of MFH treatment. TEC can generally be increased by using MNP optimized for particle heating in AMF of medically-tolerated strength (e.g. using low anisotropy MNP with large particle cores, $d_C \leq 25\,\mathrm{nm}$ as suggested by MC-simulations (s. Section 5.3)). Then, the MNP uptake (controlled via the incubation time prior to applying the MFH) and duration of

MFH treatment could be adjusted to match the predetermined critical TEC values necessary to induce tumor-specific cell damage while leaving healthy cells unharmed.

A different research opportunity arises from investigating the suitability of MNP as tracers for the simultaneous application of magnetic particle imaging (MPI) and MFH, as it is striking that MNP with particle core sizes of $d_\mathsf{C} = (25 - 28)\,\mathrm{nm}$ perform best for MPI and MFH alike (s. Chapter 5). From this, a theranostic platform could be envisioned, combining the advantages of imaging and heating in one MNP system and allowing to map the amount and distribution of MNP in real time using MPI, while applying MFH for tumor therapy.

B. Bibliography

[1] Ferlay J, Soerjomataram I, Ervik M, Dikshit R, Eser S, Mathers C, et al. Cancer Incidence and mortality worldwide: GLOBOCAN 2012 v1.1. IARC CancerBase. 2014;11.

[2] Organization WH, et al.. World Health Report 2018: Monitoring health for the SDGs. WHO; 2018. Available from: `http://apps.who.int/iris/bitstream/handle/10665/272596/9789241565585-eng.pdf?ua=1`.

[3] Stewart BW, Wild C. World Cancer Report 2014. World Health Organization and International Agency for Research on Cancer. 2014;p. 630.

[4] Statistisches-Bundesamt-Deutschland. Todesursachen in Deutschland. Fachserie. 2017;12(4). Available from: `https://www.destatis.de/DE/Publikationen/Thematisch/Gesundheit/Todesursachen/Todesursachen2120400157004.pdf?__blob=publicationFile`.

[5] Vaupel P, Kallinowski F, Okunieff P. Blood flow, oxygen and nutrient supply, and metabolic microenvironment of human tumors: a review. Cancer research. 1989;49(23):6449–6465.

[6] EU-Commission. Commission Recommendation of 18 October 2011 on the definition of nanomaterial (2011/696/EU). Official Journal of the European Communities: Legis. 2011;.

[7] Himpsel F, Ortega J, Mankey G, Willis R. Magnetic nanostructures. Advances in physics. 1998;47(4):511–597.

[8] Huang HW, Liauh CT, et al. Therapeutical applications of heat in cancer therapy. Journal of Medical and Biological Engineering. 2011;32(1):1–11.

[9] Mahmoudi K, Bouras A, Bozec D, Ivkov R, Hadjipanayis C. Magnetic hyperthermia therapy for the treatment of glioblastoma: a review of the therapy's history, efficacy and application in humans. International Journal of Hyperthermia. 2018;p. 1–13.

[10] Yarmolenko PS, Moon EJ, Landon C, Manzoor A, Hochman DW, Viglianti BL, et al. Thresholds for thermal damage to normal tissues: an update. International Journal of Hyperthermia. 2011;27(4):320–343.

[11] Wilhelm C, Gazeau F. Universal cell labelling with anionic magnetic nanoparticles. Biomaterials. 2008;29(22):3161–3174.

[12] Blanco-Andujar C, Teran F, Ortega D. Current Outlook and Perspectives on Nanoparticle-Mediated Magnetic Hyperthermia. In: Iron Oxide Nanoparticles for Biomedical Applications. Elsevier; 2018. p. 197–245.

[13] Aharoni A. Introduction to the theory of ferromagnetism. 1st ed. International series of monographs on physics. Oxford; New York: Oxford University Press; 1996.

[14] Krishnan KM. Fundamentals and applications of magnetic materials. 1st ed. Great Clarendon Street, Oxford, OX2, 6DP, UK: Oxford University Press; 2016.

[15] Rosensweig RE. Ferrohydrodynamics. Mineola, N.Y.: Dover Publications; 1997. Originally published: Cambridge ; New York : Cambridge University Press, 1985.

[16] Weiss P. Hypothesis of the molecular field and ferromagnetism. Bulletin de la Societe Francaise de Physique. 1907;(1):95–124.

[17] Barkhausen H. Zwei mit Hilfe der neuen Verstärker entdeckte Erscheinungen. Physik Zeitung. 1919;(20):401.

[18] Slabu I. Synthesis, characterization and application of superparamagnetic iron oxide nanoparticles in medical diagnostics and therapy: MR-visible implants for hernia repair and novel drug targeting models. Shaker Verlag; 2015.

[19] Farle M. Ferromagnetic resonance of ultrathin metallic layers. Reports on Progress in Physics. 1998;61(7):755.

[20] Bickford LR, Brownlow JM, Penoyer RF. Magnetocrystalline anisotropy in cobalt-substituted magnetite single crystals. IEEE Proceedings Part B: Electrical Engineering. 1957;104(5):238–244.

[21] Salazar-Alvarez G, Qin J, Sepelak V, Bergmann I, Vasilakaki M, Trohidou K, et al. Cubic versus spherical magnetic nanoparticles: the role of surface anisotropy. Journal of the American Chemical Society. 2008;130(40):13234–13239.

[22] Bødker F, Mørup S, Linderoth S. Surface effects in metallic iron nanoparticles. Physical Review Letters. 1994;72(2):282.

[23] Krishnan KM. Biomedical nanomagnetics: a spin through possibilities in imaging, diagnostics, and therapy. IEEE transactions on magnetics. 2010;46(7):2523–2558.

[24] Reeves DB. Nonequilibrium dynamics of magnetic nanoparticles in biomedical applications. PhD thesis Dartmouth College. 2015;.

[25] Mamiya H, Jeyadevan B. Hyperthermic effects of dissipative structures of magnetic nanoparticles in large alternating magnetic fields. Scientific reports. 2011;1:157.

[26] Gilbert TL. A phenomenological theory of damping in ferromagnetic materials. IEEE Transactions on Magnetics. 2004;40(6):3443–3449.

[27] Landi GT. Role of dipolar interaction in magnetic hyperthermia. Physical Review B. 2014;89(1):014403.

[28] Usov N, Liubimov BY. Dynamics of magnetic nanoparticle in a viscous liquid: Application to magnetic nanoparticle hyperthermia. Journal of Applied Physics. 2012;112(2):023901.

[29] Reeves DB, Weaver JB. Combined Néel and Brown rotational Langevin dynamics in magnetic particle imaging, sensing, and therapy. Applied physics letters. 2015;107(22):223106.

[30] Weizenecker J, Gleich B, Rahmer J, Dahnke H, Borgert J. Three-dimensional real-time in vivo magnetic particle imaging. Physics in Medicine & Biology. 2009;54(5):L1.

[31] Panagiotopoulos N, Duschka RL, Ahlborg M, Bringout G, Debbeler C, Graeser M, et al. Magnetic particle imaging: current developments and future directions. International journal of nanomedicine. 2015;10:3097.

[32] Knopp T, Buzug TM. Magnetic particle imaging: an introduction to imaging principles and scanner instrumentation. Springer Science & Business Media; 2012.

[33] Saritas EU, Goodwill PW, Croft LR, Konkle JJ, Lu K, Zheng B, et al. Magnetic particle imaging (MPI) for NMR and MRI researchers. Journal of Magnetic Resonance. 2013;229:116–126.

[34] Ferguson RM. Tracer design for magnetic particle imaging: modeling, synthesis, and experimental optimization of biocompatible iron oxide nanoparticles. University of Washington; 2011.

[35] Rahmer J, Weizenecker J, Gleich B, Borgert J. Signal encoding in magnetic particle imaging: properties of the system function. BMC medical imaging. 2009;9(1):4.

[36] Weizenecker J, Borgert J, Gleich B. A simulation study on the resolution and sensitivity of magnetic particle imaging. Physics in Medicine & Biology. 2007;52(21):6363.

[37] Goodwill PW, Conolly SM. The X-space formulation of the magnetic particle imaging process: 1-D signal, resolution, bandwidth, SNR, SAR, and magnetostimulation. IEEE transactions on medical imaging. 2010;29(11):1851–1859.

[38] Goodwill PW, Conolly SM. Multidimensional x-space magnetic particle imaging. IEEE transactions on medical imaging. 2011;30(9):1581–1590.

[39] Ferguson RM, Khandhar AP, Krishnan KM. Tracer design for magnetic particle imaging. Journal of applied physics. 2012;111(7):07B318.

[40] Goodwill P, Tamrazian A, Croft L, Lu C, Johnson E, Pidaparthi R, et al. Ferro-hydrodynamic relaxometry for magnetic particle imaging. Applied Physics Letters. 2011;98(26):262502.

[41] Ferguson RM, Khandhar AP, Arami H, Hua L, Hovorka O, Krishnan KM. Tailoring the magnetic and pharmacokinetic properties of iron oxide magnetic particle imaging tracers. Biomedizinische Technik/Biomedical Engineering. 2013;58(6):493–507.

[42] Carrey J, Mehdaoui B, Respaud M. Simple models for dynamic hysteresis loop calcu-
lations of magnetic single-domain nanoparticles: Application to magnetic hyperthermia
optimization. Journal of Applied Physics. 2011;109(8).

[43] Hergt R, Dutz S. Magnetic particle hyperthermia—biophysical limitations of a visionary
tumour therapy. Journal of Magnetism and Magnetic Materials. 2007;311(1):187–192.

[44] Ibach H, Lüth H. Festkörperphysik: Einführung in die Grundlagen. Springer-Verlag; 2009.

[45] Garcia-Otero J, Garcia-Bastida AJ, Rivas J. Influence of temperature on the coercive field
of non-interacting fine magnetic particles. Journal of Magnetism and Magnetic Materials.
1998;189(3):377–383.

[46] Usov N, Grebenshchikov YB. Hysteresis loops of an assembly of superparamagnetic
nanoparticles with uniaxial anisotropy. Journal of Applied Physics. 2009;106(2):023917.

[47] Mehdaoui B, Meffre A, Carrey J, Lachaize S, Lacroix LM, Gougeon M, et al. Optimal
size of nanoparticles for magnetic hyperthermia: a combined theoretical and experimental
study. Advanced Functional Materials. 2011;21(23):4573–4581.

[48] Rosensweig RE. Heating magnetic fluid with alternating magnetic field. Journal of mag-
netism and magnetic materials. 2002;252:370–374.

[49] Debye PJW. Polar molecules. Chemical Catalog Company, Inc.; 1929.

[50] Engelmann UM, Roeth AA, Eberbeck D, Buhl EM, Neumann UP, Schmitz-Rode T, et al.
Combining bulk temperature and nanoheating enables advanced magnetic fluid hyper-
thermia efficacy on pancreatic tumor cells. Scientific Reports. 2018;8(1):13210.

[51] Christophi C, Winkworth A, Muralihdaran V, Evans P. The treatment of malignancy by
hyperthermia. Surgical Oncology-Oxford. 1998;7(1-2):83–90.

[52] Jeyadevan B. Present status and prospects of magnetite nanoparticles-based hyperther-
mia. Journal of the Ceramic Society of Japan. 2010;118(1378):391–401.

[53] Brace C. Thermal tumor ablation in clinical use. IEEE pulse. 2011;2(5):28–38.

[54] D'Andrea J, Gandhi O, Lords J, Durney C, Johnson CC, Astle L. Physiological and
behavioral effects of chronic exposure to 2450-MHz microwaves. Journal of microwave
power. 1979;14(4):351–362.

[55] Ritz J, Germer C, Roogan A, Isbert C, Pelz J, Buhr H. Hyperthermic effects of laserinduced
thermotherapy-comparison of arterial microembolisation and hepatic blood flow occlusion.
In: Gastroenterology. vol. 116. Elsevier; 1999. p. A491–A491.

[56] Brezovich IA, Young JH. Hyperthermia with implanted electrodes. Medical physics.
1981;8(1):79–84.

[57] Robins H, d'Oleire F, Grosen E, Spriggs D. Rationale and clinical status of 41.8 degrees C systemic hyperthermia tumor necrosis factor, and melphalan for neoplastic disease. Anticancer research. 1997;17(4B):2891–2894.

[58] Jordan A, Scholz R, Wust P, Fähling H, Felix R. Magnetic fluid hyperthermia (MFH): Cancer treatment with AC magnetic field induced excitation of biocompatible superparamagnetic nanoparticles. Journal of Magnetism and Magnetic materials. 1999;201(1-3):413–419.

[59] Laurent S, Dutz S, Häfeli UO, Mahmoudi M. Magnetic fluid hyperthermia: focus on superparamagnetic iron oxide nanoparticles. Advances in colloid and interface science. 2011;166(1-2):8–23.

[60] Pankhurst Q, Thanh N, Jones S, Dobson J. Progress in applications of magnetic nanoparticles in biomedicine. Journal of Physics D: Applied Physics. 2009;42(22):224001.

[61] Wust P, Gneveckow U, Wust P, Gneveckow U, Johannsen M, Böhmer D, et al. Magnetic nanoparticles for interstitial thermotherapy–feasibility, tolerance and achieved temperatures. International Journal of Hyperthermia. 2006;22(8):673–685.

[62] Jordan A, Wust P, Fählin H, John W, Hinz A, Felix R. Inductive heating of ferrimagnetic particles and magnetic fluids: physical evaluation of their potential for hyperthermia. International Journal of Hyperthermia. 1993;9(1):51–68.

[63] Atkinson WJ, Brezovich IA, Chakraborty DP. Usable frequencies in hyperthermia with thermal seeds. IEEE Transactions on Biomedical Engineering. 1984;(1):70–75.

[64] Maier-Hauff K, Rothe R, Scholz R, Gneveckow U, Wust P, Thiesen B, et al. Intracranial thermotherapy using magnetic nanoparticles combined with external beam radiotherapy: results of a feasibility study on patients with glioblastoma multiforme. Journal of neuro-oncology. 2007;81(1):53–60.

[65] Johannsen M, Gneveckow U, Thiesen B, Taymoorian K, Cho CH, Waldöfner N, et al. Thermotherapy of prostate cancer using magnetic nanoparticles: feasibility, imaging, and three-dimensional temperature distribution. European urology. 2007;52(6):1653–1662.

[66] Ahlbom A, Bergqvist U, Bernhardt J, Cesarini J, Grandolfo M, Hietanen M, et al. Guidelines for limiting exposure to time-varying electric, magnetic, and electromagnetic fields (up to 300 GHz). Health physics. 1998;74(4):494–521.

[67] on Non-Ionizing Radiation Protection IC, et al. Guidelines for limiting exposure to time-varying electric and magnetic fields (1 Hz to 100 kHz). Health physics. 2010;99(6):818–836.

[68] Henle KJ. Sensitization to hyperthermia below 43 °C induced in Chinese hamster ovary cells by step-down heating. JNCI: Journal of the National Cancer Institute.

1980;64(6):1479–1483.

[69] Li G, Mivechi NF, Weitzel G. Heat shock proteins, thermotolerance, and their relevance to clinical hyperthermia. International journal of hyperthermia. 1995;11(4):459–488.

[70] Li GC, Hahn GM. A proposed operational model of thermotolerance based on effects of nutrients and the initial treatment temperature. Cancer Research. 1980;40(12):4501–4508.

[71] Hahn GM. Comparison of the Malignant Potential of $10T1/2$ Cells and Transformants with Their Survival Responses to Hyperthermia and to Amphotericin B. Cancer research. 1980;40(10):3763–3767.

[72] Van Rhoon GC, Samaras T, Yarmolenko PS, Dewhirst MW, Neufeld E, Kuster N. CEM43 C thermal dose thresholds: a potential guide for magnetic resonance radiofrequency exposure levels? European radiology. 2013;23(8):2215–2227.

[73] Bettaieb A, Wrzal PK, Averill-Bates DA. Hyperthermia: Cancer treatment and beyond. In: Cancer Treatment-Conventional and Innovative Approaches. InTech; 2013. .

[74] Gneveckow U, Jordan A, Scholz R, Brüß V, Waldöfner N, Ricke J, et al. Description and characterization of the novel hyperthermia-and thermoablation-system MFH® 300F for clinical magnetic fluid hyperthermia. Medical physics. 2004;31(6):1444–1451.

[75] Gellermann J, Wust P, Stalling D, Seebass M, Nadobny J, Beck R, et al. Clinical evaluation and verification of the hyperthermia treatment planning system hyperplan. International Journal of Radiation Oncology - Biology - Physics. 2000;47(4):1145–1156.

[76] Thiesen B, Jordan A. Clinical applications of magnetic nanoparticles for hyperthermia. International journal of hyperthermia. 2008;24(6):467–474.

[77] Johannsen M, Gneveckow U, Eckelt L, Feussner A, Waldöfner N, Scholz R, et al. Clinical hyperthermia of prostate cancer using magnetic nanoparticles: presentation of a new interstitial technique. International journal of hyperthermia. 2005;21(7):637–647.

[78] Tilly W, Wust P, Rau B, Harder C, Gellermann J, Schlag P, et al. Temperature data and specific absorption rates in pelvic tumours: predictive factors and correlations. International journal of hyperthermia. 2001;17(2):172–188.

[79] Attaluri A, Kandala SK, Wabler M, Zhou H, Cornejo C, Armour M, et al. Magnetic nanoparticle hyperthermia enhances radiation therapy: A study in mouse models of human prostate cancer. International Journal of Hyperthermia. 2015;31(4):359–374.

[80] Torres-Lugo M, Rinaldi C. Thermal potentiation of chemotherapy by magnetic nanoparticles. Nanomedicine. 2013;8(10):1689–1707.

[81] Maier-Hauff K, Ulrich F, Nestler D, Niehoff H, Wust P, Thiesen B, et al. Efficacy and

safety of intratumoral thermotherapy using magnetic iron-oxide nanoparticles combined with external beam radiotherapy on patients with recurrent glioblastoma multiforme. Journal of neuro-oncology. 2011;103(2):317–324.

[82] Hahn GM. Hyperthermia for the engineer: A short biological primer. IEEE Transactions on Biomedical engineering. 1984;(1):3–8.

[83] Miller R, Richards M, Baird C, Martin S, Hall E. Interaction of hyperthermia and chemotherapy agents; cell lethality and oncogenic potential. International journal of hyperthermia. 1994;10(1):89–99.

[84] Urano M. Invited review: for the clinical application of thermochemotherapy given at mild temperatures. International journal of hyperthermia. 1999;15(2):79–107.

[85] Corchero J, Villaverde A. Biomedical applications of distally controlled magnetic nanoparticles. Trends in Biotechnology. 2009;27(8):468–476.

[86] Cole AJ, Yang VC, David AE. Cancer theranostics: the rise of targeted magnetic nanoparticles. Trends in Biotechnology. 2011;29(7):323–332.

[87] J Wang YX, Xuan S, Port M, Idee JM. Recent advances in superparamagnetic iron oxide nanoparticles for cellular imaging and targeted therapy research. Current pharmaceutical design. 2013;19(37):6575–6593.

[88] Estelrich J, Escribano E, Queralt J, Busquets MA. Iron oxide nanoparticles for magnetically-guided and magnetically-responsive drug delivery. International journal of molecular sciences. 2015;16(4):8070–8101.

[89] Kalele S, Narain R, Krishnan KM. Probing temperature-sensitive behavior of pNIPAAm-coated iron oxide nanoparticles using frequency-dependent magnetic measurements. Journal of Magnetism and Magnetic Materials. 2009;321(10):1377–1380.

[90] Herrera AP, Rodriguez M, Torres-Lugo M, Rinaldi C. Multifunctional magnetite nanoparticles coated with fluorescent thermo-responsive polymeric shells. Journal of Materials Chemistry. 2008;18(8):855–858.

[91] Tai LA, Tsai PJ, Wang YC, Wang YJ, Lo LW, Yang CS. Thermosensitive liposomes entrapping iron oxide nanoparticles for controllable drug release. Nanotechnology. 2009;20(13):135101.

[92] Zhang J, Misra R. Magnetic drug-targeting carrier encapsulated with thermosensitive smart polymer: core–shell nanoparticle carrier and drug release response. Acta biomaterialia. 2007;3(6):838–850.

[93] Wilhelm S, Tavares AJ, Dai Q, Ohta S, Audet J, Dvorak HF, et al. Analysis of nanoparticle delivery to tumours. Nature Reviews Materials. 2016;1(5):16014.

[94] Southern P, Pankhurst QA. Commentary on the clinical and preclinical dosage limits of interstitially administered magnetic fluids for therapeutic hyperthermia based on current practice and efficacy models. International Journal of Hyperthermia. 2017;p. 1–16.

[95] Kugler P. Der menschliche Körper: Anatomie Physiologie Pathologie. Elsevier Health Sciences; 2017.

[96] Leonhardt H. Histologie, Zytologie und Mikroanatomie des Menschen. 7th ed. Taschen-lehrbuch der gesamten Anatomie. Oxford; New York: Georg Thieme Verlagt Stuttgart - New York; 1985.

[97] Klinke R, Pape HC, Kurtz A, Silbernagl S. Physiologie. Georg Thieme Verlag; 2009.

[98] Doherty GJ, McMahon HT. Mechanisms of endocytosis. Annual review of biochemistry. 2009;78:857–902.

[99] Oh N, Park JH. Endocytosis and exocytosis of nanoparticles in mammalian cells. International journal of nanomedicine. 2014;9(Suppl 1):51.

[100] Mercer J, Schelhaas M, Helenius A. Virus entry by endocytosis. Annual review of biochemistry. 2010;79:803–833.

[101] Iversen TG, Skotland T, Sandvig K. Endocytosis and intracellular transport of nanoparticles: present knowledge and need for future studies. Nano Today. 2011;6(2):176–185.

[102] Parton RG, Simons K. The multiple faces of caveolae. Nature reviews Molecular cell biology. 2007;8(3):185.

[103] Zhang S, Gao H, Bao G. Physical principles of nanoparticle cellular endocytosis. ACS nano. 2015;9(9):8655–8671.

[104] Swanson JA. Shaping cups into phagosomes and macropinosomes. Nature reviews Molecular cell biology. 2008;9(8):639.

[105] Rink J, Ghigo E, Kalaidzidis Y, Zerial M. Rab conversion as a mechanism of progression from early to late endosomes. Cell. 2005;122(5):735–749.

[106] Ganley IG, Carroll K, Bittova L, Pfeffer S. Rab9 GTPase regulates late endosome size and requires effector interaction for its stability. Molecular biology of the cell. 2004;15(12):5420–5430.

[107] Luzio JP, Rous BA, Bright NA, Pryor PR, Mullock BM, Piper RC. Lysosome-endosome fusion and lysosome biogenesis. J Cell Sci. 2000;113(9):1515–1524.

[108] Jordan A, Wust P, Scholz R, Tesche B, Fähling H, Mitrovics T, et al. Cellular uptake of magnetic fluid particles and their effects on human adenocarcinoma cells exposed to AC magnetic fields in vitro. International journal of hyperthermia. 1996;12(6):705–722.

[109] Creixell M, Bohorquez AC, Torres-Lugo M, Rinaldi C. EGFR-targeted magnetic nanoparticle heaters kill cancer cells without a perceptible temperature rise. ACS nano. 2011;5(9):7124–7129.

[110] Schaub NJ, Rende D, Yuan Y, Gilbert RJ, Borca-Tasciuc DA. Reduced astrocyte viability at physiological temperatures from magnetically activated iron oxide nanoparticles. Chemical research in toxicology. 2014;27(12):2023–2035.

[111] Connord V, Clerc P, Hallali N, El Hajj Diab D, Fourmy D, Gigoux V, et al. Real-time analysis of magnetic hyperthermia experiments on living cells under a confocal microscope. Small. 2015;11(20):2437–2445.

[112] Blanco-Andujar C, Ortega D, Southern P, Nesbitt SA, Thanh NTK, Pankhurst QA. Real-time tracking of delayed-onset cellular apoptosis induced by intracellular magnetic hyperthermia. Nanomedicine. 2016;11(2):121–136.

[113] Chiu-Lam A, Rinaldi C. Nanoscale thermal phenomena in the vicinity of magnetic nanoparticles in alternating magnetic fields. Advanced functional materials. 2016;26(22):3933–3941.

[114] Huang H, Delikanli S, Zeng H, Ferkey DM, Pralle A. Remote control of ion channels and neurons through magnetic-field heating of nanoparticles. Nature nanotechnology. 2010;5(8):602.

[115] Polo-Corrales L, Rinaldi C. Monitoring iron oxide nanoparticle surface temperature in an alternating magnetic field using thermoresponsive fluorescent polymers. Journal of Applied Physics. 2012;111(7):07B334.

[116] Dong J, Zink JI. Taking the temperature of the interiors of magnetically heated nanoparticles. ACS nano. 2014;8(5):5199–5207.

[117] Riedinger A, Guardia P, Curcio A, Garcia MA, Cingolani R, Manna L, et al. Sub-nanometer local temperature probing and remotely controlled drug release based on azo-functionalized iron oxide nanoparticles. Nano letters. 2013;13(6):2399–2406.

[118] Taloub S, Hobar F, Astefanoaei I, Dumitru I, Caltun OF. FEM Investigation of Coated Magnetic Nanoparticles for Hyperthermia. Nanoscience and Nanotechnology. 2016;6(1A):55–61.

[119] Pearce J, Giustini A, Stigliano R, Hoopes PJ. Magnetic heating of nanoparticles: The importance of particle clustering to achieve therapeutic temperatures. Journal of nanotechnology in engineering and medicine. 2013;4(1):011005.

[120] Domenech M, Marrero-Berrios I, Torres-Lugo M, Rinaldi C. Lysosomal membrane permeabilization by targeted magnetic nanoparticles in alternating magnetic fields. ACS nano. 2013;7(6):5091–5101.

[121] Tseng P, Judy JW, Di Carlo D. Magnetic nanoparticle–mediated massively parallel mechanical modulation of single-cell behavior. Nature methods. 2012;9(11):1113.

[122] Sadhukha T, Wiedmann TS, Panyam J. Enhancing therapeutic efficacy through designed aggregation of nanoparticles. Biomaterials. 2014;35(27):7860–7869.

[123] Zhang E, Kircher MF, Koch M, Eliasson L, Goldberg SN, Renstroem E. Dynamic magnetic fields remote-control apoptosis via nanoparticle rotation. ACS nano. 2014;8(4):3192–3201.

[124] Mansell R, Vemulkar T, Petit DC, Cheng Y, Murphy J, Lesniak MS, et al. Magnetic particles with perpendicular anisotropy for mechanical cancer cell destruction. Scientific reports. 2017;7(1):4257.

[125] Hezel AF, Kimmelman AC, Stanger BZ, Bardeesy N, DePinho RA. Genetics and biology of pancreatic ductal adenocarcinoma. Genes & development. 2006;20(10):1218–1249.

[126] Rahib L, Smith BD, Aizenberg R, Rosenzweig AB, Fleshman JM, Matrisian LM. Projecting cancer incidence and deaths to 2030: the unexpected burden of thyroid, liver, and pancreas cancers in the United States. Cancer research. 2014;74:2913–2921.

[127] Brus C, Saif MW. Second line therapy for advanced pancreatic adenocarcinoma: where are we and where are we going? JOP Journal of the Pancreas. 2010;11(4):321–323.

[128] Kimmelman AC, Hezel AF, Aguirre AJ, Zheng H, Paik Jh, Ying H, et al. Genomic alterations link Rho family of GTPases to the highly invasive phenotype of pancreas cancer. Proceedings of the National Academy of Sciences. 2008;105(49):19372–19377.

[129] Ettrich TJ, Perkhofer L, Seufferlein T. Therapie des Pankreaskarzinoms–und sie bewegt sich doch! DMW-Deutsche Medizinische Wochenschrift. 2015;140(07):508–511.

[130] Glanemann M, Shi B, Liang F, Sun XG, Bahra M, Jacob D, et al. Surgical strategies for treatment of malignant pancreatic tumors: extended, standard or local surgery? World journal of surgical oncology. 2008;6(1):123.

[131] Yekebas EF, Bogoevski D, Cataldegirmen G, Kunze C, Marx A, Vashist YK, et al. En bloc vascular resection for locally advanced pancreatic malignancies infiltrating major blood vessels: perioperative outcome and long-term survival in 136 patients. Annals of surgery. 2008;247(2):300–309.

[132] Pancreatic Carcinoma: Chemoradiation Compared With Chemotherapy Alone After Induction Chemotherapy (CONKO-007). University-of-Erlangen-Nürnberg-Medical-School. 2018-07-18;Available from: https://clinicaltrials.gov/ct2/show/NCT01827553.

[133] Li WM, Chiang CS, Huang WC, Su CW, Chiang MY, Chen JY, et al. Amifostine-conjugated pH-sensitive calcium phosphate-covered magnetic-amphiphilic

gelatin nanoparticles for controlled intracellular dual drug release for dual-targeting in HER-2-overexpressing breast cancer. Journal of Controlled Release. 2015;220:107–118.

[134] Hashemi-Moghaddam H, Kazemi-Bagsangani S, Jamili M, Zavareh S. Evaluation of magnetic nanoparticles coated by 5-fluorouracil imprinted polymer for controlled drug delivery in mouse breast cancer model. International journal of pharmaceutics. 2016;497(1-2):228–238.

[135] Roeth AA, Slabu I, Baumann M, Alizai PH, Schmeding M, Guentherodt G, et al. Establishment of a biophysical model to optimize endoscopic targeting of magnetic nanoparticles for cancer treatment. International journal of nanomedicine. 2017;12:5933.

[136] Zohuriaan-Mehr MJ, Kabiri K. Superabsorbent polymer materials: a review. Iranian polymer journal. 2008;17(6):451.

[137] Ahmed EM. Hydrogel: Preparation, characterization, and applications: A review. Journal of advanced research. 2015;6(2):105–121.

[138] Lamouche G, Kennedy BF, Kennedy KM, Bisaillon CE, Curatolo A, Campbell G, et al. Review of tissue simulating phantoms with controllable optical, mechanical and structural properties for use in optical coherence tomography. Biomedical optics express. 2012;3(6):1381–1398.

[139] Pogue BW, Patterson MS. Review of tissue simulating phantoms for optical spectroscopy, imaging and dosimetry. Journal of biomedical optics. 2006;11(4):041102.

[140] Marklein RA, Burdick JA. Controlling stem cell fate with material design. Advanced materials. 2010;22(2):175–189.

[141] Thiele J, Ma Y, Bruekers S, Ma S, Huck WT. 25th Anniversary article: designer hydrogels for cell cultures: a materials selection guide. Advanced materials. 2014;26(1):125–148.

[142] Chrambach A, Rodbard D. Polyacrylamide gel electrophoresis. Science. 1971;172(3982):440–451.

[143] Culjat MO, Goldenberg D, Tewari P, Singh RS. A review of tissue substitutes for ultrasound imaging. Ultrasound in Medicine and Biology. 2010;36(6):861–873.

[144] Menikou G, Yiannakou M, Yiallouras C, Ioannides C, Damianou C. MRI-compatible bone phantom for evaluating ultrasonic thermal exposures. Ultrasonics. 2016;71:12–19.

[145] Frickel N, Messing R, Schmidt AM. Magneto-mechanical coupling in $CoFe_2O_4$-linked PAAm ferrohydrogels. Journal of Materials Chemistry. 2011;21(23):8466–8474.

[146] Zhao X, Kim J, Cezar CA, Huebsch N, Lee K, Bouhadir K, et al. Active scaffolds for on-demand drug and cell delivery. Proceedings of the National Academy of Sciences. 2011;108(1):67–72.

[147] Lao L, Ramanujan R. Magnetic and hydrogel composite materials for hyperthermia applications. Journal of materials science: Materials in medicine. 2004;15(10):1061–1064.

[148] Zhang ZQ, Song SC. Thermosensitive/superparamagnetic iron oxide nanoparticle-loaded nanocapsule hydrogels for multiple cancer hyperthermia. Biomaterials. 2016;106:13–23.

[149] Mark JE, et al. Physical properties of polymers handbook. vol. 1076. Springer; 2007.

[150] Treloar L. Physics of Rubber Elasticity (Oxford classic texts in the physical sciences). Oxford University Press; 2005.

[151] Sperling LH. Polymeric multicomponent materials: an introduction. Wiley-Interscience; 1997.

[152] Treloar L. The elasticity and related properties of rubbers. Reports on progress in physics. 1973;36(7):755.

[153] Love A. A treatise on the mathematical theory of elasticity. 4th ed. Cambridge University Press; 1927.

[154] Arnott S, Fulmer A, Scott W, Dea I, Moorhouse R, Rees D. The agarose double helix and its function in agarose gel structure. Journal of molecular biology. 1974;90(2):269–284.

[155] Velasco D, Tumarkin E, Kumacheva E. Microfluidic encapsulation of cells in polymer microgels. Small. 2012;8(11):1633–1642.

[156] Agarose - SERVA Wide Range (molecular biology grade) - Specification Data Sheet. Serva Electrophoresis GmbH. 2016;Cat.No.: 11406.

[157] Agarose Low Melt - Roti®garose - Specification Data Sheet. Carl Roth GmbH + Co KG. 2017;Cat.No.: 6351.

[158] Righetti PG, Brost BC, Snyder RS. On the limiting pore size of hydrophilic gels for electrophoresis and isoelectric focussing. Journal of biochemical and biophysical methods. 1981;4(5-6):347–363.

[159] Tse JR, Engler AJ. Preparation of hydrogel substrates with tunable mechanical properties. Current protocols in cell biology. 2010;p. 10–16.

[160] Horkay F, McKenna GB. Polymer networks and gels. In: Physical properties of polymers handbook. Springer; 2007. p. 497–523.

[161] Tan R, Carrey J, Respaud M. Magnetic hyperthermia properties of nanoparticles inside lysosomes using kinetic Monte Carlo simulations: Influence of key parameters and dipolar interactions, and evidence for strong spatial variation of heating power. Physical Review B. 2014;90(21):214421.

[162] Ovejero JG, Cabrera D, Carrey J, Valdivielso T, Salas G, Teran FJ. Effects of inter-and intra-aggregate magnetic dipolar interactions on the magnetic heating efficiency of iron oxide nanoparticles. Physical Chemistry Chemical Physics. 2016;18(16):10954–10963.

[163] Ruta S, Chantrell R, Hovorka O. Unified model of hyperthermia via hysteresis heating in systems of interacting magnetic nanoparticles. Scientific reports. 2015;5:9090.

[164] Mamiya H, Jeyadevan B. Optimal design of nanomagnets for targeted hyperthermia. Journal of Magnetism and Magnetic Materials. 2011;323(10):1417–1422.

[165] Mamiya H, Jeyadevan B. Formation of Nonequilibrium Magnetic Nanoparticle Structures in a Large Alternating Magnetic Field and Their Influence on Magnetic Hyperthermia Treatment. IEEE Transactions on Magnetics. 2012;48(11):3258–3261.

[166] Van Kampen NG. Stochastic processes in physics and chemistry. vol. 1. Elsevier; 1992.

[167] Garcia-Alvarez D. A comparison of a few numerical schemes for the integration of stochastic differential equations in the Stratonovich interpretation. arXiv preprint arXiv:11024401. 2011;.

[168] Burrage K, Burrage P, Tian T. Numerical methods for strong solutions of stochastic differential equations: an overview. In: Proceedings of The Royal Society of London A: Mathematical, Physical and Engineering Sciences. vol. 460:2041. The Royal Society; 2004. p. 373–402.

[169] Platen E. An introduction to numerical methods for stochastic differential equations. Acta numerica. 1999;8:197–246.

[170] Guidoum AC, Boukhetala K. Itô and Stratonovich stochastic calculus with sSimDiffProc package version 2.9. pdfssemanticscholarorg. 2014;.

[171] Scholz W, Schrefl T, Fidler J. Micromagnetic simulation of thermally activated switching in fine particles. Journal of Magnetism and Magnetic Materials. 2001;233(3):296–304.

[172] Nowak U. Thermally activated reversal in magnetic nanostructures. In: Annual Reviews Of Computational PhysicsIX. World Scientific; 2001. p. 105–151.

[173] Rüemelin W. Numerical treatment of stochastic differential equations. SIAM Journal on Numerical Analysis. 1982;19(3):604–613.

[174] Barlow RJ. Statistics: a guide to the use of statistical methods in the physical sciences. vol. 29. John Wiley & Sons; 1989.

[175] Limpert E, Stahel WA, Abbt M. Log-normal Distributions across the Sciences: Keys and Clues: On the charms of statistics, and how mechanical models resembling gambling machines offer a link to a handy way to characterize log-normal distributions, which can provide deeper insight into variability and probability—normal or log-normal: That is the

question. AIBS Bulletin. 2001;51(5):341–352.

[176] Soto-Aquino D, Rinaldi C. Nonlinear energy dissipation of magnetic nanoparticles in oscillating magnetic fields. Journal of Magnetism and Magnetic Materials. 2015;393:46–55.

[177] Hergt R, Dutz S, Müller R, Zeisberger M. Magnetic particle hyperthermia: nanoparticle magnetism and materials development for cancer therapy. Journal of Physics: Condensed Matter. 2006;18(38):S2919.

[178] Schwertmann U, Cornell RM. Iron oxides in the laboratory. Preparation and characterization. VHC Publishers, Inc.: New York, New York, USA. Illus; 1991.

[179] Thanh NT. Magnetic nanoparticles: from fabrication to clinical application. Boca Raton: CRC press; 2012.

[180] Massart R, Cabuil V. Effect of some parameters on the formation of colloidal magnetite in alkaline-medium-yield and particle-size control. Journal de Chimie Physique et de Physico-Chimie Biologique. 1987;84(7-8):967–973.

[181] Bastús NG, Comenge J, Puntes V. Kinetically controlled seeded growth synthesis of citrate-stabilized gold nanoparticles of up to 200 nm: size focusing versus Ostwald ripening. Langmuir. 2011;27(17):11098–11105.

[182] Lu AH, Salabas E, Schüth F. Magnetische Nanopartikel: Synthese, Stabilisierung, Funktionalisierung und Anwendung. Angewandte Chemie. 2007;119(8):1242–1266.

[183] Jeong U, Teng X, Wang Y, Yang H, Xia Y. Superparamagnetic colloids: controlled synthesis and niche applications. Advanced Materials. 2007;19(1):33–60.

[184] Arami H, Khandhar A, Liggitt D, Krishnan KM. In vivo delivery, pharmacokinetics, biodistribution and toxicity of iron oxide nanoparticles. Chemical Society Reviews. 2015;44(23):8576–8607.

[185] McCormack PL. Ferumoxytol. Drugs. 2012;72(15):2013–2022.

[186] Lu M, Cohen MH, Rieves D, Pazdur R. FDA report: ferumoxytol for intravenous iron therapy in adult patients with chronic kidney disease. American journal of hematology. 2010;85(5):315–319.

[187] Rienso (ferumoxytol): summary of product characteristics. Takeda Global Research and Development Centre (Europe) Ltd. 2012;.

[188] Schiller B, Bhat P, Sharma A. Safety and effectiveness of ferumoxytol in hemodialysis patients at 3 dialysis chains in the United States over a 12-month period. Clinical therapeutics. 2014;36(1):70–83.

[189] ; 2009. Encyclopedia Britannica. Online Library. http://www.britannica.com/.

[190] Khalafalla S, Reimers G. Preparation of dilution-stable aqueous magnetic fluids. IEEE Transactions on Magnetics. 1980;16(2):178–183.

[191] De Cuyper M, Müller P, Lueken H, Hodenius M. Synthesis of magnetic Fe3O4 particles covered with a modifiable phospholipid coat. Journal of Physics: Condensed Matter. 2003;15(15):S1425.

[192] De Cuyper M, Soenen SJH. In: Weissig V, editor. Cationic Magnetoliposomes. vol. 605 of Methods in Molecular Biology. Human Press; 2010. p. 97–111.

[193] Massart R. Preparation of aqueous magnetic liquids in alkaline and acidic media. IEEE transactions on magnetics. 1981;17(2):1247–1248.

[194] Fortin JP, Wilhelm C, Servais J, Menager C, Bacri JC, Gazeau F. Size-sorted anionic iron oxide nanomagnets as colloidal mediators for magnetic hyperthermia. Journal of the American Chemical Society. 2007;129(9):2628–2635.

[195] Bealle G, Di Corato R, Kolosnjaj-Tabi J, Dupuis V, Clement O, Gazeau F, et al. Ultra magnetic liposomes for MR imaging, targeting, and hyperthermia. Langmuir. 2012;28(32):11834–11842.

[196] Kemp SJ, Ferguson RM, Khandhar AP, Krishnan KM. Monodisperse magnetite nanoparticles with nearly ideal saturation magnetization. RSC Advances. 2016;6(81):77452–77464.

[197] Khandhar AP, Ferguson RM, Krishnan KM. Monodispersed magnetite nanoparticles optimized for magnetic fluid hyperthermia: Implications in biological systems. Journal of applied physics. 2011;109(7):07B310.

[198] Park J, An K, Hwang Y, Park JG, Noh HJ, Kim JY, et al. Ultra-large-scale syntheses of monodisperse nanocrystals. Nature materials. 2004;3(12):891.

[199] Khandhar AP, Ferguson RM, Simon JA, Krishnan KM. Tailored magnetic nanoparticles for optimizing magnetic fluid hyperthermia. Journal of Biomedical Materials Research Part A. 2012;100(3):728–737.

[200] Klibanov AL, Maruyama K, Beckerleg AM, Torchilin VP, Huang L. Activity of amphipathic poly (ethylene glycol) 5000 to prolong the circulation time of liposomes depends on the liposome size and is unfavorable for immunoliposome binding to target. Biochimica et Biophysica Acta (BBA)-Biomembranes. 1991;1062(2):142–148.

[201] William WY, Chang E, Sayes CM, Drezek R, Colvin VL. Aqueous dispersion of monodisperse magnetic iron oxide nanocrystals through phase transfer. Nanotechnology. 2006;17(17):4483.

[202] Halliday D, Resnick R, Koch SW, Walker J. Halliday Physik. v. 1, p. 1085. John Wiley

& Sons, Limited; 2003.

[203] Department of Earth & Environmental Sciences RPI. The Electron Microprobe method. http://ees2.geo.rpi.edu/probe/Images/concepts/concept2.html; 22-APR-2018.

[204] Patterson A. The Scherrer formula for X-ray particle size determination. Physical review. 1939;56(10):978.

[205] Swanson HE, Tatge E. Standard X-ray diffraction patterns. Journal of Research of the National Bureau of Standards. 1951;46(4):318.

[206] Schulz D, McCarthy G, Grant-in Aid I. North Dakota State University. Fargo, North Dakota, USA, ICDD Grant-in-Aid. 1987;.

[207] Hufschmid R, Arami H, Ferguson RM, Gonzales M, Teeman E, Brush LN, et al. Synthesis of phase-pure and monodisperse iron oxide nanoparticles by thermal decomposition. Nanoscale. 2015;7(25):11142–11154.

[208] Howard S, Preston K. Profile fitting of powder diffraction patterns. Reviews in Mineralogy and Geochemistry. 1989;20(1):217–275.

[209] Williams DB, Carter CB. The transmission electron microscope. In: Transmission electron microscopy. Springer; 1996. p. 3–17.

[210] Mäntele W. Biophysik. Ulmer Stuttgart; 2012.

[211] Sawada H, Shimura N, Hosokawa F, Shibata N, Ikuhara Y. Resolving 45-pm-separated Si–Si atomic columns with an aberration-corrected STEM. Microscopy. 2015;64(3):213–217.

[212] Brewster R. Paint .NET-Free Software for Digital Photo Editing. Getpaintnet Ultimo acceso. 2017;15.

[213] Schneider CA, Rasband WS, Eliceiri KW. NIH Image to ImageJ: 25 years of image analysis. Nature methods. 2012;9(7):671.

[214] Teeman E. Personal Communication. University of Washington, Krishnan Labs. 2018;.

[215] O'grady K, Bradbury A. Particle size analysis in ferrofluids. Journal of Magnetism and magnetic Materials. 1983;39(1-2):91–94.

[216] Malvern Instruments Ldt. Dynamic Light Scattering: An Introduction in 30 Minutes; Technical Note MRK656-01.

[217] Pecora R. Dynamic light scattering: applications of photon correlation spectroscopy. Springer Science & Business Media; 2013.

[218] Berne B, Pecora R. Dynamic light scattering. USA, New York. 2000;.

[219] ISO-22412:2017. Particle size analysis - dynamic light scattering (DLS); 2018-09-03. Available from: https://www.iso.org/standard/65410.html.

[220] Nobbmann U. FAQ: Peak size or z-average size – which one to pick in DLS?; 2018-09-03. Available from: http://www.materials-talks.com/blog/2014/07/10/faq-peak-size-or-z-average-size-which-one-to-pick-in-dls/.

[221] Khandhar AP. Biomedical imaging and therapy with physically and physiologically tailored magnetic nanoparticles. PhD thesis, University of Washington. 2013;.

[222] De Cuyper M, Hodenius M, Ivanova G, Baumann M, Paciok E, Eckert T, et al. Specific heating power of fatty acid and phospholipid stabilized magnetic fluids in an alternating magnetic field. Journal of Physics: Condensed Matter. 2008;20(20):204131.

[223] Lak A, Niculaes D, Anyfantis GC, Bertoni G, Barthel MJ, Marras S, et al. Facile transformation of FeO/Fe 3 O 4 core-shell nanocubes to Fe 3 O 4 via magnetic stimulation. Scientific reports. 2016;6:33295.

[224] Hollemann A, Wiberg E, Wiberg N. Lehrbuch der Anorganischen Chemie, 91.-100. Auflage. Walter de Gruyter, Berlin. 1985;999:1012–1021.

[225] Olesik JW. Elemental analysis using ICP-OES and ICP/MS. Analytical Chemistry. 1991;63(1):12A–21A.

[226] Bhadani S, Tiwari M, Agrawal A, Kavipurapu CS. Spectrophotometric determination of Fe (III) with tiron in the presence of cationic surfactant and its application for the determination of iron in Al-alloys and Cu-based alloys. Microchimica Acta. 1994;117(1-2):15–22.

[227] Clarke J. SQUIDS. Scientific American. 1994;271(2):46–53.

[228] Script: Superconductivity and SQUID magnetometer. RWTH Aachen University; 2011.

[229] Ashcroft NW, Mermin ND. Solid state physics. Science: Physics. Saunders College; 1976.

[230] Chantrell R, Popplewell J, Charles S. Measurements of particle size distribution parameters in ferrofluids. IEEE Transactions on Magnetics. 1978;14(5):975–977.

[231] Bradbury A, Menear K, O'Grady K, Chantrell R. Magnetic size determination for interacting fine particle systems. IEEE Transactions on Magnetics. 1984;20(5):1846–1848.

[232] Winkler K, Murphy W. Rock physics and phase relations: a handbook of physical constants. American Geophysical Union; 1995.

[233] Hu P, Kang L, Chang T, Yang F, Wang H, Zhang Y, et al. High saturation magnetization Fe3O4 nanoparticles prepared by one-step reduction method in autoclave. Journal of Alloys and Compounds. 2017;728:88–92.

[234] Shete P, Patil R, Tiwale B, Pawar S. Water dispersible oleic acid-coated Fe3O4 nanoparticles for biomedical applications. Journal of Magnetism and Magnetic Materials. 2015;377:406–410.

[235] Pal S, Dutta P, Shah N, Huffman G, Seehra M. Surface Spin Disorder in Fe $_{3}$ O $_{4}$ Nanoparticles Probed by Electron Magnetic Resonance Spectroscopy and Magnetometry. IEEE transactions on magnetics. 2007;43(6):3091–3093.

[236] Schmitz-Antoniak C, Schmitz D, Warland A, Darbandi M, Haldar S, Bhandary S, et al. Suppression of the Verwey Transition by Charge Trapping. Annalen der Physik. 2018;530(3):1700363.

[237] Nedelkoski Z, Kepaptsoglou D, Lari L, Wen T, Booth RA, Oberdick SD, et al. Origin of reduced magnetization and domain formation in small magnetite nanoparticles. Scientific reports. 2017;7:45997.

[238] Hai HT, Yang HT, Kura H, Hasegawa D, Ogata Y, Takahashi M, et al. Size control and characterization of wustite (core)/spinel (shell) nanocubes obtained by decomposition of iron oleate complex. Journal of colloid and interface science. 2010;346(1):37–42.

[239] Pichon BP, Gerber O, Lefevre C, Florea I, Fleutot S, Baaziz W, et al. Microstructural and magnetic investigations of wustite-spinel core-shell cubic-shaped nanoparticles. Chemistry of Materials. 2011;23(11):2886–2900.

[240] Unni M, Uhl AM, Savliwala S, Savitzky BH, Dhavalikar R, Garraud N, et al. Thermal decomposition synthesis of iron oxide nanoparticles with diminished magnetic dead layer by controlled addition of oxygen. ACS nano. 2017;11(2):2284–2303.

[241] Tamion A, Hillenkamp M, Tournus F, Bonet E, Dupuis V. Accurate determination of the magnetic anisotropy in cluster-assembled nanostructures. Applied Physics Letters. 2009;95(6):062503.

[242] Tournus F, Bonet E. Magnetic susceptibility curves of a nanoparticle assembly, I: Theoretical model and analytical expressions for a single magnetic anisotropy energy. Journal of Magnetism and Magnetic Materials. 2011;323(9):1109–1117.

[243] Tournus F, Tamion A. Magnetic susceptibility curves of a nanoparticle assembly II. Simulation and analysis of ZFC/FC curves in the case of a magnetic anisotropy energy distribution. Journal of Magnetism and Magnetic Materials. 2011;323(9):1118–1127.

[244] Tournus F, Blanc N, Tamion A, Hillenkamp M, Dupuis V. Dispersion of magnetic anisotropy in size-selected CoPt clusters. Physical Review B. 2010;81(22):220405.

[245] Di Corato R, Espinosa A, Lartigue L, Tharaud M, Chat S, Pellegrino T, et al. Magnetic hyperthermia efficiency in the cellular environment for different nanoparticle designs. Biomaterials. 2014;35(24):6400–6411.

[246] Branquinho LC, Carrião MS, Costa AS, Zufelato N, Sousa MH, Miotto R, et al. Effect of magnetic dipolar interactions on nanoparticle heating efficiency: Implications for cancer hyperthermia. Scientific reports. 2013;3:2887.

[247] Levy M, Wilhelm C, Luciani N, Deveaux V, Gendron F, Luciani A, et al. Nanomagnetism reveals the intracellular clustering of iron oxide nanoparticles in the organism. Nanoscale. 2011;3(10):4402–4410.

[248] Lévy M, Gazeau F, Bacri JC, Wilhelm C, Devaud M. Modeling magnetic nanoparticle dipole-dipole interactions inside living cells. Physical Review B. 2011;84(7):075480.

[249] Quantum Design Inc . VSM Option User's Manual, 1096-100, Rev. B0; February 2011.

[250] Foner S. Vibrating Sample Magnetometer. Review of Scientific Instruments. 1956;27(7):548–548.

[251] Engelmann UM, Shasha C, Teeman E, Slabu I, Krishnan KM. Predicting size-dependent heating efficiency of magnetic nanoparticles from experiment and stochastic Néel-Brown Langevin simulation. Journal of Magnetism and Magnetic Materials. 2019;471:450–456.

[252] Roca A, Morales M, O'Grady K, Serna C. Structural and magnetic properties of uniform magnetite nanoparticles prepared by high temperature decomposition of organic precursors. Nanotechnology. 2006;17(11):2783.

[253] Chen DX, Sanchez A, Taboada E, Roig A, Sun N, Gu HC. Size determination of superparamagnetic nanoparticles from magnetization curve. Journal of Applied Physics. 2009;105(8):083924.

[254] Löwa N, Radon P, Kosch O, Wiekhorst F. Concentration dependent MPI tracer performance. International Journal on Magnetic Particle Imaging. 2016;2(1).

[255] Friedrich RP, Janko C, Poettler M, Tripal P, Zaloga J, Cicha I, et al. Flow cytometry for intracellular SPION quantification: specificity and sensitivity in comparison with spectroscopic methods. International journal of nanomedicine. 2015;10:4185.

[256] Gräfe C, Slabu I, Wiekhorst F, Bergemann C, von Eggeling F, Hochhaus A, et al. Magnetic particle spectroscopy allows precise quantification of nanoparticles after passage through human brain microvascular endothelial cells. Physics in Medicine & Biology. 2016;61(11):3986.

[257] Ficko BW, NDong C, Giacometti P, Griswold KE, Diamond SG. A feasibility study of nonlinear spectroscopic measurement of magnetic nanoparticles targeted to cancer cells. IEEE Transactions on Biomedical Engineering. 2017;64(5):972–979.

[258] Schilling M, Ludwig F, Kuhlmann C, Wawrzik T. Magnetic particle imaging scanner with 10-kHz drive-field frequency. Biomedizinische Technik/Biomedical Engineering.

2013;58(6):557–563.

[259] Draack S, Viereck T, Kuhlmann C, Schilling M, Ludwig F. Temperature-dependent MPS measurements. International Journal on Magnetic Particle Imaging. 2017;3(1).

[260] Arami H, Ferguson R, Khandhar AP, Krishnan KM. Size-dependent ferrohydrodynamic relaxometry of magnetic particle imaging tracers in different environments. Medical physics. 2013;40(7).

[261] Khandhar AP, Ferguson RM, Arami H, Krishnan KM. Monodisperse magnetite nanoparticle tracers for in vivo magnetic particle imaging. Biomaterials. 2013;34(15):3837–3845.

[262] Ferguson RM, Khandhar AP, Kemp SJ, Arami H, Saritas EU, Croft LR, et al. Magnetic particle imaging with tailored iron oxide nanoparticle tracers. IEEE transactions on medical imaging. 2015;34(5):1077–1084.

[263] Yu EY, Bishop M, Zheng B, Ferguson RM, Khandhar AP, Kemp SJ, et al. Magnetic particle imaging: a novel in vivo imaging platform for cancer detection. Nano letters. 2017;17(3):1648–1654.

[264] Engelmann U, Seifert J, Mues B, Roitsch S, Menager C, Schmidt A, et al. Heating efficiency of magnetic nanoparticles decreases with gradual immobilization in hydrogels. Journal of Magnetism and Magnetic Materials. 2019;471:486–494.

[265] Jones C; 2017. NanoTherics, Ltd., Keele, Staffordshire, UK. Personal communication.

[266] Huang S, Wang S, Gupta A, Borca-Tasciuc D, Salon S. On the measurement technique for specific absorption rate of nanoparticles in an alternating electromagnetic field. Measurement Science and Technology. 2012;23(3):035701.

[267] Gonzales-Weimuller M, Zeisberger M, Krishnan KM. Size-dependant heating rates of iron oxide nanoparticles for magnetic fluid hyperthermia. Journal of magnetism and magnetic materials. 2009;321(13):1947–1950.

[268] Bordelon DE, Cornejo C, Grüttner C, Westphal F, DeWeese TL, Ivkov R. Magnetic nanoparticle heating efficiency reveals magneto-structural differences when characterized with wide ranging and high amplitude alternating magnetic fields. Journal of Applied Physics. 2011;109(12):124904.

[269] Wildeboer R, Southern P, Pankhurst Q. On the reliable measurement of specific absorption rates and intrinsic loss parameters in magnetic hyperthermia materials. Journal of Physics D: Applied Physics. 2014;47(49):495003.

[270] Ng EYK, Kumar SD, et al. Physical mechanism and modeling of heat generation and transfer in magnetic fluid hyperthermia through Néelian and Brownian relaxation: a review. Biomedical engineering online. 2017;16(1):36.

[271] Hiergeist R, Andrä W, Buske N, Hergt R, Hilger I, Richter U, et al. Application of magnetite ferrofluids for hyperthermia. Journal of Magnetism and Magnetic Materials. 1999;201(1-3):420–422.

[272] Wang X, Gu H, Yang Z. The heating effect of magnetic fluids in an alternating magnetic field. Journal of Magnetism and Magnetic Materials. 2005;293(1):334–340.

[273] Li CH, Hodgins P, Peterson G. Experimental study of fundamental mechanisms in inductive heating of ferromagnetic nanoparticles suspension (Fe3O4 Iron Oxide Ferrofluid). Journal of Applied Physics. 2011;110(5):054303.

[274] Kashevsky BE, Kashevsky SB, Prokhorov IV. Dynamic magnetic hysteresis in a liquid suspension of acicular maghemite particles. Particuology. 2009;7(6):451–458.

[275] Lacroix LM, Malaki RB, Carrey J, Lachaize S, Respaud M, Goya G, et al. Magnetic hyperthermia in single-domain monodisperse FeCo nanoparticles: evidences for Stoner–Wohlfarth behavior and large losses. Journal of Applied Physics. 2009;105(2):023911.

[276] Dennis CL, Krycka KL, Borchers JA, Desautels RD, Van Lierop J, Huls NF, et al. Internal magnetic structure of nanoparticles dominates time-dependent relaxation processes in a magnetic field. Advanced Functional Materials. 2015;25(27):4300–4311.

[277] Conde-Leboran I, Baldomir D, Martinez-Boubeta C, Chubykalo-Fesenko O, del Puerto Morales M, Salas G, et al. A single picture explains diversity of hyperthermia response of magnetic nanoparticles. The Journal of Physical Chemistry C. 2015;119(27):15698–15706.

[278] Bae S, Lee SW, Takemura Y, Yamashita E, Kunisaki J, Zurn S, et al. Dependence of frequency and magnetic field on self-heating characteristics of NiFe $_2$ O $_4$ nanoparticles for hyperthermia. IEEE transactions on magnetics. 2006;42(10):3566–3568.

[279] Kallumadil M, Tada M, Nakagawa T, Abe M, Southern P, Pankhurst QA. Suitability of commercial colloids for magnetic hyperthermia. Journal of Magnetism and Magnetic Materials. 2009;321(10):1509–1513.

[280] Blanco-Andujar C, Ortega D, Southern P, Pankhurst Q, Thanh N. High performance multi-core iron oxide nanoparticles for magnetic hyperthermia: microwave synthesis, and the role of core-to-core interactions. Nanoscale. 2015;7(5):1768–1775.

[281] Lima Jr E, De Biasi E, Mansilla MV, Saleta ME, Granada M, Troiani HE, et al. Heat generation in agglomerated ferrite nanoparticles in an alternating magnetic field. Journal of Physics D: Applied Physics. 2012;46(4):045002.

[282] Verde E, Landi GT, Carrião M, Drummond AL, Gomes J, Vieira E, et al. Field dependent transition to the non-linear regime in magnetic hyperthermia experiments: Comparison between maghemite, copper, zinc, nickel and cobalt ferrite nanoparticles of similar sizes.

Aip Advances. 2012;2(3):032120.

[283] Verde EL, Landi GT, Gomes JdA, Sousa MH, Bakuzis AF. Magnetic hyperthermia investigation of cobalt ferrite nanoparticles: Comparison between experiment, linear response theory, and dynamic hysteresis simulations. Journal of Applied Physics. 2012;111(12):123902.

[284] Ludwig F, Remmer H, Kuhlmann C, Wawrzik T, Arami H, Ferguson RM, et al. Self-consistent magnetic properties of magnetite tracers optimized for magnetic particle imaging measured by ac susceptometry, magnetorelaxometry and magnetic particle spectroscopy. Journal of magnetism and magnetic materials. 2014;360:169–173.

[285] Niculaes D, Lak A, Anyfantis GC, Marras S, Laslett O, Avugadda SK, et al. Asymmetric Assembling of Iron Oxide Nanocubes for Improving Magnetic Hyperthermia Performance. ACS nano. 2017;11(12):12121–12133.

[286] Cabrera D, Coene A, Leliaert J, Artés-Ibáñez EJ, Dupré L, Telling ND, et al. Dynamical magnetic response of iron oxide nanoparticles inside live cells. ACS nano. 2018;.

[287] Dennis C, Jackson A, Borchers J, Ivkov R, Foreman A, Lau J, et al. The influence of collective behavior on the magnetic and heating properties of iron oxide nanoparticles. Journal of Applied Physics. 2008;103(7):07A319.

[288] Deleu M, Crowet JM, Nasir MN, Lins L. Complementary biophysical tools to investigate lipid specificity in the interaction between bioactive molecules and the plasma membrane: a review. Biochimica et Biophysica Acta (BBA)-Biomembranes. 2014;1838(12):3171–3190.

[289] Ma DD, Wei AQ. Enhanced delivery of synthetic oligonucleotides to human leukaemic cells by liposomes and immunoliposomes. Leukemia research. 1996;20(11-12):925–930.

[290] Wang Y, Miao L, Satterlee A, Huang L. Delivery of oligonucleotides with lipid nanoparticles. Advanced drug delivery reviews. 2015;87:68–80.

[291] Slabu I, Roeth A, Engelmann U, Wiekhorst F, Buhl E, Neumann U, et al. Modelling of magnetoliposome uptake in human pancreatic tumor cells in vitro. Nanotechnology: Special issue - focus on personalized medicine and theranostics. 2019;.

[292] Yunis AA, Arimura GK, Russin DJ. Human pancreatic carcinoma (MIA PaCa-2) in continuous culture: sensitivity to asparaginase. International journal of cancer. 1977;19(1):128–135.

[293] Edge SB, Compton CC. The American Joint Committee on Cancer: the 7th edition of the AJCC cancer staging manual and the future of TNM. Annals of surgical oncology. 2010;17(6):1471–1474.

[294] Oberlin L. Behandlung von Pankreaskarzinomzelllinien in vitro und in vivo mit einem monoklonalen Antikoerper gegen den Transferrinrezeptor. Universitaetsbibliothek Giessen; Doktorarbeit; 2009.

[295] Tan MH, Nowak NJ, Loor R, Ochi H, Sandberg AA, Lopez C, et al. Characterization of a new primary human pancreatic tumor line. Cancer investigation. 1986;4(1):15–23.

[296] Earle WR, Voegtlin C. A further study of the mode of action of methylcholanthrene on normal tissue cultures. Public Health Reports (1896-1970). 1940;p. 303–322.

[297] Sanford KK, Earle WR, Likely GD. The growth in vitro of single isolated tissue cells. Journal of the National Cancer Institute. 1948;9(3):229–246.

[298] Theerakittayakorn K, Bunprasert T. Differentiation capacity of mouse L929 fibroblastic cell line compare with human dermal fibroblast. World Acad Sci Eng Technol. 2011;50:373–376.

[299] Baca OG, Scott T, Akporiaye E, DeBlassie R, Crissman H. Cell cycle distribution patterns and generation times of L929 fibroblast cells persistently infected with Coxiella burnetii. Infection and immunity. 1985;47(2):366–369.

[300] Wilhelm C, Gazeau F, Roger J, Pons J, Bacri JC. Interaction of anionic superparamagnetic nanoparticles with cells: kinetic analyses of membrane adsorption and subsequent internalization. Langmuir. 2002;18(21):8148–8155.

[301] Chithrani BD, Chan WC. Elucidating the mechanism of cellular uptake and removal of protein-coated gold nanoparticles of different sizes and shapes. Nano letters. 2007;7(6):1542–1550.

[302] Dos Santos T, Varela J, Lynch I, Salvati A, Dawson KA. Quantitative assessment of the comparative nanoparticle-uptake efficiency of a range of cell lines. Small. 2011;7(23):3341–3349.

[303] Limbach LK, Li Y, Grass RN, Brunner TJ, Hintermann MA, Muller M, et al. Oxide nanoparticle uptake in human lung fibroblasts: effects of particle size, agglomeration, and diffusion at low concentrations. Environmental science & technology. 2005;39(23):9370–9376.

[304] Chaudhuri A, Battaglia G, Golestanian R. The effect of interactions on the cellular uptake of nanoparticles. Physical biology. 2011;8(4):046002.

[305] Soukup D, Moise S, Céspedes E, Dobson J, Telling ND. In situ measurement of magnetization relaxation of internalized nanoparticles in live cells. Acs Nano. 2015;9(1):231–240.

[306] Sanz B, Calatayud MP, De Biasi E, Lima Jr E, Mansilla MV, Zysler RD, et al. In silico before in vivo: how to predict the heating efficiency of magnetic nanoparticles within the

intracellular space. Scientific reports. 2016;6:38733.

[307] De Duve C. The lysosome concept. In: Ciba Foundation Symposium-Anterior Pituitary Secretion (Book I of Colloquia on Endocrinology). Wiley Online Library; 1963. p. 1–35.

[308] De Duve C, Wattiaux R. Functions of lysosomes. Annual review of physiology. 1966;28(1):435–492.

[309] McNaught AD, McNaught AD. Compendium of chemical terminology. vol. 1669. Blackwell Science Oxford; 1997.

[310] Chang JS, Chang KLB, Hwang DF, Kong ZL. In vitro cytotoxicitiy of silica nanoparticles at high concentrations strongly depends on the metabolic activity type of the cell line. Environmental science & technology. 2007;41(6):2064–2068.

[311] Kim JA, Åberg C, Salvati A, Dawson KA. Role of cell cycle on the cellular uptake and dilution of nanoparticles in a cell population. Nature nanotechnology. 2012;7(1):62.

[312] Martina MS, Nicolas V, Wilhelm C, Ménager C, Barratt G, Lesieur S. The in vitro kinetics of the interactions between PEG-ylated magnetic-fluid-loaded liposomes and macrophages. Biomaterials. 2007;28(28):4143–4153.

[313] Martina MS, Wilhelm C, Lesieur S. The effect of magnetic targeting on the uptake of magnetic-fluid-loaded liposomes by human prostatic adenocarcinoma cells. Biomaterials. 2008;29(30):4137–4145.

[314] Rappoport J, Preece J, Chipman K, Argatov I, Davies A, Dyson L, et al. „How do Manufactured Nanoparticles Enter Cells. Microporous and Mesoporous Materials. 2011;116:123–130.

[315] Serda RE, Mack A, Van De Ven AL, Ferrati S, Dunner Jr K, Godin B, et al. Logic-Embedded Vectors for Intracellular Partitioning, Endosomal Escape, and Exocytosis of Nanoparticles. Small. 2010;6(23):2691–2700.

[316] Jiang X, Roecker C, Hafner M, Brandholt S, Doerlich RM, Nienhaus GU. Endo-and exocytosis of zwitterionic quantum dot nanoparticles by live HeLa cells. ACS nano. 2010;4(11):6787–6797.

[317] Rascol E, Devoisselle JM, Chopineau J. The relevance of membrane models to understand nanoparticles–cell membrane interactions. Nanoscale. 2016;8(9):4780–4798.

[318] Ding Hm, Ma Yq. Theoretical and computational investigations of nanoparticle–biomembrane interactions in cellular delivery. Small. 2015;11(9-10):1055–1071.

[319] Bahrami AH, Raatz M, Agudo-Canalejo J, Michel R, Curtis EM, Hall CK, et al. Wrapping of nanoparticles by membranes. Advances in colloid and interface science. 2014;208:214–224.

[320] Fenzl C, Genslein C, Domonkos C, Edwards K, Hirsch T, Baeumner A. Investigating non-specific binding to chemically engineered sensor surfaces using liposomes as models. Analyst. 2016;141(18):5265–5273.

[321] Lee RJ, Low PS. Delivery of liposomes into cultured KB cells via folate receptor-mediated endocytosis. Journal of Biological Chemistry. 1994;269(5):3198–3204.

[322] Gao H, Shi W, Freund LB. Mechanics of receptor-mediated endocytosis. Proceedings of the National Academy of Sciences. 2005;102(27):9469–9474.

[323] Osaki F, Kanamori T, Sando S, Sera T, Aoyama Y. A quantum dot conjugated sugar ball and its cellular uptake. On the size effects of endocytosis in the subviral region. Journal of the American Chemical Society. 2004;126(21):6520–6521.

[324] Bartczak D, Nitti S, Millar TM, Kanaras AG. Exocytosis of peptide functionalized gold nanoparticles in endothelial cells. Nanoscale. 2012;4(15):4470–4472.

[325] Bartczak D, Nitti S, Millar TM, Kanaras AG. Exocytosis of peptide functionalized gold nanoparticles in endothelial cells. Nanoscale. 2012;4(15):4470–4472.

[326] Poller WC, Löwa N, Wiekhorst F, Taupitz M, Wagner S, Möller K, et al. Magnetic particle spectroscopy reveals dynamic changes in the magnetic behavior of very small superparamagnetic iron oxide nanoparticles during cellular uptake and enables determination of cell-labeling efficacy. Journal of biomedical nanotechnology. 2016;12(2):337–346.

[327] Dutz S, Hergt R. The role of interactions in systems of single domain ferrimagnetic iron oxide nanoparticles. Journal of Nano- and Electronic Physics. 2012;4(2).

[328] Engelmann U, Buhl EM, Baumann M, Schmitz-Rode T, Slabu I. Agglomeration of magnetic nanoparticles and its effects on magnetic hyperthermia. Current Directions in Biomedical Engineering. 2017;3(2):457–460.

[329] Engelmann UM, Buhl EM, Draack S, Viereck T, Ludwig F, Schmitz-Rode T, et al. Magnetic relaxation of agglomerated and immobilized iron oxide nanoparticles for hyperthermia and imaging applications. IEEE Magnetics Letters. 2018;9:1–5.

[330] Calvet D, Wong JY, Giasson S. Rheological monitoring of polyacrylamide gelation: Importance of cross-link density and temperature. Macromolecules. 2004;37(20):7762–7771.

[331] Engler AJ, Sen S, Sweeney HL, Discher DE. Matrix elasticity directs stem cell lineage specification. Cell. 2006;126(4):677–689.

[332] Pernodet N, Maaloum M, Tinland B. Pore size of agarose gels by atomic force microscopy. Electrophoresis. 1997;18(1):55–58.

[333] Narayanan J, Xiong JY, Liu XY. Determination of agarose gel pore size: Absorbance measurements vis a vis other techniques. In: Journal of Physics: Conference Series.

vol. 28. IOP Publishing; 2006. p. 83.

[334] Roeder L, Reckenthaeler M, Belkoura L, Roitsch S, Strey R, Schmidt A. Covalent ferrohy-drogels based on elongated particulate cross-linkers. Macromolecules. 2014;47(20):7200–7207.

[335] Wang J, Ugaz VM. Using in situ rheology to characterize the microstructure in photopoly-merized polyacrylamide gels for DNA electrophoresis. Electrophoresis. 2006;27(17):3349–3358.

[336] Khlebtsov B, Khlebtsov N. On the measurement of gold nanoparticle sizes by the dynamic light scattering method. Colloid Journal. 2011;73(1):118–127.

[337] Fissan H, Ristig S, Kaminski H, Asbach C, Epple M. Comparison of different character-ization methods for nanoparticle dispersions before and after aerosolization. Analytical Methods. 2014;6(18):7324–7334.

[338] Martens MA, Deissler RJ, Wu Y, Bauer L, Yao Z, Brown R, et al. Modeling the Brown-ian relaxation of nanoparticle ferrofluids: comparison with experiment. Medical physics. 2013;40(2).

[339] Hrozek J, Nespor D, Bartusek K. Thermal Conductivity and Heat Capacity Measurement of Biological Tissues. In: PIERS Proceedings; 2013. .

[340] Bergman TL, Incropera FP, DeWitt DP, Lavine AS. Fundamentals of heat and mass transfer. John Wiley & Sons; 2011.

[341] Bu-Lin Z, Bing H, Sheng-Li K, Huang Y, Rong W, Jia L. A polyacrylamide gel phantom for radiofrequency ablation. International Journal of Hyperthermia. 2008;24(7):568–576.

[342] Rojas JM, Gavilán H, del Dedo V, Lorente-Sorolla E, Sanz-Ortega L, da Silva GB, et al. Time-course assessment of the aggregation and metabolization of magnetic nanoparticles. Acta biomaterialia. 2017;58:181–195.

[343] Ludwig R, Stapf M, Dutz S, Müller R, Teichgräber U, Hilger I. Structural properties of magnetic nanoparticles determine their heating behavior-an estimation of the in vivo heating potential. Nanoscale research letters. 2014;9(1):602.

[344] Dieckhoff J, Eberbeck D, Schilling M, Ludwig F. Magnetic-field dependence of Brownian and Néel relaxation times. Journal of Applied Physics. 2016;119(4):043903.

[345] Yoshida T, Enpuku K. Simulation and quantitative clarification of AC susceptibility of magnetic fluid in nonlinear Brownian relaxation region. Japanese Journal of Applied Physics. 2009;48(12R):127002.

[346] Fannin P, Charles S. On the calculation of the Neel relaxation time in uniaxial single-domain ferromagnetic particles. Journal of Physics D: Applied Physics. 1994;27(2):185.

[347] Dennis C, Jackson A, Borchers J, Hoopes P, Strawbridge R, Foreman A, et al. Nearly complete regression of tumors via collective behavior of magnetic nanoparticles in hyperthermia. Nanotechnology. 2009;20(39):395103.

[348] Jiang J, Oberdörster G, Biswas P. Characterization of size, surface charge, and agglomeration state of nanoparticle dispersions for toxicological studies. Journal of Nanoparticle Research. 2009;11(1):77–89.

[349] Genck W. Make the most of antisolvent crystallization. Chemical Processing. 2010;.

[350] Tan CY, Huang YX. Dependence of refractive index on concentration and temperature in electrolyte solution, polar solution, nonpolar solution, and protein solution. Journal of Chemical & Engineering Data. 2015;60(10):2827–2833.

[351] Balgavỳ P, Dubničková M, Kučerka N, Kiselev MA, Yaradaikin SP, Uhriková D. Bilayer thickness and lipid interface area in unilamellar extruded 1, 2-diacylphosphatidylcholine liposomes: a small-angle neutron scattering study. Biochimica et Biophysica Acta (BBA)-Biomembranes. 2001;1512(1):40–52.

[352] Lak A, Kraken M, Ludwig F, Kornowski A, Eberbeck D, Sievers S, et al. Size dependent structural and magnetic properties of FeO–Fe 3 O 4 nanoparticles. Nanoscale. 2013;5(24):12286–12295.

[353] Stakhanova M, Karapet'yants MK, Vasil'ev V, Epikhin YA. A comparative study of the specific heats and densities of aqueous electrolyte solutions. Russ J Phys Chem. 1964;38:1306.

[354] Piñeiro-Redondo Y, Bañobre-López M, Pardiñas-Blanco I, Goya G, López-Quintela MA, Rivas J. The influence of colloidal parameters on the specific power absorption of PAA-coated magnetite nanoparticles. Nanoscale research letters. 2011;6(1):383.

[355] Spizzo F, Sgarbossa P, Sieni E, Semenzato A, Dughiero F, Forzan M, et al. Synthesis of ferrofluids made of iron oxide nanoflowers: Interplay between carrier fluid and magnetic properties. Nanomaterials. 2017;7(11):373.

[356] Saville SL, Qi B, Baker J, Stone R, Camley RE, Livesey KL, et al. The formation of linear aggregates in magnetic hyperthermia: Implications on specific absorption rate and magnetic anisotropy. Journal of colloid and interface science. 2014;424:141–151.

[357] Dennis CL, Ivkov R. Physics of heat generation using magnetic nanoparticles for hyperthermia. International Journal of Hyperthermia. 2013;29(8):715–729.

[358] Suto M, Hirota Y, Mamiya H, Fujita A, Kasuya R, Tohji K, et al. Heat dissipation mechanism of magnetite nanoparticles in magnetic fluid hyperthermia. Journal of Magnetism and Magnetic Materials. 2009;321(10):1493–1496.

[359] Franken NA, Rodermond HM, Stap J, Haveman J, Van Bree C. Clonogenic assay of cells in vitro. Nature protocols. 2006;1(5):2315.

[360] Bähring F, Schlenk F, Wotschadlo J, Buske N, Liebert T, Bergemann C, et al. Suitability of viability assays for testing biological effects of coated superparamagnetic nanoparticles. Ieee Transactions on Magnetics. 2013;49(1):383–388.

[361] Wilhelm C, Billotey C, Roger J, Pons J, Bacri JC, Gazeau F. Intracellular uptake of anionic superparamagnetic nanoparticles as a function of their surface coating. Biomaterials. 2003;24(6):1001–1011.

[362] Dickson J, Calderwood S. Temperature range and selective sensitivity of tumors to hyperthermia: a critical review. Annals of the New York Academy of Sciences. 1980;335(1):180–205.

[363] Hensley D, Tay ZW, Dhavalikar R, Zheng B, Goodwill P, Rinaldi C, et al. Combining magnetic particle imaging and magnetic fluid hyperthermia in a theranostic platform. Physics in Medicine & Biology. 2017;62(9):3483.

[364] Tay ZW, Chandrasekharan P, Chiu-Lam A, Hensley DW, Dhavalikar R, Zhou XY, et al. Magnetic particle imaging-guided heating in vivo using gradient fields for arbitrary localization of magnetic hyperthermia therapy. ACS nano. 2018;12(4):3699–3713.

[365] Lim EK, Kim T, Paik S, Haam S, Huh YM, Lee K. Nanomaterials for theranostics: recent advances and future challenges. Chemical reviews. 2014;115(1):327–394.

[366] Rehman M, Asadullah Madni AI, Khan WS, Khan MI, Mahmood MA, Ashfaq M, et al. Solid and liquid lipid-based binary solid lipid nanoparticles of diacerein: in vitro evaluation of sustained release, simultaneous loading of gold nanoparticles, and potential thermoresponsive behavior. International journal of nanomedicine. 2015;10:2805.

[367] Hondow N, Brydson R, Wang P, Holton MD, Brown MR, Rees P, et al. Quantitative characterization of nanoparticle agglomeration within biological media. Journal of Nanoparticle Research. 2012;14(7):977.

[368] Cho EC, Zhang Q, Xia Y. The effect of sedimentation and diffusion on cellular uptake of gold nanoparticles. Nature nanotechnology. 2011;6(6):385.

[369] Park MV, Neigh AM, Vermeulen JP, de la Fonteyne LJ, Verharen HW, Briedé JJ, et al. The effect of particle size on the cytotoxicity, inflammation, developmental toxicity and genotoxicity of silver nanoparticles. Biomaterials. 2011;32(36):9810–9817.

[370] Ross SM. Combined DC and ELF magnetic fields can alter cell proliferation. Bioelectromagnetics: Journal of the Bioelectromagnetics Society, The Society for Physical Regulation in Biology and Medicine, The European Bioelectromagnetics Association. 1990;11(1):27–36.

[371] Fitzsimmons R, Ryaby J, Magee F, Baylink D. Combined magnetic fields increased net calcium flux in bone cells. Calcified tissue international. 1994;55(5):376–380.

[372] Kirson ED, Gurvich Z, Schneiderman R, Dekel E, Itzhaki A, Wasserman Y, et al. Disruption of cancer cell replication by alternating electric fields. Cancer research. 2004;64(9):3288–3295.

C. List of Publications

This thesis is partly based on the following original publications by the writer:

Engelmann UM, Shasha C, Teeman E, Slabu I and Krishnan KM. Predicting size-dependent heating efficiency of magnetic nanoparticles from experiment and stochastic Néel-Brown Langevin simulation. Journal of Magnetism and Magnetic Materials. 2019; 471:450-456. Published online: 2018-10-03.
[251]; used in Chapter 5, Section 5.3.

Slabu I, Roeth AA, Engelmann UM, Wiekhorst F, Buhl EM, Neumann U and Schmitz-Rode T. Modelling of magnetoliposome uptake in human pancreatic tumor cells in vitro. Nanotechnology: Special issue - focus on personalized medicine and theranostics. 2019. Published online: 2019-01-30.
[291]; used in Chapter 6, Sections 6.2 and 6.3.

Engelmann UM, Seifert J, Mues B, Roitsch S, Menager C, Schmidt A and Slabu I. Heating efficiency of magnetic nanoparticles decreases with gradual immobilization in hydrogels. Journal of Magnetism and Magnetic Materials. 2019; 471:486-494. Published online: 2018-09-29.
[264]; used in Chapter 7, Sections 7.1 and 7.2.

Engelmann UM, Buhl EM, Baumann M, Schmitz-Rode T and Slabu I. Agglomeration of magnetic nanoparticles and its effects on magnetic hyperthermia. Current Directions in Biomedical Engineering. 2017; 3(2):457–460. Published online: 2017-09-08.
[328]; used in Chapter 7, Sections 7.3 and 7.4.

Engelmann UM, Buhl EM, Draack S, Viereck T, Ludwig F, Schmitz-Rode T and Slabu I. Magnetic relaxation study of agglomerated and immobilized magnetic iron oxide nanoparticles for hyperthermic and imaging applications. IEEE Magnetics Letters. 2018; 9:1-5. Published online: 2018-11-01.
[329]; used in Chapter 7, Sections 7.3 and 7.4.

Engelmann UM, Roeth AA, Eberbeck D, Buhl EM, Neumann UP, Schmitz-Rode T and Slabu I. Combining bulk temperature and nanoheating enables advanced magnetic fluid hyperthermia efficacy on pancreatic tumor cells. Scientific Reports. 2018; 8(1):13210. Published online: 2018-09-04.
[50]; used in Chapter 2, Section 2.5 and Chapter 8.

D. Acknowledgment

"If I have seen further it is by standing on the shoulders of giants."

Sir Isaac Newton

In diesem Sinne steht diese Arbeit ganz im Zeichen hervorragender Zusammenarbeit und eines regen Austauschs mit anderen, denen ich zum Dank verpflichtet bin und ohne die diese Arbeit nicht gelungen wäre.

Mein größter Dank gilt Dr. Ioana Slabu als meiner direkte Betreuerin, Mentorin und Ideengeberin. Und daher möchte ich ihr auch als Erste danken. Als Forschungsgruppenleiterin hat sie sich unermüdlich für mein wissenschaftliches Vorankommen eingesetzt, mich an ihren Ideen teilhaben lassen und mir einen Aufenthalt als Gastwissenschaftler an der Physikalisch-Technischen Bundesanstalt in Berlin ermöglicht. Vielen Dank für das große Vertrauen und die außergewöhnliche Unterstützung, die vielen Gespräche und die tolle Atmosphäre in der Arbeitsgruppe.

Ebenso hervorragend war die Begleitung durch meine Berichter Professor Dr. Martin Baumann und Professor Dr. Jörg Fitter. Von Ihrer Seite wurde die Arbeit durch die für mich optimale Balance aus Hilfestellung in kniffligen Fragen und Freiheit im Arbeiten bestens begleitet. Danke für die angenehme Betreuung und das in mich gesteckte Vertrauen, diese Promotion trotz anfänglicher finanzieller Engpässe zu begleiten; vielen Dank ebenso für das stets offene Ohr in allen Belangen und die wissenschaftliche Betreuung meiner Studierenden. Besonders danken möchte ich Professor Dr. Jörg Fitter für seinen außergewöhnlichen Einsatz, mir sehr schnelles Feedback zu dieser Arbeit zu geben.

Mein besonderer Dank gilt dem Cusanuswerk für die finanzielle Unabhängigkeit, die diese Promotion durch ein Stipendium erst ermöglicht hat. Über die monetäre Sicherheit hinaus, habe ich besonders den Austausch mit Promovierenden anderer Wissenschaften sehr genossen und danke dem Cusanuswerk, dass insbesondere Auslandskonferenzen und mein Auslandsaufenthalt in Seattle unkompliziert und unbürokratisch unterstützt wurden. Stellvertretend möchte ich besonders Dr. Ingrid Reul für die perfekt durchorganisierten Graduiertentreffen danken und ebenso Dr. Siegfried Kleymann, der mich mehrfach zum Schreiben, Studieren und Diskutieren im Cusanushaus in Mehlem empfangen hat.

Getragen wurde ich durch die gesamte Zeit der Doktorarbeit von der außergewöhnlich guten Arbeitsatmosphäre der Biophysical & Education Engineering Gruppe des Institutes für Angewandte Medizintechnik (AME). Ich danke meinen Arbeitskollegen Dr.-Ing. Andreas Ritter, M.Sc. Benedikt Mues, M.Sc. Michael Gundlach und M.Sc. Max Lindemann für die vielen guten Stunden und erfolgreichen (nicht) Kaffeepausen. Darüber hinaus danke ich allen Studenten, die ich während meiner Zeit am Institut begleiten durfte und deren Arbeiten und Austausch diese Arbeit auf allen Ebenen bereichert haben: M.Sc. Florian Müller, M.Sc. Katharina Kol-

Infinite Science Publishing

Wissenschaft sollte allen zugänglich sein. Teilen Sie Ihr Wissen, Ihre Ideen und Ihre Leidenschaft für die Forschung. Veröffentlichen Sie Ihre Bachelor- und Masterarbeit sowie Ihre Dissertation und Habilitationsschrift bei Infinite Science.

Push your Career Publish your Thesis

www.publishing.infinite-science.de

Aktuelle Dissertationen

RWTH Aachen
Institut für Angewandte
Medizintechnik

Ulrich M. Engelmann

Assessing Magnetic
Fluid Hyperthermia

Magnetic Relaxation Simulation, Modeling of
Nanoparticle Uptake inside Pancreatic Tumor
Cells and in vitro Efficacy
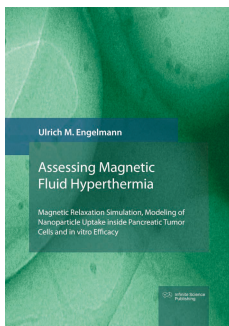
Universität Potsdam
Institut für
Chemie

David Heinke

Biokompatible superpara-
magnetische Nanopartikel

Entwicklung von Nanopartikeln für den
Einsatz als in-vivo-Diagnostikum
insbesondere im Magnetic Particle Imaging

UKSH Lübeck
Klinik für Orthopädie und
Unfallchirurgie

Annette Bretin

Elastic Properties
of the Human Femur

Local Anisotropic Material Laws
for Patient-Specific Modelling

Research Series of the Clinic for
Orthopaedics and Trauma Surgery
University of Lübeck · Volume 2
Series Editors: A.-P. Schulz and R. Wendlandt
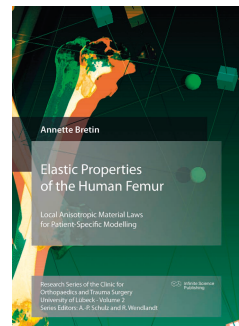
Universität zu Lübeck
Institut für
Biomedizinische Optik

Hendrik Spahr

Detektion von retinalen
Mikrobewegungen

Anwendungen der phasensensitiven
optischen Kohärenztomografie

Universität zu Lübeck
Institut für
Medizintechnik

Christoph Fabian Isernhagen

Röntgendiffraktionsbildgebung

Von der Röntgenbeugung zur
optimierten Bildrekonstruktion

Universität zu Lübeck
Institut für
Medizinische Informatik

André Mastmeyer

Personalized
Virtual Reality Simulations

Methods for Ultrasound-Guided Needle
Punctures of Breathing Virtual Patients